Doctoral Thesis

Developing Versatile Delivery Nanoplatforms Using Protein Nanoparticles

Hansol Kim

Department of Biological Sciences

Graduate School of UNIST

2020

Developing Versatile Delivery Nanoplatforms Using Protein Nanoparticles

Hansol Kim

Department of Biological Sciences

Graduate School of UNIST

Developing Versatile Delivery Nanoplatforms Using Protein Nanoparticles

A thesis/dissertation
submitted to the Graduate School of UNIST
in partial fulfillment of the
requirements for the degree of
Doctor of Philosophy

Hansol Kim

12. 03. 2019

Approved by

Advisor
Sebyung Kang

Developing Versatile Delivery Nanoplatforms Using Protein Nanoparticles

Hansol Kim

This certifies that the thesis/dissertation of Hansol Kim is approved.

12/03/2019 of submission

Advisor: Sebyung Kang

Changwook Lee

HyungJoon Cho

Ja-Hyoung Ryu

Young Chan Chae

Abstract

Targeted delivery is an important area of biomedical research, which can reduce side effects in clinical field. Various carriers, such as organic, inorganic particles, liposome, polymer, etc., have been utilized in targeted delivery. However, these vehicles have several difficulties such as the complexity of synthesis, heterogeneous size and shape and lower biocompatibility. Protein nanoparticles could be an attractive candidate as delivery vehicles. Protein nanoparticles have well-defined structure with high symmetry, uniform size and shape. These particles have also biodegradability, greater stability during *in vivo* circulation and being easy to prepare the particles. And protein nanoparticles can attach drugs, fluorescent dye, enzymes, radioactive isotopes, antigens, or antibodies at desired site depending on their purpose.

In this study, we used *Aquifex aeolicus* Lumazine synthase (AaLS) as a targeted delivery vehicle. Antibody binding domain (ABD), which was known to selectively bind to Fc part of the antibody, was genetically encoded to AaLS (ABD-AaLS). We have designed a modular delivery platform that can deliver drugs to a variety of cancer cells by binding various antibodies to ABD. This platform can deliver drug to variety of target cancer cells in *in vitro*.

Recently we have developed a targeted delivery platform using P22 virus-like particle (P22 VLP) that is relatively large-sized protein cage nanoparticles. We covalently attached affibody to exterior surface of P22 VLP using bacterial superglue system. These platforms successfully delivered anticancer drug, doxorubicin, to tumor site and showed tumor specific killing effect.

In addition, we developed the cloaking drug delivery system using mesoporous silica nanoparticles (MSNs). We constructed GST fused affibody molecules and bound these fusion proteins on MSNs as capping materials. This pre-coated nanoparticles blocked nonspecific binding of serum proteins, avoiding immune response, while maintaining targeting ability in vivo.

Our studies demonstrated that protein nanoparticles are promising platforms for diagnostic and/or therapeutic agent delivery in biomedical field.

Contents

List of figures

Chapter 4. Cloaking nanoparticles with protein corona shield for targeted drug delivery

Abbreviations

AaLS : Aquifex aeolicus lumazine synthase

ABD : Antibody binding domain

Afb : Affibody

AlDox : Aldoxorubicin

BSA : Bovine serum albumin

CD : Cluster of differentiation

CPT : Camptothecin

DLS : Dynamic light scattering

DOTA : Dodecane tetraacetic acid

EGFR : Epidermal growth factor receptor

EPR : Enhanced permeability and retention

F5M : Fluorescein-5-maleimide

FBS : Fetal bovine serum

GFP : Green fluorescent protein

GSH : Glutathione

GST : Glutathione-S-transferase

H&E : Hematoxylin and eosin

HER2 : Human epidermal growth factor receptor 2

IgG : Immunoglobulin G

IV : Intravenous

LbL : Layer by layer

LC-MS/MS : Luquid chromatography-mass spectrometry

MPS : Mononuclear phagocyte system

MSN : Mesoporous silica nanoparticle

PAGE : Polyacrylamide gel electrophoresis

PBS : Phosphate-Buffered Saline

PCS : Protein corona shield

PCSN : Protein corona shield nanoparticle

PEG : Polyethylene glycol

QCM : Quartz crystal microbalance

SC : SpyCatcher

SPR : Surface plasmon resonance

ST : SpyTag

TEM : Transmission electron microscopy

VLP : Virus like particle

WB : Wiffle ball

Chapter 1. Introduction

1.1 Nanoparticle-based cargo delivery

Nanomedicine is the biomedical application using nanotechnology. Nanomedicine is a large category including application of nanomaterials and nanodevice for drug delivery, diagnosis, biosensing, and tissue engineering. The nanomedicine has similar size and structure to biological molecules, therefore the nanomaterials are promising platform. Among the various nanomedicine area, nano based drug delivery system is the most actively studied field (Figure 1.1)[1]. Encapsulating therapeutic drugs in nanomaterials and delivering these carriers to target tissues still remain major task of therapeutics. To develop ideal nanomedicine avoiding side effect, we have to understand in detail the types and properties of nanoparticles.

1.1.1 Characteristics of nanoparticles as delivery carrier

Conventional drugs and diagnostic probes have a few limitations for biomedical application. Drugs and diagnostic probes rapidly diffuse and spread throughout the body, which cause adverse effects in normal cells and tissues. Some cargoes, such as protein and/or nucleic acids, are easily degraded under physiological conditions. To alleviate the side effect and enhance efficacy, development of delivery carriers that envelop drugs or probes is promising and urgent task.

Nanoparticles have higher solubility, bioavailability and cargo-loading. Nanoparticles enhance half-life of cargoes while protecting them from unwanted degradation and preventing indiscriminate diffusion. Physicochemical properties of nanoparticles determine the circulation and biodistribution (Figure 1.2)[2].

Size and shape of nanoparticles

Size and shape of nanoparticles affect to toxicity, biodistribution and half-life. Especially, size and shape are related to uptake of particles. It was reported that 100 nm diameter particles were untaken by target cells 2.5 folded higher than 1um diameter particles[3]. Release of cargo is important as well as uptake of particle for delivery system. As particles have smaller size, it has higher surface to volume ratio, which means that more cargoes are closer to surface of particle. Being near the surface would induce faster cargo release[4]. It would be an advantage for cargo delivery. The size of particles closely related to biological pathway. It has been shown that 20nm diameter particles are rapidly

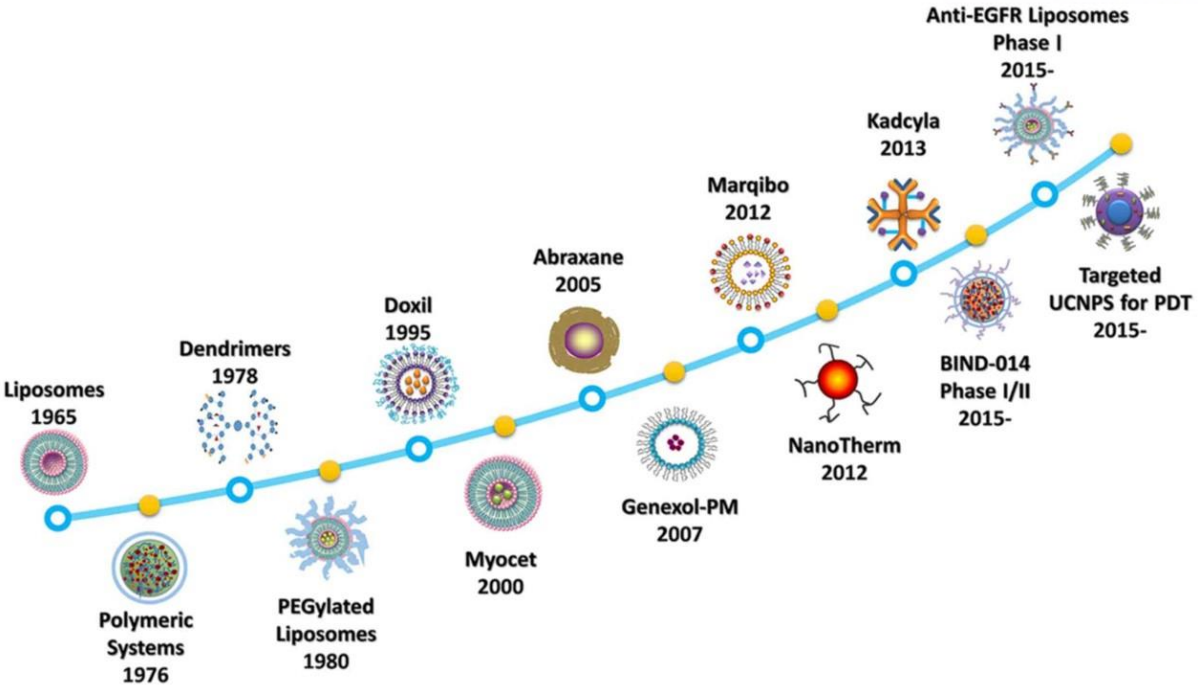

Figure 1.1 Timeline of the development of nanomedicine

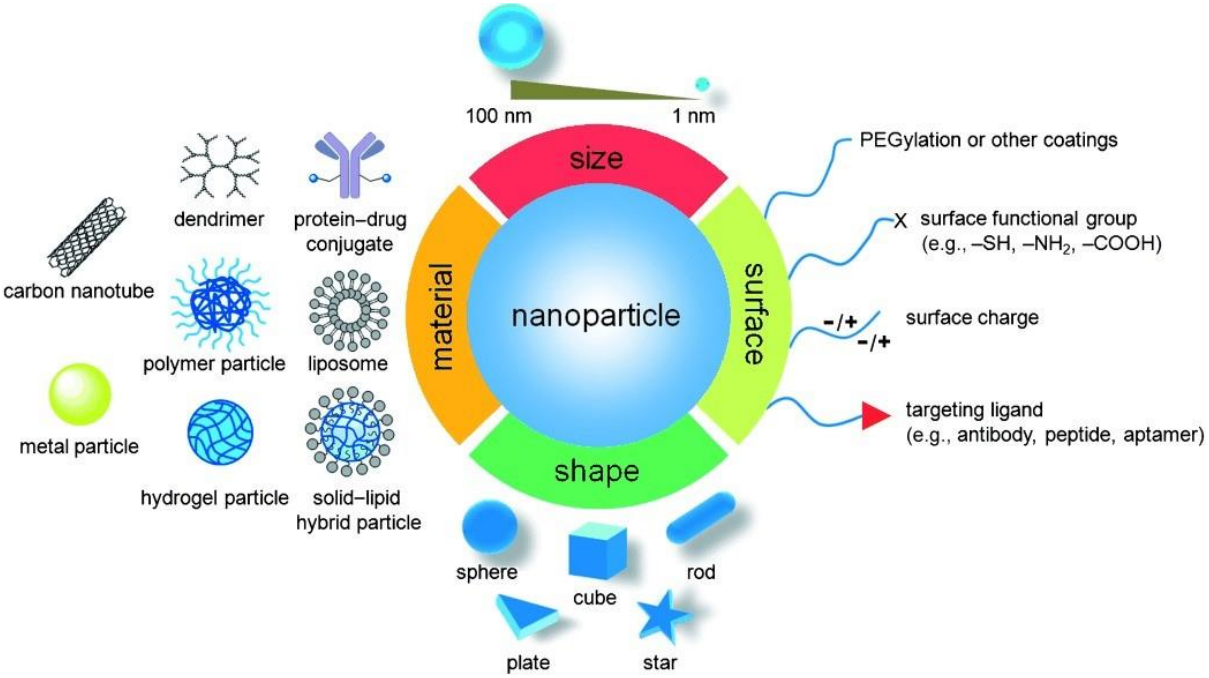

Figure 1.2 Characteristics of nanoparticles as carriers for cargo delivery.

removed by renal clearance and over 200nm diameter particles are removed by lymphatic systems that are responsible for filtering and clearance of foreign materials[5]. The optimal size of particles is approximately 100nm, which could load enough cargo due to high surface to volume ratio and avoid rapid clearance by macrophage dependent immune response.

Cargo loading and release

The size and shape affect properties of nanoparticles, such as bioavailability, biodistribution and toxicity. Even if particles get cargo to target site by controlling these properties, it cannot be used as carriers unless cargoes cannot be released from particles. The release of cargo depends on various factors including temperature, pH, solubility of cargo, desorption and diffusion rate of cargo from particles[6-7]. These factors are determined by the type of nanoparticles being used.

Surface modification

Manipulation of surface of nanoparticles can generate ideal cargo delivery platforms. Incorporation of functional material on nanoparticles can induce enhanced stability, prevention of aggregation and target-specific delivery[8]. Nanoparticles are recognized foreign materials by lymphatic system, which induces natural immune response. Especially, hydrophobic particles are likely to be cleared by indiscriminate binding of blood components. Thus, it is important that making hydrophobic nanoparticles to hydrophilic to increase circulation time. Various polymers or surfactants or proteins have been used for coating materials. PEG is commonly used coating agents, which is hydrophilic and inert polymer. PEGylated nanoparticles can block nonspecific binding of plasma proteins, preventing substantial clearance under blood circulation. Aggregation dependent clearance is also major concern of nanoparticles as well as clearance caused by opsonization. Especially, nanoparticles having high surface area such as micelles, dendrimers and liposomes are easily aggregated. Various approach has been reported to prevent aggregation using coating materials with capping agents and changing the surface charge of particles.

Targeted cargo delivery

Targeted cargo delivery using nanoparticle is important for minimizing side effect and enhancing delivery efficiency. The nanoparticles can penetrate into the damaged tissue due to defective epithelial junctions. This leakage of nanoparticles occurs passively. The leaked nanoparticles can reach lesion site and deliver cargo, while some nanoparticles

reach healthy tissues and induce damage. Thus, active targeting along with passive targeting is required in nanoparticle-based cargo delivery. For active targeting, coating targeting ligand on nanoparticle is a common strategy. Antibodies, peptides, small molecules, aptamers and designed proteins are most common coating materials[9]. Especially, antibodies are widely used as nanoparticle targeting ligand because it is high target specificity, bioavailability, longer half-life and other unique *in vivo* properties. Thus, antibodies have been applied to various nanomaterials including lipid vesicles, dendrimers, micelles and organic/inorganic nanoparticles. Antibodies are chemically conjugated to nanoparticles via modification of antibody fragments and/or modification of nanoparticle surfaces. However, chemical modification often causes some limitations, such as decreased targeting ability of antibodies and destabilization of the antibodies due to modifications of binding sites.

1.1.2 Type of nanoparticles

Liposomes

Liposome is the nanomaterials consisting of aqueous core having one or more phospholipids and cholesterol layer[10]. Liposome can load hydrophilic cargo molecules into aqueous core region and hydrophobic cargo molecules within the lipid bilayer. In addition, composition of liposomes is similar to plasma membrane, resulting in high biocompatibility compared to synthetic carriers. Also, modifications of liposome are possible using modified lipids and cholesterols to stabilize liposome and add functions on interior and exterior surface. Today, several methods to release of drug from liposome have been studied using light, heat, enzyme or ultrasound[11-14]. These liposomes have been combined with targeting ligands to develop targeted drug delivery platforms.

Dendrimers

Dendrimers are macromolecules being nano-sized spherical structure found in nature. Dendrimers are composed of four parts: Central core, branches, repeat units at branch junction, and terminal capping group[15]. The branches of dendrimers can load a myriad of cargoes due to large surface area and release them eventually. And the large number of exposed terminal capping groups having amino acids lead to high biocompatibility and longer half-life in blood circulation. Dendrimers are commonly used as a gene delivery vectors. Especially, high branched dendrimer-aptamers have high affinity and specificity to various kinds of targets[16].

Micelles

Micelles are self-assembled from amphiphilic block copolymers having above the critical micelle concentration[17]. The assembly of copolymer constructs core-shell structure. The core consists of hydrophobic parts of polymer, which can load cargo molecules and protects them being dissolved. On the other hand, the hydrophilic domains including PLA, PLGA and polystyrene form shell structure, which increase the aqueous solubility of micelles[18-19]. In addition, these copolymers are biocompatible and biodegradable, therefore micelles are non-toxic carriers for drug delivery system. For targeted drug delivery, peptides such as integrin-binding peptide and mitochondria-targeting peptide were modified to shell domain and selectively target tumors[20-21]. Besides, several micelles have been widely used for gene transfer, temperature and pH sensing and photodynamic therapy.

Mesoporous silica nanoparticles

Various kinds of inorganic nanoparticles have been used in medical imaging and therapy. Among the inorganic nanoparticles, mesoporous silica nanoparticles (MSNs) have unique properties and potential for biomedical applications. Various morphological structure of MSNs can be produced, having different particle size, pore diameter, pore structure, and surface functionality in controlled manner. High surface and pore volume of MSNs induces higher cargo loading capacity via physical adsorption. In addition, MSNs are inorganic materials that protect various types of cargo molecules from environment factors including enzyme degradation and hyperthermia. Release of drug on targeted tissues is relatively easy when cargo molecules are encapsulated in MSNs compared to other nanomaterials. It is just necessary to block the pore entrance to protect cargo molecules using capping materials before MSNs reach to lesion sites. When cargo loaded MSNs get into targets, those capping materials would detach from pore entrance and trigger the release of cargoes. The stimuli to open the pore entrance includes pH, light, heat, and enzymatic cleavage[6]. Tumor penetration is also important factor to treat solid tumor using nanomaterials as well as stimuli dependent cargo release. The matrix density is higher than healthy tissues, which block the penetration of carriers into the peripheral site of tumor. To enhance tumor penetration, proteolytic enzymes grafted on MSNs and these complexes loosen the matrix and get into tumor site[22]. These physicochemical properties cause MSNs as an ideal drug delivery system.

1.2 Protein nanoparticle-based delivery

1.2.1 Protein cage architectures

Various kinds of nanoparticles are used for biomedical applications to diagnose and treat diseases. Nanoplatforms have a variety of advantages such as longer half-life in blood stream, deep penetration to lesion site, and enhanced cargo loading capacity and these properties make nanoparticles as promising delivery carriers. Though various nanoplatforms including liposomes, micelles and organic/inorganic nanoparticles are developed for drug delivery, these nanoparticles often have heterogenous size, structure and composition, high toxicity and low biodegradability, which make it difficult to utilize in clinical usage.

Protein-based nanoparticles are rising delivery nanoplatforms because these particles are bio-oriented materials having biocompatibility and solubility by chemical and genetic manipulations. Along with these characteristics, protein-based nanoparticles are composed of single subunits, inducing same size and structure. Moreover, crystal structures of these nanoparticles were already identified, which make it possible to design and modify the specific site to give various functionality. Thus, protein-based nanoparticles are promising candidates as cargo carriers for diagnosis and therapy.

Protein cages are self-assembled from multiple copies of single subunits. Most of the protein cages form spherical structure having cavity inside nanoparticles. The protein cage nanoparticles can be classified to three compartments of exterior, interior and interface to impart various functionalities. The cavity provide space to load cargoes such as drugs, probes, enzymes, and polymers to protect them from the physiological conditions. Exterior of nanoparticles can be modified utilized to attach targeting ligands and guest molecules for targeted delivery and interfaces between subunits can be utilized for chimeric assembly and/or symmetry broken architectures. Many studies using protein cage nanoparticles have been investigated for targeted delivery[23]. Here, two type of protein cage nanoparticles will be discussed.

Lumazine synthase (LS)

Lumazine synthase is the enzyme which is related to synthesis of riboflavin. Various kinds of LSs exist from fungi, archaea and some bacteria[24-26]. Among the various LSs, we focused on lumazine synthase from *Aquifex aeolicus* (AaLS) which forms icosahedral structure (T =1) with an outer diameter of 16 nm and inner diameter of 9 nm[27]. Based on the hollow spherical structure of AaLS, it has been used as nanotemplate to load guest molecules. GFP, HIV proteases, and chemical drugs were encapsulated in AaLS and

these platforms showed great potential to enhance pharmacological properties of cargo molecules. As a versatile drug delivery system, cell-targeting peptides including SP94 and RGD4C were genetically inserted to surface of AaLS(Figure 1.3)[28]. Furthermore, AaLS maintains stable structure under high temperature and can be easily modified that impose various functionalities.

P22 virus-like nanoparticles (P22 VLP)

Virus-like particles (VLPs) are commonly used nanoplatforms. Viruses have protein shell called capsid, storing and protecting viral nucleic acids from outside. The viral capsids are beneficial carriers due to its various size, structure and robust symmetry. The virus-like particles are driven from plant viruses (CMV, CCMV and TMV), bacteriophage (P22, MS2, and M13) and animal viruses (HBV, papilomavirus).

VLP derived from the *salmonella typhimurium* bacteriophage P22 are self-assembled to procapsid from 420 copies of identical coat proteins and 100-300 copies of scaffolding protein[29]. Scaffolding proteins support assembly of coat proteins via noncovalent interactions. The unique attribute of P22 VLP is structure change through external stimuli and P22 VLP morphologies can be controlled. When P22 self-assemble into the capsids, the capsid forms spherical structure, procapsid (PC), including scaffolding protein inside the capsid. When scaffolding proteins are eliminated, the capsids retain empty shell (ES) morphology. The PC and ES can be transformed to expanded (EX) morphology by heat treatments at 65 ºC, causing change of diameter from 56nm to 62nm and decreased pore size. Furthermore, heating the capsid at 75 ºC induces the loss of 12 icosahedral pentamers, forming 10nm pores at five-fold axis and results in hollow nanostructure known as wiffle ball (WB) (Figure 1.4)[30].

P22 VLP is commonly manipulated as cargo vehicles because it has relatively large interior space and pore which make it possible to translocate cargo molecules between protein shells. Anti-cancer drugs, BTZ and Doxorubicin, were loaded interior surface of P22 VLP and hepatocellular carcinoma targeting peptides, SP94, were genetically modified to exterior surface[31]. Besides the small molecules, enzymes were encapsulated within P22 VLP to sequester from outside factors. Hydrogenases were encapsulated into the P22 VLP to produce hydrogen which is renewable fuels. The new catalytic system was sustainable against air, heat or other factors[32]. Also, P22 VLP has been used for intermolecular communications of functional materials due to confined and dense interior space. P22 VLP can provide enough space for enzyme cascade because a series of

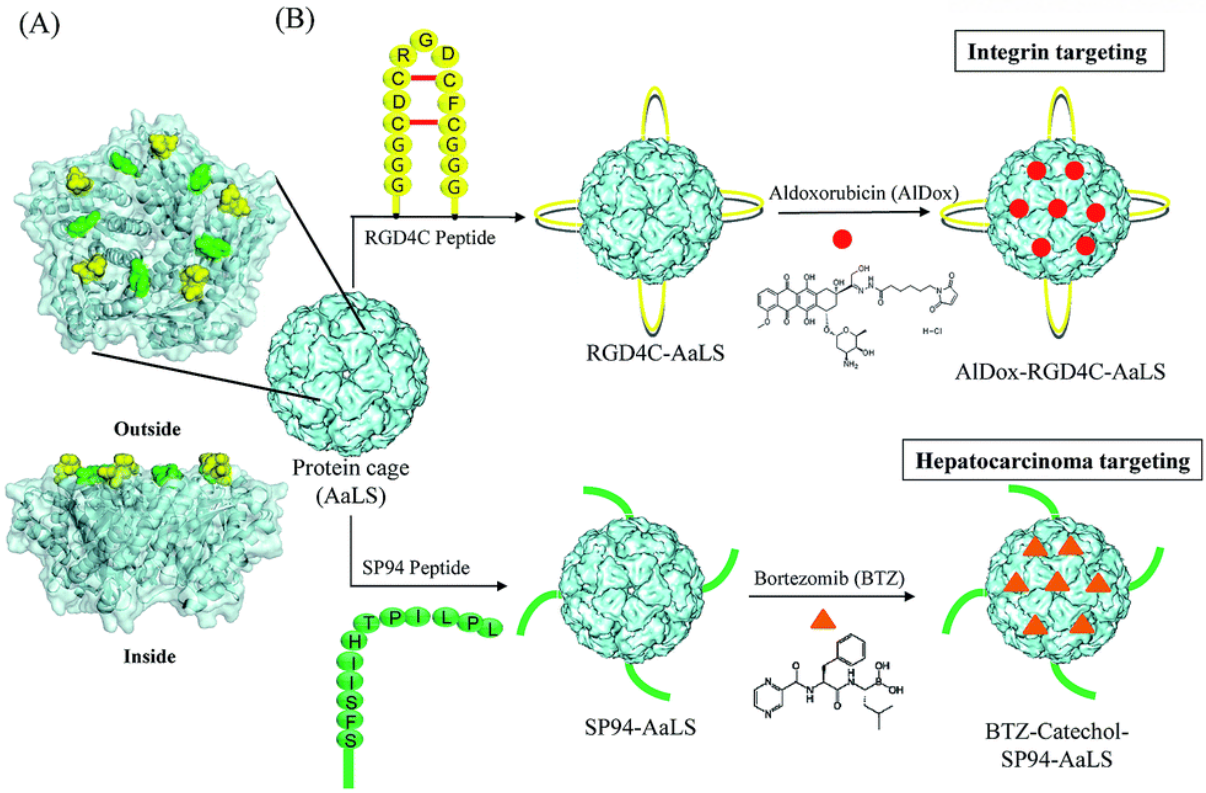

Figure 1.3 Targeted delivery modular platforms using AaLS with targeting peptide.

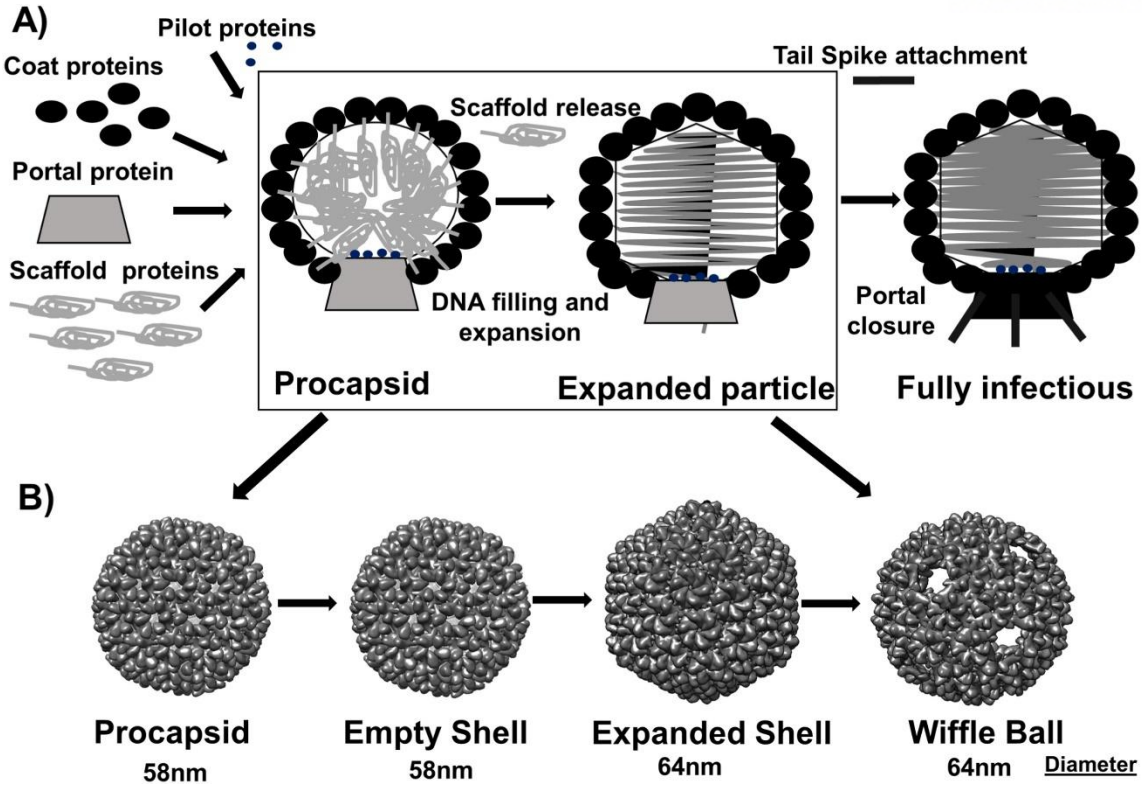

Figure 1.4 Capsid formation and topological change of P22.

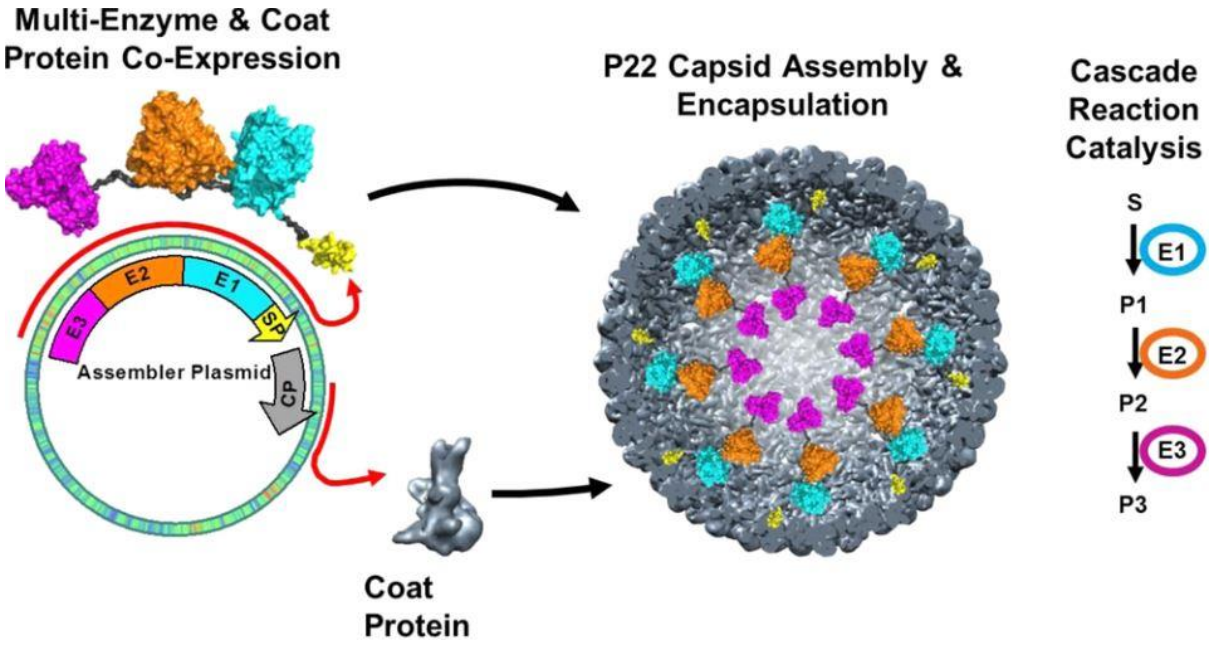

Figure 1.5 Encapsulation of enzyme cascade within P22 VLP.

enzymes can be packed. To mimic sugar metabolism of *Pyrococcus furiosus*, three enzymes including CelB, GALK, and GLUK were co-encapsulated within P22 VLP, which system performed a cascade of coupled reaction (Figure 1.5)[33]. In addition, P22 VLPs were used as nanotemplates to produce high-density environment using ATRP within limited space. This approach was useful to encapsulate lots of catalyst or contrast agents that showed better efficiency as more molecules were loaded.

1.2.2 Protein engineering

Protein engineering is the term that developing useful proteins on demand. There are many strategies to modify the protein. Here, chemical and genetic modification of proteins are introduced.

Chemical modifications

Chemical modification is powerful tools to conjugate probes, therapeutic drugs, and build protein constructs. Cysteine and lysine residues are major targets for the site-specific modifications. Low abundance of cysteine can cause facile modification of single site. Furthermore, the cysteine residue can be removed and inserted by codon reassignment. There are various strategies to modify the cysteine residues such as aminoethylation, iodoacetamides, maleimides, Dha formation and disulfide formations[34-37]. Lysine residue is another choice for modifications where multiple conjugations are necessary. For the preferential modifications of amine of lysine, electrophiles including activated esters, sulfonyl chlorides or isothiocyanates have been used[38-39]. In addition, unsaturated aldehyde esters react with lysine residues by selective azo-electrocyclizations[40].

Genetic modifications

Genetic modification is the direct manipulation of genes. Rational designed DNA is made by removing and insertion of the gene materials using recombinant DNA method for desired phonotype. Insertion of candidate DNA to host is the widely used genetic technique to develop multifunctional fusion proteins. In addition, point mutation which changes one or two bases to switch a single amino acid has been also used. The genetic modification has been applied in many fields including biomedical research, industry, and agriculture.

1.2.3 Functional proteins

Antibody binding domain (Z domain)

Antibody binding domain named Z domain was engineered from B domain of immunoglobulin-binding region of staphylococcal protein A[41]. B domain has binding affinity to both Fc and Fab region, which affect the binding of antibodies to their targets. To solve this problem, key amino acids related antibody binding region of B domain were mutated and this resulting engineered protein is Z domain[42]. The Z domain has enhanced stability and selective binding affinity to Fc parts of antibodies which are isolated from various animal. Using the properties of Z domain, modular drug delivery systems have been developed.

Affibody molecules

Antibodies is the most common targeting ligands in diagnosis and therapeutics due to strong binding and high selectivity to target receptor. However, antibodies have large, complex glycosylation pattern and disulfide bond dependent structure, leading to low stability and expensive and laborious manufacturing steps. Recently, a variety of artificial targeting ligands were developed to replace antibodies. Affibody molecules are one of alternative for antibodies (Figure 1.6)[43]. Affibody molecules consist of 58 amino acids without cysteine and has small molecular weight about 6 kDa as well as high solubility and stability. Affibody molecules libraries are constructed by genetic modification of 13 amino acid position of helices one and two of the B domain[44-45]. These affibody molecules showed specific binding to target molecules (e.g TNF-α, EGFR, HER2, IgA, IgE and IgM) with strong binding affinity approximately in the μM to pM range[46]. Some affibody molecules having low binding affinity were mutated by helix shuffling or sequence alignment. Furthermore, the structural properties including small size and simple composition mean that affibody molecules are genetically fused with various functional proteins, retaining targeting ability, solubility and stability of fusion proteins[47]. Now, the clinical applications of affibody molecules are explored in diagnostic imaging and therapeutics to improve efficiency as an alternative of the conventional antibodies.

Bacterial superglue; SpyTag and SpyCatcher

SpyTag and SpyCatcher are driven from the immunoglobulin-like collagen adhesin domain (CnaB2) from the fibronectin binding protein FbaB, found in *streptococcus pygenes*[48]. CnaB2 domain is split into two fragments, which one is N-terminal protein

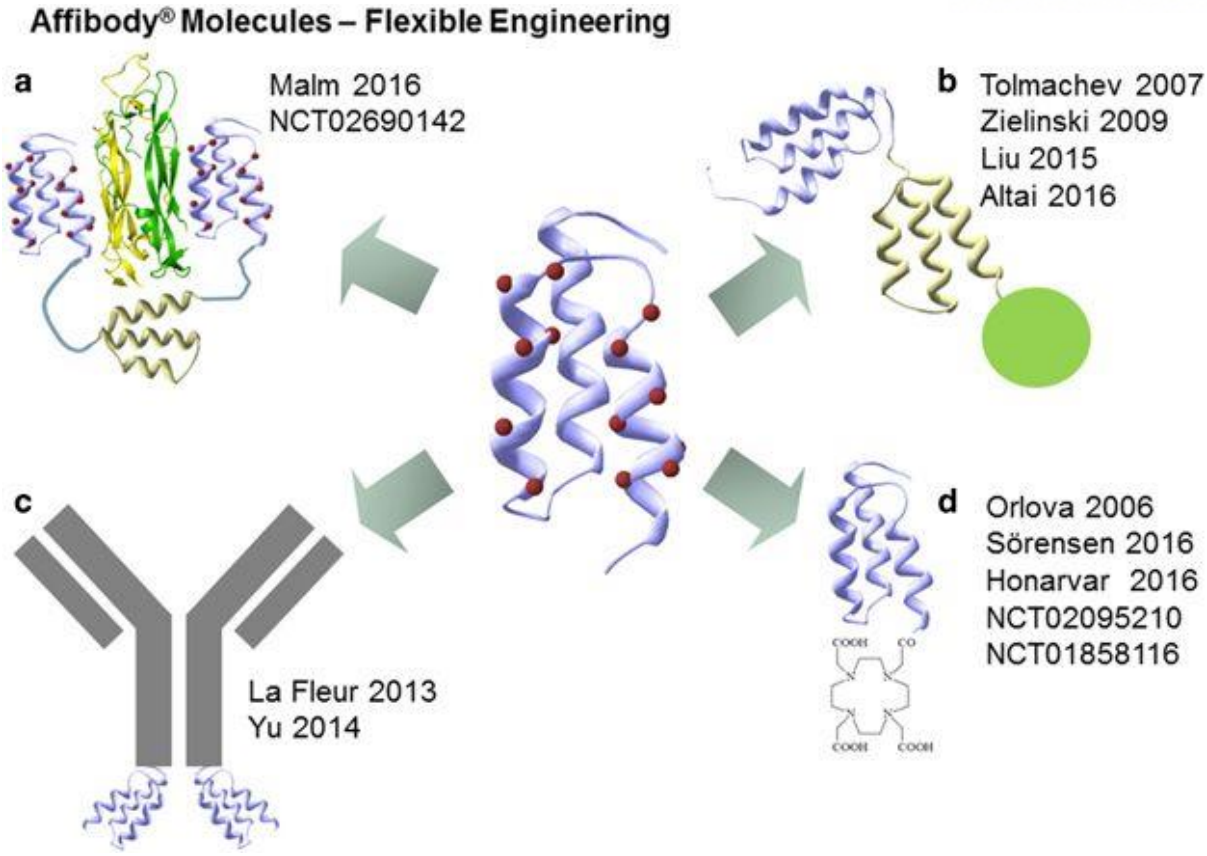

Figure 1.6 Affibody molecules engineered in various formats.

fragment named SpyCatcher and the other is C-terminal 13 amino acids(AHIVMVDATKPTK) peptide named SpyTag. These two parts spontaneously form isopeptide bond between Lys31 of SpyCatcher and Asp117 of SpyTag (Figure 1.7)[48]. This covalent reaction occurs under various pH, temperature, redox conditions and in detergents. Also, SpyTag and SpyCatcher maintain reactivity where individual parts are located N-terminal, C-terminal and even internal position of protein unlike to other tagging proteins. Both SpyTag and SpyCatcher could be fused with functional proteins located in vitro and in vivo and maintain the function of fused proteins. Recently, this bacterial superglue system has been widely used for biomedical applications. Using the SpyTag/SpyCatcher interaction, novel enzyme assemblies are developed (Figure 1.8)[49]. The fusion protein of SpyCatcher and horseradish peroxidase assemble with various enzyme complexes, arabinofuranosidase and endoxylanase to enhance sugar conversion through spatial proximity of enzymes[50]. This tool has been also applied for displaying functional proteins on surface of bacteria and virus (Figure 1.9)[49, 51]. Antigens and targeting ligands were post-translationally attached to virus-like particle and showed improved immune response and gene delivery.

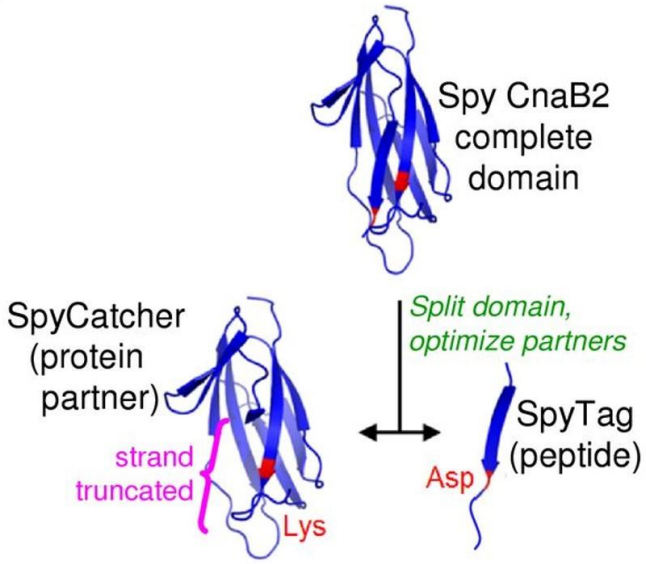

Figure 1.7 Isopeptide formation between SpyTag and SpyCatcher.

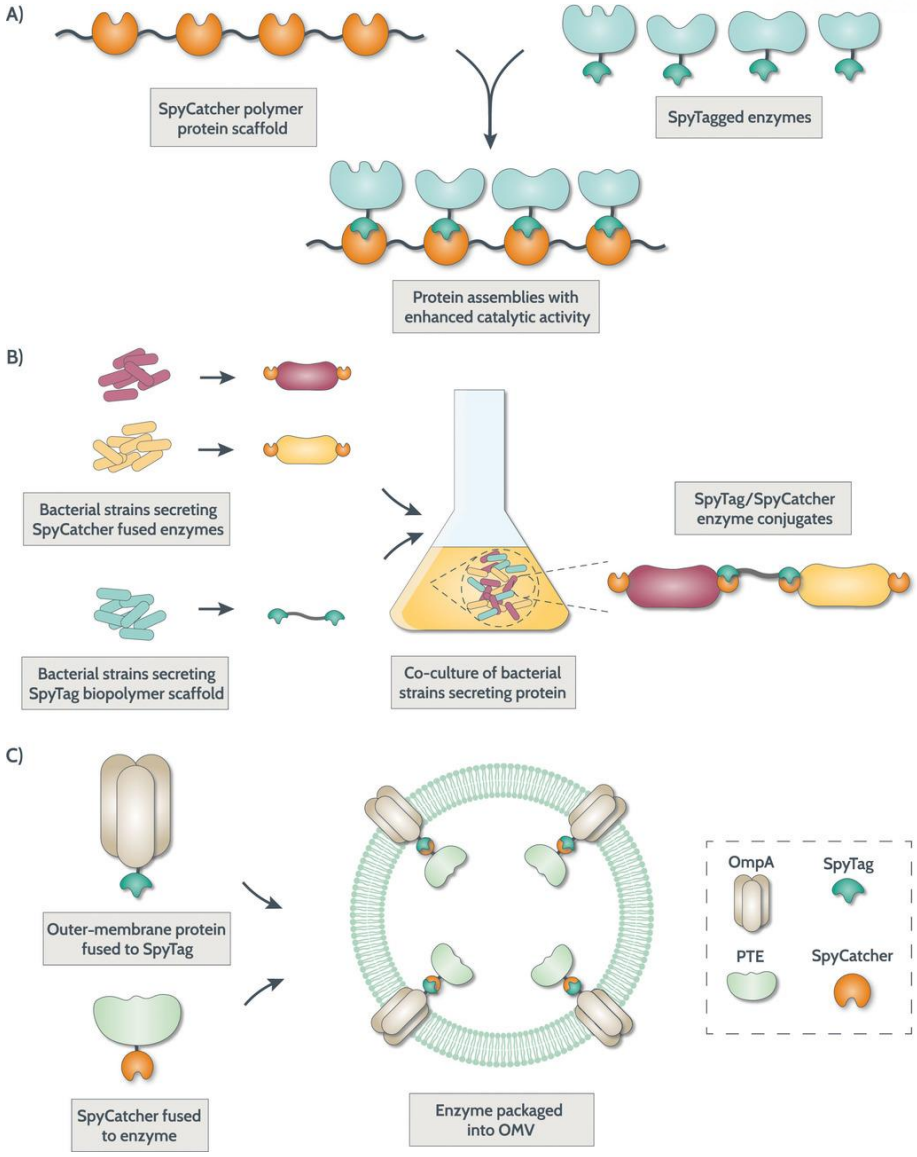

Figure 1.8 Novel enzyme assemblies using SpyTag/SpyCatcher.

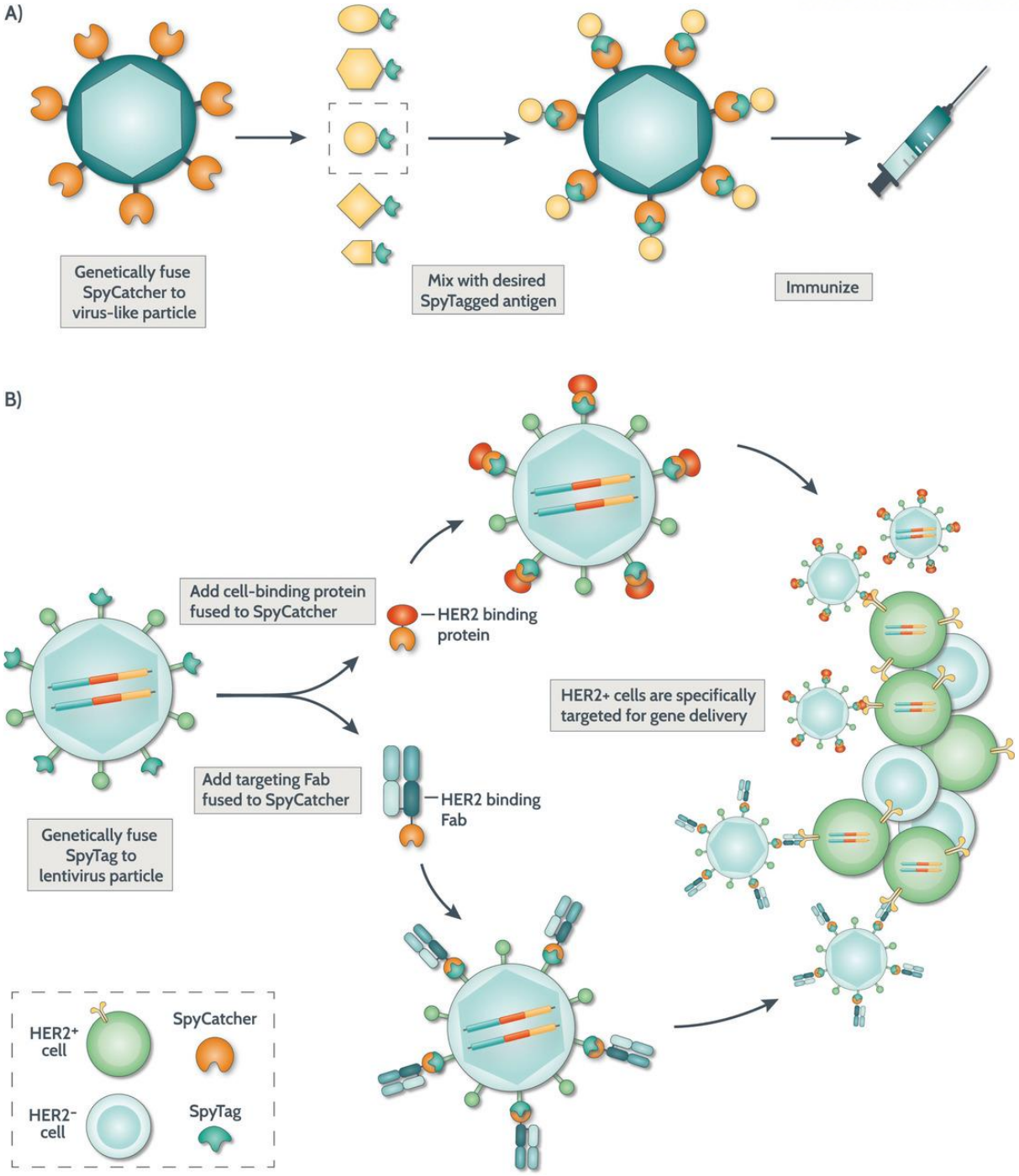

Figure 1.9 Display functional proteins on viral capsid using SpyTag/SpyCatcher.

1.3 Reference

1. Li, Z.; Tan, S. R.; Li, S.; Shen, Q.; Wang, K. H., Cancer drug delivery in the nano era: An overview and perspectives (Review). *Oncol Rep* **2017,** *38* (2), 611-624.
2. Sun, T. M.; Zhang, Y. S.; Pang, B.; Hyun, D. C.; Yang, M. X.; Xia, Y. N., Engineered Nanoparticles for Drug Delivery in Cancer Therapy. *Angew Chem Int Edit* **2014,** *53* (46), 12320-12364.
3. Desai, M. P.; Labhasetwar, V.; Walter, E.; Levy, R. J.; Amidon, G. L., The mechanism of uptake of biodegradable microparticles in Caco-2 cells is size dependent. *Pharm Res-Dordr* **1997,** *14* (11), 1568-1573.
4. Buzea, C.; Pacheco, I. I.; Robbie, K., Nanomaterials and nanoparticles: Sources and toxicity. *Biointerphases* **2007,** *2* (4), Mr17-Mr71.
5. Prokop, A.; Davidson, J. M., Nanovehicular intracellular delivery systems. *J Pharm Sci-Us* **2008,** *97* (9), 3518-3590.
6. Mura, S.; Nicolas, J.; Couvreur, P., Stimuli-responsive nanocarriers for drug delivery. *Nat Mater* **2013,** *12* (11), 991-1003.
7. Siepmann, J.; Gopferich, A., Mathematical modeling of bioerodible, polymeric drug delivery systems. *Adv Drug Deliver Rev* **2001,** *48* (2-3), 229-247.
8. Khanbabaie, R.; Jahanshahi, M., Revolutionary Impact of Nanodrug Delivery on Neuroscience. *Curr Neuropharmacol* **2012,** *10* (4), 370-392.
9. Friedman, A. D.; Claypool, S. E.; Liu, R., The Smart Targeting of Nanoparticles. *Curr Pharm Design* **2013,** *19* (35), 6315-6329.
10. Gulati, M.; Grover, M.; Singh, S.; Singh, M., Lipophilic drug derivatives in liposomes. *Int J Pharmaceut* **1998,** *165* (2), 129-168.
11. Papahadjopoulos, D.; Jacobson, K.; Nir, S.; Isac, T., Phase transitions in phospholipid vesicles. Fluorescence polarization and permeability measurements concerning the effect of temperature and cholesterol. *Biochim Biophys Acta* **1973,** *311* (3), 330-48.
12. Huang, S. L.; MacDonald, R. C., Acoustically active liposomes for drug encapsulation and ultrasound-triggered release. *Biochim Biophys Acta* **2004,** *1665* (1-2), 134-41.
13. Pak, C. C.; Erukulla, R. K.; Ahl, P. L.; Janoff, A. S.; Meers, P., Elastase activated liposomal delivery to nucleated cells. *Bba-Biomembranes* **1999,** *1419* (2), 111-126.
14. Gerasimov, O. V.; Boomer, J. A.; Qualls, M. M.; Thompson, D. H., Cytosolic drug delivery using pH- and light-sensitive liposomes. *Adv Drug Deliver Rev* **1999,** *38* (3), 317-338.
15. Kesharwani, P.; Jain, K.; Jain, N. K., Dendrimer as nanocarrier for drug delivery. *Prog Polym Sci* **2014,** *39* (2), 268-307.

16. Liu, H. M.; Wang, Y.; Wang, M. M.; Xiao, J. R.; Cheng, Y. Y., Fluorinated poly(propylenimine) dendrimers as gene vectors. *Biomaterials* **2014,** *35* (20), 5407-5413.

17. Sun, T. M.; Du, J. Z.; Yan, L. F.; Mao, H. Q.; Wang, J., Self-assembled biodegradable micellar nanoparticles of amphiphilic and cationic block copolymer for siRNA delivery. *Biomaterials* **2008,** *29* (32), 4348-4355.

18. Rabanel, J. M.; Faivre, J.; Tehrani, S. F.; Lalloz, A.; Hildgen, P.; Banquy, X., Effect of the Polymer Architecture on the Structural and Biophysical Properties of PEG-PLA Nanoparticles. *Acs Appl Mater Inter* **2015,** *7* (19), 10374-10385.

19. Gundogdu, N.; Cetin, M., Chitosan-poly (lactide-co-glycolide) (CS-PLGA) nanoparticles containing metformin HCl: Preparation and in vitro evaluation. *Pak J Pharm Sci* **2014,** *27* (6), 1923-1929.

20. Jung, H. S.; Han, J.; Lee, J. H.; Lee, J. H.; Choi, J. M.; Kweon, H. S.; Han, J. H.; Kim, J. H.; Byun, K. M.; Jung, J. H.; Kang, C.; Kim, J. S., Enhanced NIR Radiation-Triggered Hyperthermia by Mitochondrial Targeting. *Journal of the American Chemical Society* **2015,** *137* (8), 3017-3023.

21. Gao, Y. J.; Zhou, Y. X.; Zhao, L.; Zhang, C.; Li, Y. S.; Li, J. W.; Li, X. R.; Liu, Y., Enhanced antitumor efficacy by cyclic RGDyK-conjugated and paclitaxel-loaded pH-responsive polymeric micelles. *Acta Biomater* **2015,** *23*, 127-135.

22. Villegas, M. R.; Baeza, A.; Vallet-Regi, M., Hybrid Collagenase Nanocapsules for Enhanced Nanocarrier Penetration in Tumoral Tissues. *Acs Appl Mater Inter* **2015,** *7* (43), 24075-24081.

23. MaHam, A.; Tang, Z. W.; Wu, H.; Wang, J.; Lin, Y. H., Protein-Based Nanomedicine Platforms for Drug Delivery. *Small* **2009,** *5* (15), 1706-1721.

24. Persson, K.; Schneider, G.; Jordan, D. B.; Viitanen, P. V.; Sandalova, T., Crystal structure analysis of a pentameric fungal and an icosahedral plant lumazine synthase reveals the structural basis for differences in assembly. *Protein Sci* **1999,** *8* (11), 2355-2365.

25. Meining, W.; Mortl, S.; Fischer, M.; Cushman, M.; Bacher, A.; Ladenstein, R., The atomic structure of pentameric lumazine synthase from Saccharomyces cerevisiae at 1.85 A resolution reveals the binding mode of a phosphonate intermediate analogue. *J Mol Biol* **2000,** *299* (1), 181-97.

26. Morgunova, E.; Meining, W.; Illarionov, B.; Haase, I.; Jin, G. Y.; Bacher, A.; Cushman, M.; Fischer, M.; Ladenstein, R., Crystal structure of lumazine synthase from Mycobacterium tuberculosis as a target for rational drug design: Binding mode of a new class of purinetrione inhibitors. *Biochemistry* **2005,** *44* (8), 2746-2758.

27. Bacher, A.; Baur, R.; Eggers, U.; Harders, H. D.; Otto, M. K.; Schnepple, H., Riboflavin Synthases of Bacillus-Subtilis - Purification and Properties. *J Biol Chem* **1980,** *255* (2), 632-637.

28. Min, J.; Kim, S.; Lee, J.; Kang, S., Lumazine synthase protein cage nanoparticles as modular delivery platforms for targeted drug delivery. *Rsc Adv* **2014,** *4* (89), 48596-48600.

29. Patterson, D. P.; Prevelige, P. E.; Douglas, T., Nanoreactors by Programmed Enzyme

Encapsulation Inside the Capsid of the Bacteriophage P22. *Acs Nano* **2012,** *6* (6), 5000-5009.

30. Kant, R.; Llauro, A.; Rayaprolu, V.; Qazi, S.; de Pablo, P. J.; Douglas, T.; Bothner, B., Changes in the stability and biomechanics of P22 bacteriophage capsid during maturation. *Bba-Gen Subjects* **2018,** *1862* (6), 1492-1504.

31. Moon, H.; Lee, J.; Min, J.; Kang, S., Developing genetically engineered encapsulin protein cage nanoparticles as a targeted delivery nanoplatform. *Biomacromolecules* **2014,** *15* (10), 3794-801.

32. Kang, S. B.; Prevelige, P. E., Domain study of bacteriophage P22 coat protein and characterization of the capsid lattice transformation by hydrogen/deuterium exchange. *Journal of Molecular Biology* **2005,** *347* (5), 935-948.

33. Patterson, D. P.; Schwarz, B.; Waters, R. S.; Gedeon, T.; Douglas, T., Encapsulation of an Enzyme Cascade within the Bacteriophage P22 Virus-Like Particle. *Acs Chem Biol* **2014,** *9* (2), 359-365.

34. Lundell, N.; Schreitmuller, T., Sample preparation for peptide mapping - A pharmaceutical quality-control perspective. *Anal Biochem* **1999,** *266* (1), 31-47.

35. Smith, M. E. B.; Schumacher, F. F.; Ryan, C. P.; Tedaldi, L. M.; Papaioannou, D.; Waksman, G.; Caddick, S.; Baker, J. R., Protein Modification, Bioconjugation, and Disulfide Bridging Using Bromomaleimides. *Journal of the American Chemical Society* **2010,** *132* (6), 1960-1965.

36. Simon, M. D.; Chu, F. X.; Racki, L. R.; de la Cruz, C. C.; Burlingame, A. L.; Panning, B.; Narlikar, G. J.; Shokat, K. M., The site-specific installation of methyl-lysine analogs into recombinant histones. *Cell* **2007,** *128* (5), 1003-1012.

37. Kenyon, G. L.; Bruice, T. W., Novel sulfhydryl reagents. *Methods Enzymol* **1977,** *47*, 407-30.

38. Kalkhof, S.; Sinz, A., Chances and pitfalls of chemical cross-linking with amine-reactive N-hydroxysuccinimide esters. *Anal Bioanal Chem* **2008,** *392* (1-2), 305-312.

39. Nakamura, T.; Kawai, Y.; Kitamoto, N.; Osawa, T.; Kato, Y., Covalent Modification of Lysine Residues by Allyl Isothiocyanate in Physiological Conditions: Plausible Transformation of Isothiocyanate from Thiol to Amine. *Chem Res Toxicol* **2009,** *22* (3), 536-542.

40. Tanaka, K.; Masuyama, T.; Hasegawa, K.; Tahara, T.; Mizuma, H.; Wada, Y.; Watanabe, Y.; Fukase, K., A submicrogram-scale protocol for biomolecule-based PET imaging by rapid 6 pi-azaelectrocyclization: Visualization of sialic acid dependent circulatory residence of glycoproteins. *Angew Chem Int Edit* **2008,** *47* (1), 102-105.

41. Uhlen, M.; Guss, B.; Nilsson, B.; Gatenbeck, S.; Philipson, L.; Lindberg, M., Complete Sequence of the Staphylococcal Gene Encoding Protein-a - a Gene Evolved through Multiple Duplications. *J Biol Chem* **1984,** *259* (3), 1695-1702.

42. Nilsson, B.; Moks, T.; Jansson, B.; Abrahmsen, L.; Elmblad, A.; Holmgren, E.; Henrichson, C.; Jones, T. A.; Uhlen, M., A Synthetic Igg-Binding Domain Based on Staphylococcal Protein-A. *Protein Eng* **1987,** *1* (2), 107-113.

43. Frejd, F. Y.; Kim, K. T., Affibody molecules as engineered protein drugs. *Exp Mol Med* **2017,** *49*.

44. Nord, K.; Nilsson, J.; Nilsson, B.; Uhlen, M.; Nygren, P. A., A Combinatorial Library of an Alpha-Helical Bacterial Receptor Domain. *Protein Eng* **1995,** *8* (6), 601-608.

45. Nord, K.; Gunneriusson, E.; Ringdahl, J.; Stahl, S.; Uhlen, M.; Nygren, P. A., Binding proteins selected from combinatorial libraries of an alpha-helical bacterial receptor domain. *Nat Biotechnol* **1997,** *15* (8), 772-777.

46. Nygren, P. A., Alternative binding proteins: Affibody binding proteins developed from a small three-helix bundle scaffold. *Febs J* **2008,** *275* (11), 2668-2676.

47. Friedman, M.; Lindstrom, S.; Ekerljung, L.; Andersson-Svahn, H.; Carlsson, J.; Brismar, H.; Gedda, L.; Frejd, F. Y.; Stahl, S., Engineering and characterization of a bispecific HER2 x EGFR-binding affibody molecule. *Biotechnol Appl Bioc* **2009,** *54*, 121-131.

48. Zakeri, B.; Fierer, J. O.; Celik, E.; Chittock, E. C.; Schwarz-Linek, U.; Moy, V. T.; Howarth, M., Peptide tag forming a rapid covalent bond to a protein, through engineering a bacterial adhesin. *P Natl Acad Sci USA* **2012,** *109* (12), E690-E697.

49. Sutherland, A. R.; Alam, M. K.; Geyer, C. R., Post-translational Assembly of Protein Parts into Complex Devices by Using SpyTag/SpyCatcher Protein Ligase. *Chembiochem* **2019,** *20* (3), 319-328.

50. Jia, L. L.; Minamihata, K.; Ichinose, H.; Tsumoto, K.; Kamiya, N., Polymeric SpyCatcher Scaffold Enables Bioconjugation in a Ratio-Controllable Manner. *Biotechnol J* **2017,** *12* (12).

51. Brune, K. D.; Leneghan, D. B.; Brian, I. J.; Ishizuka, A. S.; Bachmann, M. F.; Draper, S. J.; Biswas, S.; Howarth, M., Plug-and-Display: decoration of Virus-Like Particles via isopeptide bonds for modular immunization. *Sci Rep-Uk* **2016,** *6*.

Chapter 2. Development of an antibody-binding modular nanoplatform for antibody-guided targeted cell imaging and delivery

2.1 Introduction

For many biotechnological and biomedical applications and *in vivo* and/or *in vitro* diagnostics, target specificity and high binding affinity to any given target molecules are essential features. Antibodies have extremely high binding affinity and specificity for their target molecules, and a variety of antibodies against virtually any desired targets can be readily obtained on demand.[1–5] Therefore, antibodies have been widely used as ligands for targeted delivery of various therapeutics and/or diagnostics and specific detection of biomarkers *in vitro* and/or *in vivo*. As targeting ligands, antibodies are generally chemically conjugated to functional modules, such as delivery vehicles, enzymes, chemicals, or any other supporting materials.[6–10] However, chemical conjugation and the related approaches often suffer from decreased affinity and specificity of antibodies generally due to alterations in their target binding sites or destabilization and random orientation of the antibodies.[4,11] Therefore, it is necessary to develop a nanoplatform that achieves oriented display of antibodies on the surface without the loss of the essential properties of the antibodies: high affinity and specificity. In addition, a potential nanoplatform should have structural plasticity that acquires additional functionalities on demand as well as a structural uniformity that ensures reproducible outcomes.

Lumazine synthase protein cage nanoparticle isolated from the hyperthermophile *Aquifex aeolicus* (AaLS) is a nanocage-forming enzyme that consists of 60 identical subunits with an exterior diameter of 15.4 nm and an 8 nm interior cavity,[12] and catalyzes the penultimate step in the synthesis of riboflavin.[13] Its hollow spherical architecture has been used as a template for the encapsulation of cargo proteins, such as green fluorescent protein,[14,15] HIV protease,[16] and ferritin,[17] by engineering the electrostatic properties of its interior surface and the biomineralization of iron oxide nanoparticles.[18] AaLS has also been utilized as a building block for fabricating uniform layer-by-layer (LbL) assemblies[19] and as a nanoplatform for developing a versatile drug delivery vehicle.[20,21] Similar to the other protein cage nanoparticles, such as ferritin, virus-like particles and encapsulin, AaLS has a uniform size distribution and a symmetric and well-defined multivalent structure.[12] Furthermore, AaLS exhibits an unusual heat stability and genetic and chemical versatility that allows it to acquire multiple functionalities simultaneously.[19–21]

In this study, we constructed a universal multivalent antibody-binding nanoplatform by genetically introducing antibody-binding domains (ABDs) to the surface of lumazine synthase protein cage nanoparticles isolated from the hyperthermophile *Aquifex aeolicus* (AaLS). We demonstrate that the resulting ABD–AaLS effectively captures various types of antibodies derived from diverse species on

demand, and that their complexes selectively recognize and bind to their target cells *in vitro*, guided by antibodies displayed on the surface of ABD–AaLS (Scheme 2.1).

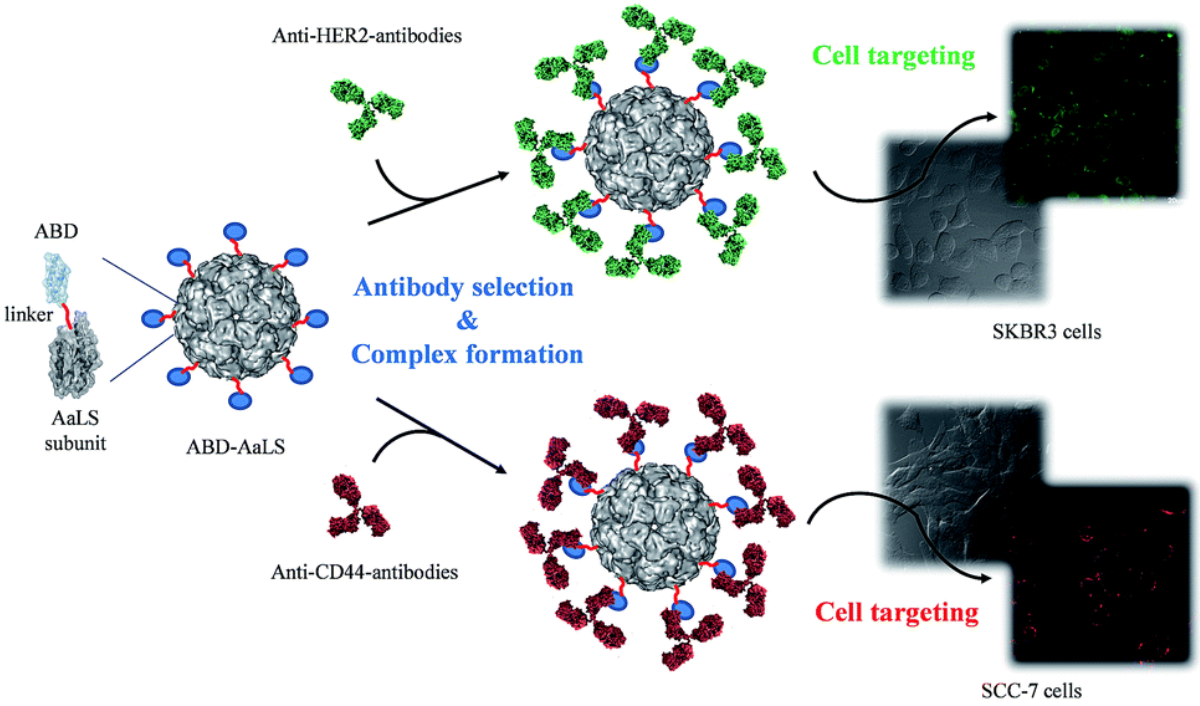

Scheme 2.1 Construction of ABD-AaLS protein cage nanoparticle and its application for fluorescent cell imaging as polyvalent antibody-displaying nanoplatforms.

2.2 Materials and Methods

Construction and purification of antibody-binding domain displaying AaLS (ABD–AaLS) protein cage nanoparticles

The IPTG inducible pET-30b based plasmids containing genes encoding wild-type AaLS protein was prepared and used as templates. The optimized antibody-binding domain (ABD) was synthesized and subcloned into the C-terminus of AaLS gene with extra linker residues. We introduced 26 amino acid residues to provide sufficient flexibility and space for antibody binding. The amplifed DNAs were used to transform the competent E. coli strain BL21 (DE), resulting in the overexpression in E. coli of the ABD–AaLS protein cage nanoparticles.

Quartz crystal microbalance (QCM) measurements

QCM experiments were performed using Q-Sense E4 and standard gold QCM sensors (Q-Sense, Sweden) as described previously, with slight modifications.4 Briefly, the system was operated in flow mode with a pump and temperature was maintained at 25.0 ± 0.1 C. Each sample solution was introduced to the measurement chamber with a pump and continuously measured for 10 min prior to the subsequent introductions. AaLS and ABD–AaLS and various IgGs (rabbit, rat, and mouse) were introduced at concentrations of approximately 100 mg ml^{-1} and 50 mg ml^{-1}, respectively, in phosphate buffer (50 mM phosphate, 100 mM NaCl, pH 6.5). Resonance frequencies were measured simultaneously at seven harmonics (5, 15, 25, 35, 45, 55 and 65 MHz). For clarity, only the normalized frequency of the third overtone is shown.

Surface plasmon resonance (SPR) analysis

SPR experiments were performed with carboxyl dextran CM5 gold chips on a Biacore 3000 device (Biacore AB, Sweden) at 25 C using a PBS buffer as a running solution. Rabbit, rat, or mouse IgGs were coupled to the surface of a CM5 sensor chip by standard amine-coupling chemistry on the SPR instrument as described previously, with slight modifications.[4,22] Briefly, a mixture of EDC (0.4 M) and NHS (0.6 M) was injected onto the chip at a flow rate of 10 ml min^{-1} to activate carboxyl groups on the sensor surface and subsequently 20 mg ml^{-1} of rabbit, rat, or mouse IgGs were added at the same flow rate for 7 min. Excess reactive groups were blocked with 1 M ethanolamine (pH 8.0). ABD–AaLS captures by rabbit, rat, or mouse IgGs were examined by applying various amounts (30, 60, 120, 240, and 400 nM) of ABD–AaLS (PBS, pH 7.4) to the surface at a flow rate of 30 ml min^{-1}. AaLS was applied in parallel as a control.

Cell culture and fluorescence cell microscopy

SKBR3 was obtained from the American Type Culture Collection (ATCC, Manassas, VA) and SCC-7

and KB cells were obtained from the Korean cell line bank (KCLB). SKBR3 cells were cultured in Dulbecco's Modified Eagle's Medium (DMEM) supplemented with 10% (v/v) fetal bovine serum (FBS, Invitrogen Corp., Carlsbad, CA) and antibiotics (100 mg ml^{-1} penicillin and 50 mg ml^{-1} streptomycin) at 37 C under 5% CO2. SCC-7 cells were cultured in RPMI1640 supplemented with 10% FBS and 1% penicillin–streptomycin and KB cells were cultured in RPMI1640 medium with L-glutamine (300 mg l^{-1}), 10% FBS, 25 mM HEPES and 25 mM NaHCO3. SKBR3, SCC-7, and KB cells (2 x 10^4 per well) were grown in 8-well microscopy chambers (Ibidi GmbH, Martinsried, Germany). $^{-1}$ The combinations of fABD–AaLS (final 50 nM) and Alexa-HER2-Ab or HER2-Ab (rabbit IgG, final 200 nM), fABD–AaLS (final 50 nM) and Alexa-CD44-Ab or CD44-Ab (rat IgG, final 200 nM), or fABD–AaLS (final 50 nM) and Alexa-integrin-Ab or integrin-Ab (mouse IgG, final 200 nM) were mixed in DMEM supplemented with 10% (v/v) FBS, antibiotics, and 0.05% Tween 20, and incubated at room temperature for 30 min. The individual mixtures of fABD–AaLS and various IgGs were added to corresponding cell culture wells and incubated at 37 C for 30 min. The cells were washed three times with PBS containing 0.05% Tween 20 and mixed with 4% paraformaldehyde at room temperature for 20 min, and again washed with PBS. The cells were incubated with 4,6-diamidino-2-phenylindole (DAPI, Sigma) in PBS for 10 min and washed with PBS. Fluorescence images are obtained using a Personal DV microscope (Applied Precision, Washington, USA).

2.3 Results and discussion

We first synthesized a gene that encodes the ABD of protein A to construct an AaLS-based multivalent antibody-binding nanoplatform. Protein A and G have been widely used as ligands for purifying various types of antibodies, because they selectively capture antibodies with high affinity.[11,26] In particular, the ABD of protein A (the so-called Z-domain) is known to exclusively bind to the Fc region of various types of antibodies.[27–30] We also genetically engineered AaLS by replacing arginine 108 with cysteine (R108C) for later use in site-specific modification with diagnostic probes such as fluorescent dyes.[19–21] Subsequently, we fused the ABD nucleic acid sequence to the 3′ end of the AaLS gene with intervening linker residues (KDPNSGGGLVPRGSGGGSGGGTGGGSGGG) to provide flexibility and room for antibody accessibility. We previously reported that the C-termini of AaLS expose on the surface of protein cage nanoparticles and tolerate the insertion of oligopeptides.[19–21] However, this is the first time that a domain of this size (59 amino acids) has been introduced.

We overexpressed the ABD–AaLS and successfully purified them without significant loss of materials. We confirmed the fusion of the ABD and AaLS using DNA sequencing and mass spectrometric analysis. Compared with the mass of the dissociated AaLS monomer (16 652.5 Da), the dissociated subunit mass of ABD–AaLS (25 557.0 Da) showed an increase of 8904.5 Da, which exactly corresponds to the combined mass of the ABD and linker (calc. 8904.5 Da) (Figure 2.1A). In addition, the ABD fused to the C-terminus of AaLS did not significantly alter its original protein cage architecture. Transmission electron microscopic (TEM) images revealed a cage-like architecture with a diameter of approximately 15 nm, which is almost identical to that of AaLS (Figure 2.1B). Since the ABD is relatively small and lacking in electron density, it was not readily apparent in the TEM images. However, ABD–AaLS eluted much earlier than AaLS in size-exclusion chromatography (Figure 2.1C), consistent with a larger hydrodynamic diameter due to the addition of ABDs on the surface of AaLS. Dynamic light scattering analysis of ABD–AaLS confirmed a larger hydrodynamic diameter (18.3 nm) than that of AaLS (15.8 nm) (Figure 2.1D). These results indicate that ABD–AaLS forms an intact protein cage architecture uniformly displaying ABDs on the surface of AaLS. In order to investigate whether the displayed ABDs on the AaLS effectively capture various types of antibodies, we first monitored interactions between antibodies and ABD–AaLS in real time by quartz crystal microbalance (QCM). Deposition and release of molecules on the QCM sensor induce decreases and increases in resonance frequency ($-\Delta F$), respectively, and these changes are sensitive to the masses of the deposited or released molecules.[31] We previously showed that wild type and AaLS variants stably form a uniform monolayer on a gold QCM sensor without any surface modifications.[4,19,32-33] ABD–AaLS also strongly bound to the gold QCM sensor to form a uniform monolayer and remained bound even after washing with buffer (Figure 2.1E). The resonance frequency of the ABD–AaLS monolayer dramatically decreased upon the addition of rabbit IgG, whereas that of the AaLS monolayer was unchanged (Figure 2.1E). Even extensive buffer washing did not remove the initially bound rabbit IgGs (Figure 2.1E).

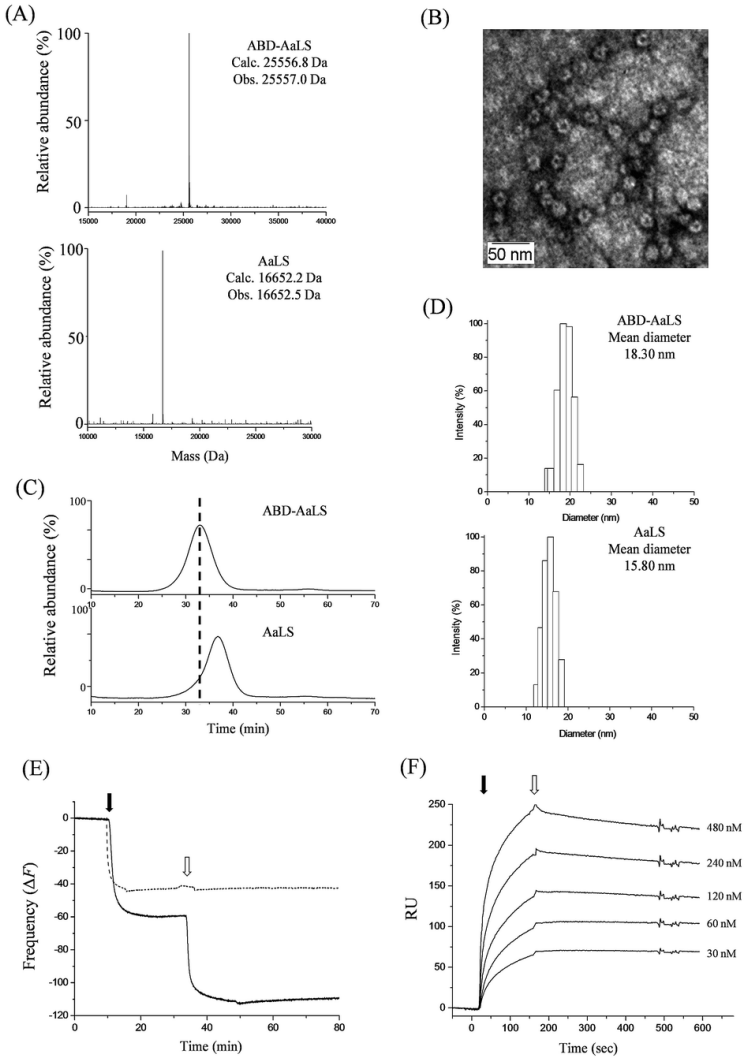

Figure 2.1 Characterization of ABD–AaLS. (A) Molecular mass measurements of the dissociated subunits of AaLS (calc. 16 652.2 Da; obs. 16 652.5 Da, bottom) and ABD–AaLS (calc. 25 556.8 Da; obs. 25 557.0 Da, top). (B) Transmission electron micrographic (TEM) image of 2% uranyl acetate stained ABD–AaLS. (C) Size-exclusion elution profiles of AaLS (bottom) and ABD–AaLS (top). (D) Dynamic light scattering measurements of AaLS (bottom) and ABD–AaLS (top). The mean diameters of AaLS and ABD–AaLS were 15.80 and 18.30 nm, respectively. (E) QCM resonance signal changes ($-\Delta F$) upon introduction of either AaLS (dashed line) or ABD–AaLS (solid line) onto the surface of standard gold sensors (closed arrow) and subsequent deposition of rabbit IgG on the monolayers of either AaLS (dashed line) or ABD–AaLS (solid line) (open arrow). (F) SPR analyses of ABD–AaLS binding to rabbit IgG immobilized SPR gold sensors. Various concentrations of ABD–AaLS (30, 60, 120, 240, and 480 nM) were loaded to the rabbit IgG immobilized SPR gold sensor at a flow rate of 5 μl min^{-1} for 2 min (closed arrow) and subsequently buffers were added (open arrow) and flow maintained for 8 min.

To further investigate the binding affinity between ABD–AaLS and rabbit IgGs, we performed surface plasmon resonance (SPR) analyses. In contrast to QCM studies, we first immobilized rabbit IgGs on the surface of an SPR CM5 sensor chip and then introduced ABD–AaLS at several different concentrations (Figure 2.1F). Each experiment was performed after regeneration of the free-IgG surface by base washing of ABD–AaLS bound to the IgG on the chip and subsequent equilibration with the appropriate binding buffer.[34] Gradual increases in SPR responses (RU) were observed upon introduction of ABD–AaLS at various concentrations (Figure 2.1F), whereas no apparent change was observed upon introduction of AaLS. Consistent with previous QCM results, apparent release of bound ABD–AaLS from the immobilized IgGs was not observed even after extensive buffer washing (Figure 2.1F). These data suggest that the polyvalent display of ABDs on the surface of AaLS protein cage nanoparticles may allow them to capture IgGs cooperatively while tightly maintaining antibody/ABD–AaLS (Ab/ABD–AaLS) complexes.

To investigate whether Ab/ABD–AaLS complexes can selectively bind their target cells guided by bound antibodies, we prepared target cell lines and selected corresponding monoclonal antibodies that recognize these cells. First, we prepared the SKBR3 breast cancer cell line and chose an anti-HER2 antibody as a model rabbit IgG, since HER2 is known to be overexpressed on the surface of SKBR3 cells and has been extensively utilized as a ligand for targeted delivery and therapy.[35,36] We first prepared Alexa Fluor 647-labeled anti-HER2 monoclonal antibodies (Alexa-HER2-Ab) and fluorescein-labeled ABD–AaLS (fABD–AaLS). Mass spectrometric analysis revealed that all the subunits were labeled with one fluorescein (60 fluorescein molecules per ABD–AaLS nanoparticle) (Figure 2.2A). Fluorescein conjugation did not significantly alter their cage architecture (Figure 2.2B and C).

Subsequently, we simply mixed Alexa-HER2-Ab and fABD–AaLS to form Alexa-HER2-Ab/fABD–AaLS complexes. These complexes were incubated with SKBR3 cells and visualized and analyzed by fluorescence microscopy and flow cytometry. fABD–AaLS and Alexa-HER2-Ab alone were used as negative and positive controls, respectively. While Alexa-HER2-Ab/fABD–AaLS complexes and Alexa-HER2-Ab bound to SKBR3 cells (Figure 2.3A and B), fABD–AaLS alone did not (Figure 2.3D). Fluorescence images of Alexa-HER2-Ab (Figure 2.3A, red, middle panel) and fABD–AaLS (Figure 2.3A, green, left panel) indicated their colocalization, which was confirmed in merged images (Figure 2.3A, right panel). Furthermore, when we treated SKBR3 cells with a complex of unlabeled HER2-Ab and fABD–AaLS, the cells were well visualized with HER2-Ab/fABD–AaLS complexes without fluorescent labeling of antibodies (Figure 2.3C). Flow cytometry measurements of Alexa-HER2-Ab, Alexa-HER2-Ab/fABD–AaLS complexes, and HER2-Ab/fABD–AaLS complexes revealed virtually identical levels of cell binding, quantitatively confirming their cell-specific binding (Figure 2.3E). These data demonstrate that anti-HER2 antibodies on the surface of fABD–AaLS allow these complexes to recognize HER2 expressed on the surface of SKBR3 cells and selectively bind to them. These data also imply that ABD–AaLS serves as a nanoplatform that not only displays targeting antibodies on the surface in an orientation-controlled manner but also acquires fluorescent probes effectively, and that they can be used as target-specific cell imaging

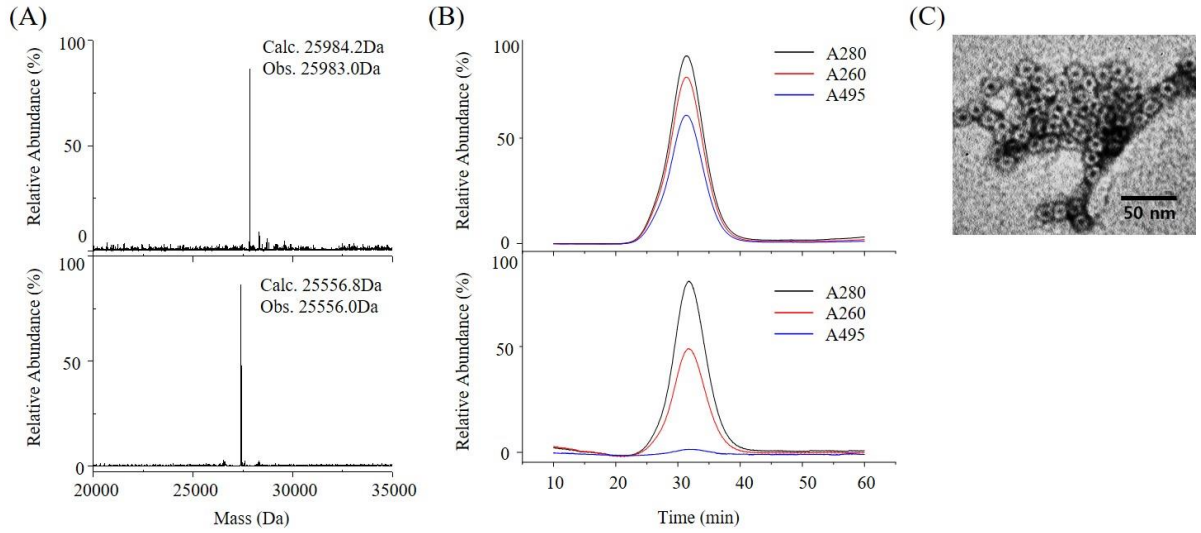

Figure 2.2 Characterization of fluorescent dye (fluorescein) labeled ABD-AaLS (fABD-AaLS). (A) Molecular mass measurements of the dissociated subunits of ABD-AaLS (calc. 25556.8 Da; obs. 25557.0 Da, bottom) and fABD-AaLS (calc. 25984.2 Da; obs. 25983.0 Da, top). Molecular mass increase (427.0 Da) upon labeling agreed excellent with molecular mass of fluorescein-5-maleimide (427.4 Da) (B) Size exclusion elution profiles of ABD-AaLS (bottom) and fABD-AaLS (top). fABD-AaLS eluted same time as that of untreated ABD-AaLS. Significant absorption increase at 495 nm is due to the attached fluoresceins. (C) Transmission electron micrographic (TEM) image of 2% uranyl acetate stained fABD-AaLS. fABD-AaLS maintained its cage architecture even after chemical conjugation of fluorescein.

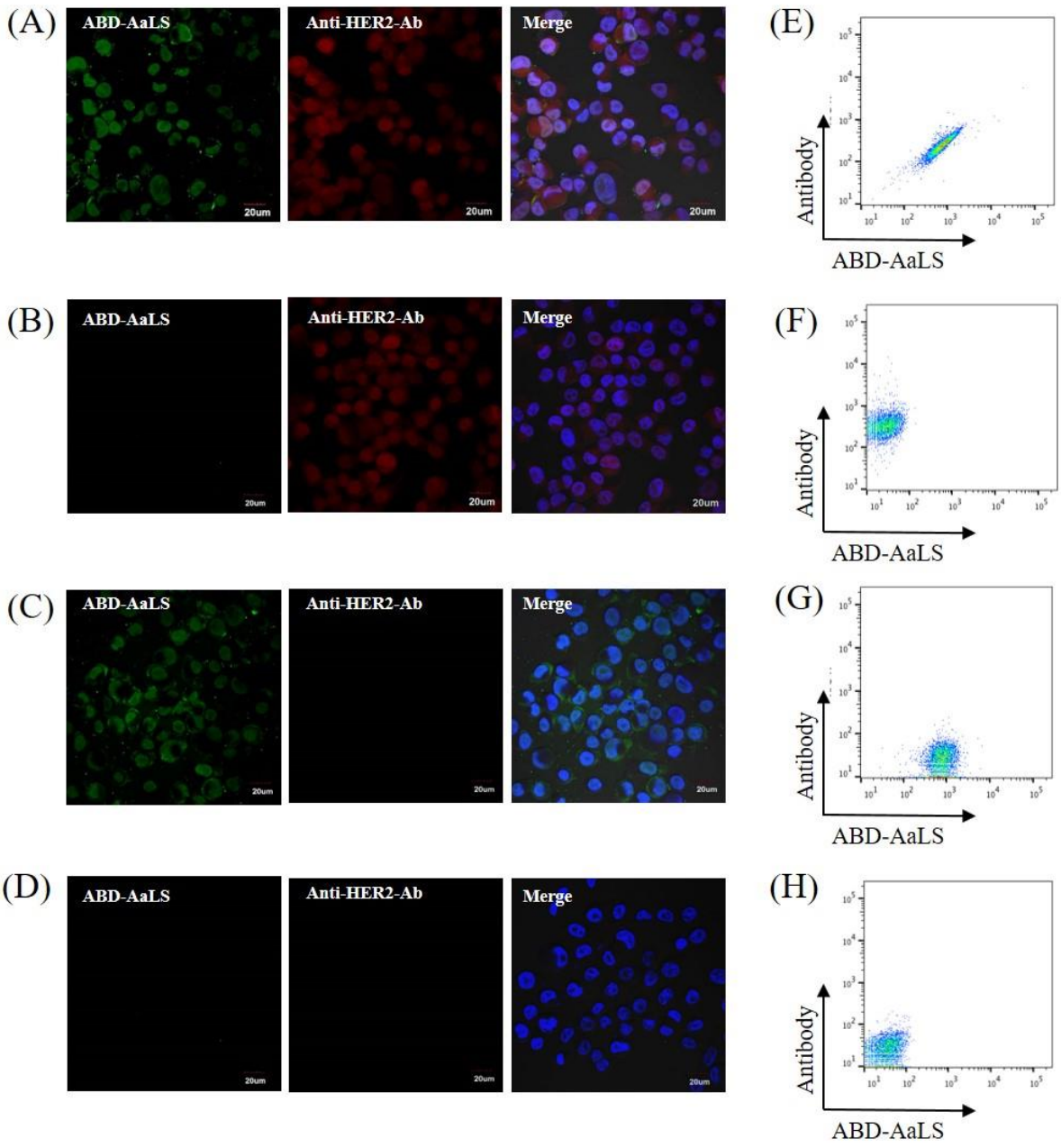

Figure 2.3 Florescence microscopic images (A–D) and flow cytometry measurements (E–H) of SKBR3 breast cancer cells treated with Alexa-HER2-Ab/fABD–AaLS complexes (A and E), Alexa-HER2-Ab only (B and F), HER2-Ab/fABD–AaLS complexes (C and G), and fABD–AaLS only (D and H). Rabbit anti-HER2 IgG and ABD–AaLS were labeled with Alexa Fluor 647 (Alexa-HER2-Ab, red) and fluorescein (fABD–AaLS, green), respectively, and nuclei were visualized with DAPI as blue. Fluorescein (left rows), Alexa Fluor 647 (middle rows), and merged with DAPI staining (right rows) are shown.

probes.

To examine whether ABD–AaLS can serve as a universal antibody-binding nanoplatform for target-selective cell imaging by displaying various types of targeting antibodies (IgGs) on the surface in an orientation-controlled manner, we adapted two other types of antibodies derived from rat and mouse individually. The ability of ABD–AaLS to bind to rat and mouse IgGs was validated by QCM and SPR analyses. QCM and SPR studies were performed under the same conditions as those for rabbit IgG, and the patterns of rat and mouse IgGs binding to the ABD–AaLS monolayer on the QCM sensor were virtually identical to those of rabbit IgG (Figure 2.4A and B). For SPR experiments, rat or mouse IgGs were immobilized on the surface of an SPR CM-5 sensor chip instead of rabbit IgG, followed by application of ABD–AaLS at a series of concentrations. The patterns of SPR responses were also similar to those of rabbit IgG (Figure 2.4C-F), suggesting that rat and mouse IgGs also bind strongly to ABD–AaLS but not to AaLS as rabbit IgG does.

To confirm specific binding between the non-covalent complexes consisting of ABD–AaLS and rat or mouse IgGs to the target cells, we chose anti-CD44 monoclonal antibody and anti-integrin $\alpha\beta\gamma_3$ monoclonal antibody as rat- and mouse-derived IgGs, respectively. We performed fluorescence cell imaging and flow cytometry under the same conditions as those for Alexa-HER2-Ab/fABD–AaLS. We prepared Alexa Fluor 647-labeled anti-CD44 Ab (Alexa-CD44-Ab) and anti-integrin $\alpha\beta\gamma_3$ Ab (Alexa-integrin-Ab), unlabeled anti-CD44 Ab (CD44-Ab) and anti-integrin $\alpha\beta\gamma_3$ Ab (integrin-Ab), and fluorescein-labeled ABD–AaLS (fABD–AaLS), and we subsequently mixed each Ab and fABD–AaLS to form Ab/fABD–AaLS complexes with various combinations as described above. The resulting Alexa-CD44-Ab/fABD–AaLS and CD44-Ab/fABD–AaLS or Alexa-integrin-Ab/fABD–AaLS and integrin-Ab/fABD–AaLS complexes were incubated with SCC-7 cells, which overexpress the cell-surface glycoprotein CD44 that is involved in cell–cell interactions and cell adhesion and migration,[37,38] or KB cells, which overexpress integrin $\alpha\gamma\beta_3$ on their surface.[39] The cells were then examined by fluorescence microscopy and flow cytometry (Figure 2.5 and Figure 2.6). Similarly to rabbit IgG, Alexa-CD44-Ab/fABD–AaLS and Alexa-integrin-Ab/fABD–AaLS complexes selectively bound to SCC-7 cells and KB cells, respectively (Figure 2.5A,E and Figure 2.6), and the fluorescence signals of fABD–AaLS (Figure 2.5A, green, left panel) and Alexa-CD44-Ab (Figure 2.5A, red, right panel) overlapped to each other (Figure 2.5A, right panel). Alexa-CD44-Ab and CD44-Ab/fABD–AaLS complexes also tightly bound to SCC-7 cells (Figure 2.5B,C and E). ABD–AaLS was alternatively labeled with Alexa Fluor 647 and subsequently complexed with unlabeled CD44-Ab. These complexes also tightly bound to SCC-7 cells (Figure 2.7), suggesting that ABD–AaLS is amenable to chemical modifications with various types of fluorophores.

To examine the efficacy of antibody-guided targeted drug delivery with ABD–AaLS, the 6-maleimidocaproyl hydrazone prodrug of doxorubicin (AlDox)[40] was chemically conjugated to ABD–AaLS (ABD–AaLS–AlDox) instead of fluorophores as described previously.[20,25] Subsequently, targeting antibodies were non-covalently complexed with ABD–AaLS–AlDox (Ab/ABD–AaLS–AlDox) depending

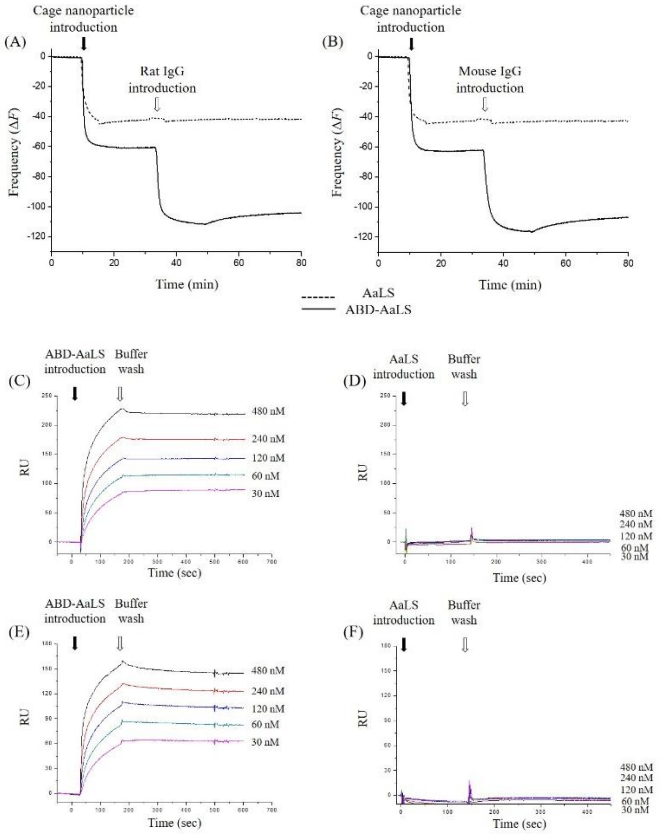

Figure 2.4 QCM resonance signal changes (-ΔF) upon introductions of either AaLS (dashed line) or ABD-AaLS (solid line) onto the surface of standard gold sensors (closed arrow) and subsequent deposition of rat (A) or mouse (B) IgGs on the monolayers of either AaLS (dashed line) or ABD-AaLS (solid line) (open arrow). SPR analyses of ABD-AaLS or AaLS binding to rat (C and D) or mouse (E and F) IgG immobilized SPR gold sensors. Various amounts of ABD-AaLS (C and E) or AaLS (D and F) (30, 60, 120, 240, and 480 nM) were loaded to the rat or mouse IgG immobilized SPR gold sensor at a flow rate of 5 μl/min for 2 min (closed arrow) and subsequently buffers were added (open arrow) and kept flow for 8 min.

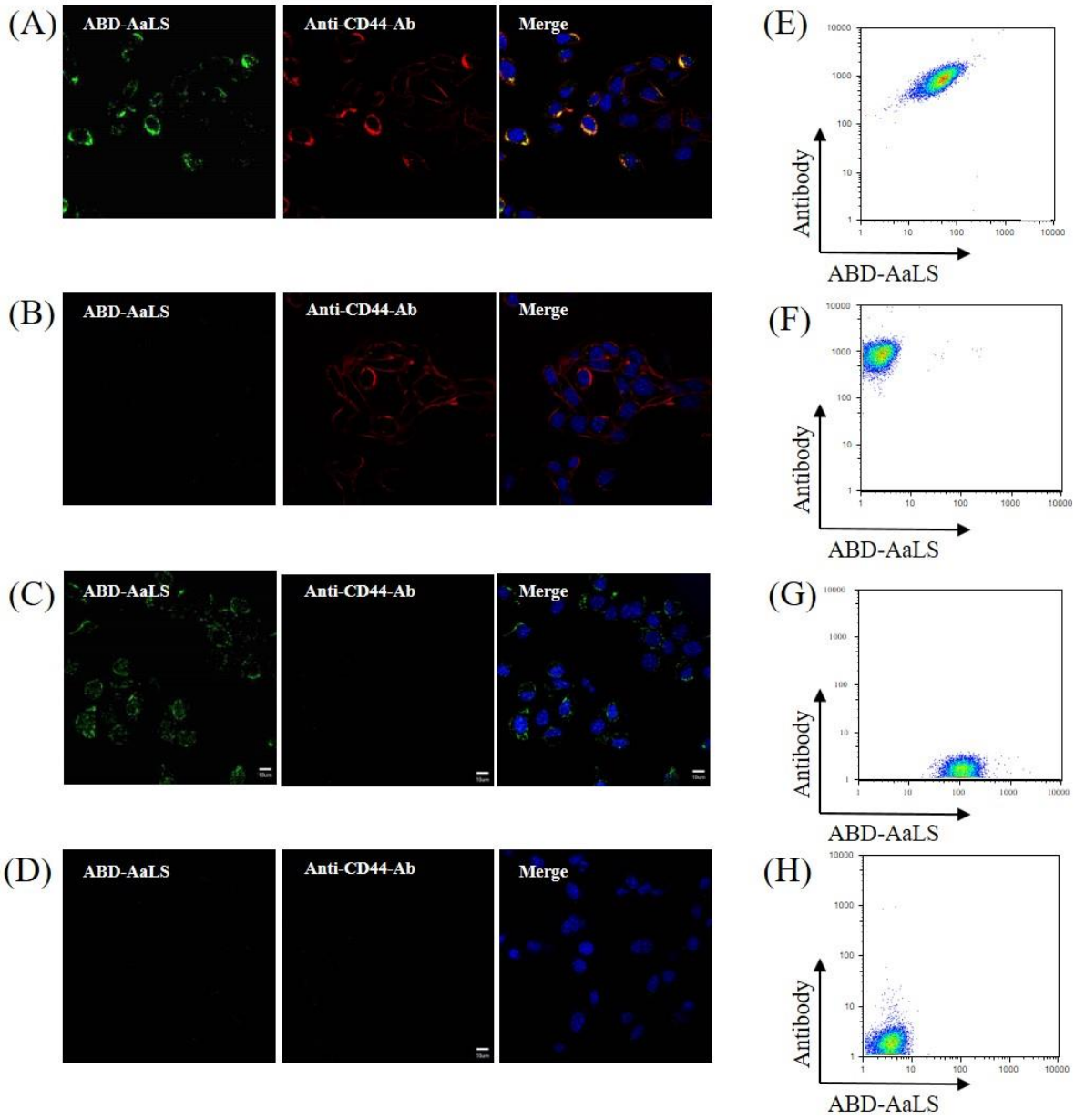

Figure 2.5 Florescence microscopic images (A–D) and flow cytometry measurements (E–H) of SCC-7 cells treated with Alexa-CD44-Ab/fABD–AaLS complexes (A and E), Alexa-CD44-Ab only (B and F), CD44-Ab/fABD–AaLS complexes (C and G), and fABD–AaLS only (D and H). Rat anti-CD44 IgG and ABD–AaLS were labeled with Alexa Fluor 647 (Alexa-CD44-Ab, red) and fluorescein (fABD–AaLS, green), respectively, and nuclei were visualized with DAPI as blue. Fluorescein (left rows), Alexa Fluor 647 (middle rows), and merged with DAPI staining (right rows) are shown.

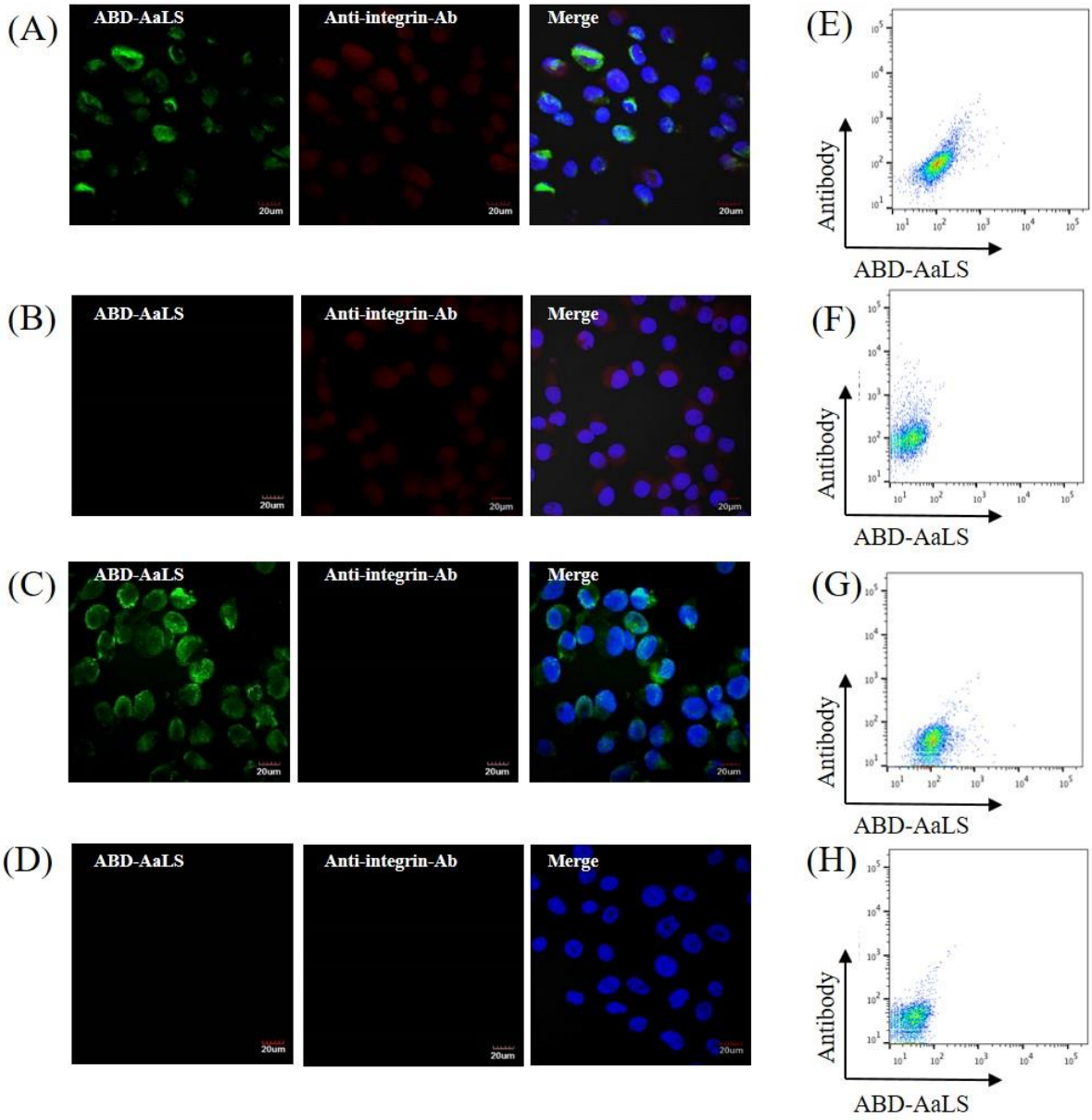

Figure 2.6 Florescence microscopic images (A-D) and flow cytometry measurements (E-H) of KB cells treated with Alexa-integrin-Ab/fABD-AaLS complexes (A and E), Alexa-integrin-Ab only (B and F), integrin-Ab/fABD-AaLS complexes (C and G) and fABD-AaLS only (D and H), respectively. Mouse anti-integrin IgG and ABD-AaLS were labeled with Alexa-647 (AlexaCD44-Ab, red) and fluorescein (fABD-AaLS, green), respectively, and nuclei were visualized with DAPI as blue. Fluorescein (left rows), Alexa-647 (middle rows), and merged with DAPI staining (right rows) were presented.

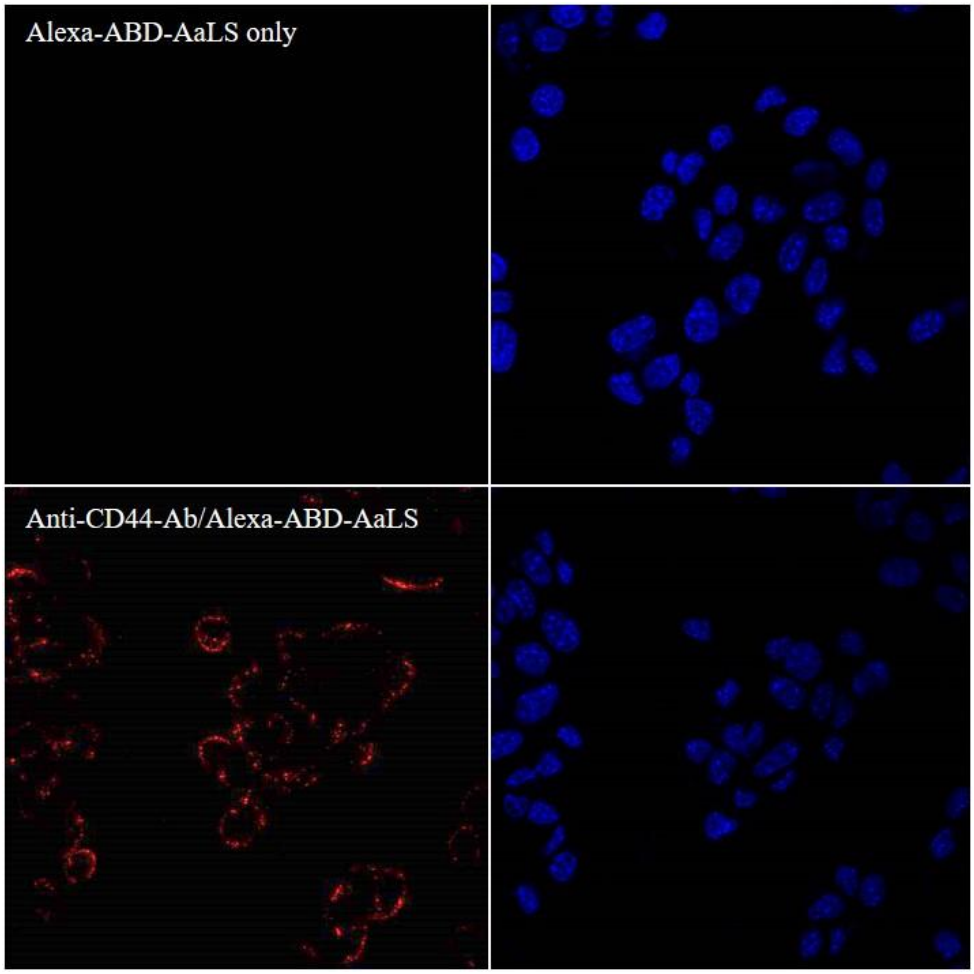

Figure 2.7 Florescent microscopic images of SCC-7 cells treated with Alexa-ABD-AaLS only (top two panels) and CD44-Ab/Alexa-ABD-AaLS complexes (bottom two panels), respectively. ABD-AaLS were labeled with Alexa-647 (Alexa-ABD-AaLS, red) and nuclei were visualized with DAPI as blue, whereas rat anti-CD44 IgG was not labeled with any dyes at all. Alexa-647 (left rows) and DAPI staining (right rows) were presented.

.

on target cells and 3-(4,5-dimethylthiazol-2-yl)-2,5-diphenyltetrazolium bromide (MTT) cell viability assays were performed. Hydrazine linkage is known to be quite stable at neutral pH and to become quickly cleaved under an acidic condition (pH 4.5–5.5).[40] We previously showed that 48 AlDox molecules are conjugated to one AaLS (60 subunits) and approximately 65% of them are released within 15 h.[20]

The SKBR3, SCC-7 and KB cells were treated with the complexes of anti-HER2-Ab, anti-CD44-Ab, or anti-integrin-Ab and ABD–AaLS–AlDox, respectively, for 1 h. The free prodrug, AlDox, and ABD–AaLS only were also treated in parallel to serve as positive and negative controls. One hour later, cells were washed with fresh media to remove unbound complexes and free AlDox, further cultured for 48 h, and their viability was measured to investigate the cytotoxicity of delivered drugs. The cytotoxic effects of delivered AlDox on antibody-corresponding target cells significantly increased in a dose-dependent manner and were higher than even those of free AlDox, whereas ABD–AaLS without AlDox had no significant effect on cell viability (Figure 2.8). The enhanced cytotoxicity of antibody-mediated ABD–AaLS–AlDox may be due to receptor-mediated endocytosis of whole complexes upon specific binding, which transports increased amounts of AlDox into the target cells, and subsequent low pH-induced release of Dox into the cells.

Taken together, these results indicate that ABD–AaLS can serve as a universal IgG-binding nanoplatform for efficiently displaying IgGs derived from a variety of species, such as rabbit, rat, and mouse, on demand by simple molecular recognition, and those complexes can be used as not only effective optical probes for target-specific cell imaging but also drug-carriers for target-specific treatment.

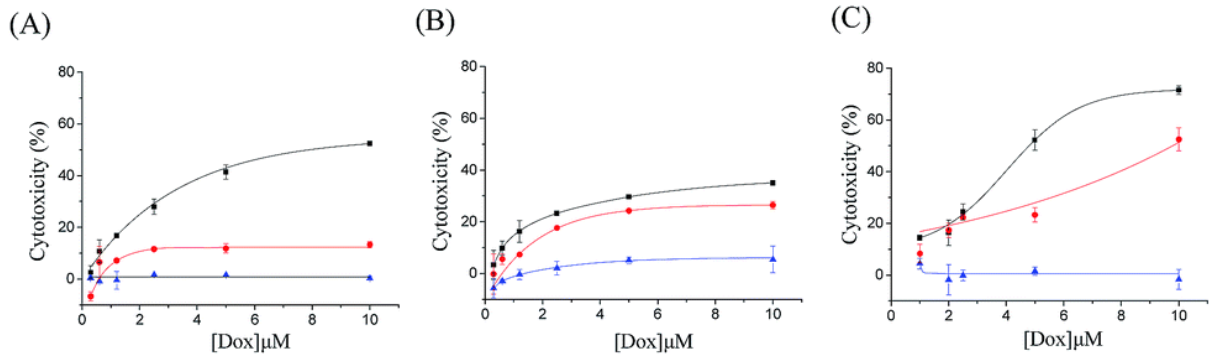

Figure 2.8 MTT cell viability assay. (A) Dose-dependent cytotoxicity profiles of anti-HER2-Ab/ABD–AaLS–AlDox (black, squares), free AlDox (red, circles), and ABD–AaLS only (blue, triangles) toward SKBR3 cells. (B) Dose-dependent cytotoxicity profiles of anti-CD44-Ab/ABD–AaLS–AlDox (black, squares), free AlDox (red, circles), and ABD–AaLS only (blue, triangles) toward SCC-7 cells. (C) Dose-dependent cytotoxicity profiles of anti-integrin-Ab/ABD–AaLS–AlDox (black, squares), free AlDox (red, circles), and ABD–AaLS only (blue, triangles) toward KB cells.

2.4 Conclusion

In this study, we constructed a polyvalent antibody-binding nanoplatform, ABD–AaLS, and demonstrated that ABD–AaLS effectively captures various types of antibodies derived from diverse species on demand. We also successfully demonstrated that targeting antibody/ABD–AaLS complexes selectively recognize and bind to their target cells *in vitro*, guided by antibodies displayed on the surface of ABD–AaLS.

Antibodies offer an almost unlimited range of specific targeting moieties, making them attractive targeting ligands for *in vitro* and/or *in vivo* diagnostics.[1,2,5,41] Depending on the target cells, appropriate antibodies can be selected and simply mixed with ABD–AaLS, which can be independently pre-modified depending on the purposes, to form diagnostic probe complexes. Utilizing ABD–AaLS as a universal antibody-binding nanoplatform, we can overcome the drawbacks associated with chemical conjugation of antibodies through non-covalent complexation as well as introduce additional functionalities to ABD–AaLS without altering antibody activity. Since ABD–AaLS has an additional internal cavity and exterior sites for encapsulation and attachment of cargo molecules such as drugs and diagnostic probes, ABD–AaLS may provide new opportunities to develop versatile target-dependent theranostic delivery systems.

2.5 References

1. Allen, T. M., Ligand-targeted therapeutics in anticancer therapy. *Nat Rev Cancer* **2002,** *2* (10), 750-763.

2. Carter, P., Improving the efficacy of antibody-based cancer therapies. *Nat Rev Cancer* **2001,** *1* (2), 118-129.

3. Hainfeld, J. F., Uranium-Loaded Apoferritin with Antibodies Attached - Molecular Design for Uranium Neutron-Capture Therapy. *P Natl Acad Sci USA* **1992,** *89* (22), 11064-11068.

4. Kang, H. J.; Kang, Y. J.; Lee, Y. M.; Shin, H. H.; Chung, S. J.; Kang, S., Developing an antibody-binding protein cage as a molecular recognition drug modular nanoplatform. *Biomaterials* **2012,** *33* (21), 5423-5430.

5. von Mehren, M.; Adams, G. P.; Weiner, L. M., Monoclonal antibody therapy for cancer. *Annu Rev Med* **2003,** *54*, 343-69.

6. Erathodiyil, N.; Ying, J. Y., Functionalization of inorganic nanoparticles for bioimaging applications. *Acc Chem Res* **2011,** *44* (10), 925-35.

7. Farokhzad, O. C.; Langer, R., Impact of nanotechnology on drug delivery. *ACS Nano* **2009,** *3* (1), 16-20.

8. Gillies, E. R.; Frechet, J. M. J., Dendrimers and dendritic polymers in drug delivery. *Drug Discov Today* **2005,** *10* (1), 35-43.

9. Sutton, D.; Nasongkla, N.; Blanco, E.; Gao, J. M., Functionalized micellar systems for cancer targeted drug delivery. *Pharm Res-Dordr* **2007,** *24* (6), 1029-1046.

10. Torchilin, V. P., Recent advances with liposomes as pharmaceutical carriers. *Nat Rev Drug Discov* **2005,** *4* (2), 145-60.

11. Danczyk, R.; Krieder, B.; North, A.; Webster, T.; HogenEsch, H.; Rundell, A., Comparison of antibody functionality using different immobilization methods. *Biotechnol Bioeng* **2003,** *84* (2), 215-23.

12. Zhang, X.; Meining, W.; Fischer, M.; Bacher, A.; Ladenstein, R., X-ray structure analysis and crystallographic refinement of lumazine synthase from the hyperthermophile Aquifex aeolicus at 1.6 A resolution: determinants of thermostability revealed from structural comparisons. *J Mol Biol* **2001,** *306* (5), 1099-114.

13. Zhang, X.; Meining, W.; Cushman, M.; Haase, I.; Fischer, M.; Bacher, A.; Ladenstein, R., A structure-based model of the reaction catalyzed by lumazine synthase from Aquifex aeolicus. *J Mol Biol* **2003,** *328* (1), 167-82.

14. Seebeck, F. P.; Woycechowsky, K. J.; Zhuang, W.; Rabe, J. P.; Hilvert, D., A simple tagging system for protein encapsulation. *J Am Chem Soc* **2006,** *128* (14), 4516-7.

15. Worsdorfer, B.; Pianowski, Z.; Hilvert, D., Efficient in vitro encapsulation of protein cargo by an engineered protein container. *J Am Chem Soc* **2012,** *134* (2), 909-11.

16. Worsdorfer, B.; Woycechowsky, K. J.; Hilvert, D., Directed evolution of a protein container. *Science* **2011,** *331* (6017), 589-92.

17. Beck, T.; Tetter, S.; Kunzle, M.; Hilvert, D., Construction of Matryoshka-type structures from supercharged protein nanocages. *Angew Chem Int Ed Engl* **2015,** *54* (3), 937-40.

18. Shenton, W.; Mann, S.; Colfen, H.; Bacher, A.; Fischer, M., Synthesis of Nanophase Iron Oxide in Lumazine Synthase Capsids. *Angew Chem Int Ed Engl* **2001,** *40* (2), 442-445.

19. Moon, H.; Kim, W. G.; Lim, S.; Kang, Y. J.; Shin, H. H.; Ko, H.; Hong, S. Y.; Kang, S., Fabrication of uniform layer-by-layer assemblies with complementary protein cage nanobuilding blocks via simple His-tag/metal recognition. *J Mater Chem B* **2013,** *1* (35), 4504-4510.

20. Min, J.; Kim, S.; Lee, J.; Kang, S., Lumazine synthase protein cage nanoparticles as modular delivery platforms for targeted drug delivery. *RSC Advances* **2014,** *4* (89), 48596-48600.

21. Ra, J. S.; Shin, H. H.; Kang, S.; Do, Y., Lumazine synthase protein cage nanoparticles as antigen delivery nanoplatforms for dendritic cell-based vaccine development. *Clin Exp Vaccine Res* **2014,** *3* (2), 227-34.

22. Kang, Y. J.; Yang, H. J.; Jeon, S.; Kang, Y. S.; Do, Y.; Hong, S. Y.; Kang, S., Polyvalent Display of Monosaccharides on Ferritin Protein Cage Nanoparticles for the Recognition and Binding of Cell-Surface Lectins. *Macromolecular bioscience* **2014,** *14* (5), 619-625.

23. Kwon, C.; Kang, Y. J.; Jeon, S.; Jung, S.; Hong, S. Y.; Kang, S., Development of protein-cage-based delivery nanoplatforms by polyvalently displaying beta-cyclodextrins on the surface of ferritins through copper(I)-catalyzed azide/alkyne cycloaddition. *Macromol Biosci* **2012,** *12* (11), 1452-8.

24. Min, J.; Moon, H.; Yang, H. J.; Shin, H. H.; Hong, S. Y.; Kang, S., Development of P22 viral capsid nanocomposites as anti-cancer drug, bortezomib (BTZ), delivery nanoplatforms. *Macromol Biosci* **2014,** *14* (4), 557-64.

25. Moon, H.; Lee, J.; Min, J.; Kang, S., Developing genetically engineered encapsulin protein cage nanoparticles as a targeted delivery nanoplatform. *Biomacromolecules* **2014,** *15* (10), 3794-801.

26. Bonroy, K.; Frederix, F.; Reekmans, G.; Dewolf, E.; De Palma, R.; Borghs, G.; Declerck, P.; Goddeeris, B., Comparison of random and oriented immobilisation of antibody fragments on mixed self-assembled monolayers. *J Immunol Methods* **2006,** *312* (1-2), 167-81.

27. Braisted, A. C.; Wells, J. A., Minimizing a binding domain from protein A. *Proc Natl Acad Sci U S A* **1996,** *93* (12), 5688-92.

28. Deisenhofer, J., Crystallographic refinement and atomic models of a human Fc fragment and its complex with fragment B of protein A from Staphylococcus aureus at 2.9- and 2.8-A resolution. *Biochemistry* **1981,** *20* (9), 2361-70.

29. Lee, J.; Song, E. K.; Bae, Y.; Min, J.; Rhee, H. W.; Park, T. J.; Kim, M.; Kang, S., An enhanced ascorbate peroxidase 2/antibody-binding domain fusion protein (APEX2-ABD) as a recombinant target-specific signal amplifier. *Chem Commun (Camb)* **2015,** *51* (54), 10945-8.

30. Hwang, M. P.; Lee, J. W.; Lee, K. E.; Lee, K. H., Think modular: a simple apoferritin-based platform for the multifaceted detection of pancreatic cancer. *ACS Nano* **2013,** *7* (9), 8167-74.

31. Hook, F.; Rodahl, M.; Brzezinski, P.; Kasemo, B., Energy dissipation kinetics for protein and antibody-antigen adsorption under shear oscillation on a quartz crystal microbalance. *Langmuir* **1998,** *14* (4), 729-734.

32. Kang, S.; Suci, P. A.; Broomell, C. C.; Iwahori, K.; Kobayashi, M.; Yamashita, I.; Young, M.; Douglas, T., Janus-like Protein Cages. Spatially Controlled Dual-Functional Surface Modifications of Protein Cages. *Nano Lett* **2009,** *9* (6), 2360-2366.

33. Kang, Y. J.; Uchida, M.; Shin, H. H.; Douglas, T.; Kang, S., Biomimetic FePt nanoparticle synthesis within Pyrococcus furiosus ferritins and their layer-by-layer formation. *Soft Matter* **2011,** *7* (23), 11078-11081.

34. Jung, Y. W.; Kang, H. J.; Lee, J. M.; Jung, S. O.; Yun, W. S.; Chung, S. J.; Chung, B. H., Controlled antibody immobilization onto immunoanalytical platforms by synthetic peptide. *Anal Biochem* **2008,** *374* (1), 99-105.

35. Hellstrom, I.; Goodman, G.; Pullman, J.; Yang, Y.; Hellstrom, K. E., Overexpression of HER-2 in ovarian carcinomas. *Cancer Res* **2001,** *61* (6), 2420-2423.

36. Rhodes, A., Developing a cell line standard for HER2/neu. *Cancer Biomark* **2005,** *1* (4-5), 229-32.

37. Choi, K. Y.; Chung, H.; Min, K. H.; Yoon, H. Y.; Kim, K.; Park, J. H.; Kwon, I. C.; Jeong, S. Y., Self-assembled hyaluronic acid nanoparticles for active tumor targeting. *Biomaterials* **2010,** *31* (1), 106-14.

38. Koo, O. M.; Rubinstein, I.; Onyuksel, H., Role of nanotechnology in targeted drug delivery and imaging: a concise review. *Nanomedicine* **2005,** *1* (3), 193-212.

39. Arap, W.; Pasqualini, R.; Ruoslahti, E., Cancer treatment by targeted drug delivery to tumor vasculature in a mouse model. *Science* **1998,** *279* (5349), 377-380.

40. Willner, D.; Trail, P. A.; Hofstead, S. J.; King, H. D.; Lasch, S. J.; Braslawsky, G. R.; Greenfield, R. S.; Kaneko, T.; Firestone, R. A., (6-Maleimidocaproyl)hydrazone of doxorubicin--a new derivative for the preparation of immunoconjugates of doxorubicin. *Bioconjug Chem* **1993,** *4* (6), 521-7.

41. Suci, P. A.; Kang, S.; Young, M.; Douglas, T., A Streptavidin-Protein Cage Janus Particle for Polarized Targeting and Modular Functionalization. *Journal of the American Chemical Society* **2009,** *131* (26), 9164-+.

Chapter 3. Development of target-tunable P22 VLP-based delivery nanoplatforms using bacterial superglue

3.1 Introduction

The targeted delivery of diagnostics and/or therapeutics is a powerful approach for early diagnosis and treatment of disease in the biomedical field. Protein cage nanoparticles have been widely used as targeted delivery vehicles for diagnostic and therapeutic applications [1-5], because they have well-defined, highly symmetrical structures of uniform size and shape, with a simple composition comprising multiple copies of one or two protein subunits, and a plasticity which enables them to be manipulated both genetically and chemically. The interior cavities and surfaces of protein cage nanoparticles are generally loaded with cargo molecules including drugs, fluorescent dyes, antigens, contrast agents, enzymes, and polymers, using self-assembly mediated encapsulations and/or chemical conjugations [6-13]. The exterior surface is frequently used to display targeting ligands [2]. Small targeting ligands, such as RGD and SP94 peptides or folic acids, have been displayed via direct genetic fusion or chemical conjugation on the exterior of protein cage nanoparticles [2, 14-15]. However, these approaches are only suitable for small peptides or chemicals, not for whole protein or domain ligands. Direct genetic fusion of whole proteins or domain ligands frequently results in disruption of the supramolecular architecture of protein cage nanoparticles, inducing aggregation and/or improper folding of the protein cage nanoparticles [16-17]. Thus, it is necessary to develop an easy method for displaying large proteins or domain ligands on the surface of protein cage nanoparticles.

In this study, we constructed target-tunable and cargo-loadable modular delivery nanoplatforms using P22 virus-like particles (VLPs); displayed two different targeting ligands on their surface; tailored to their target cells using a bacterial superglue, the SpyTag/SpyCatcher (ST/SC) post-translational ligation system; and loaded prodrugs on either interior or exterior surfaces on demand (Scheme 3.1).

Salmonella typhimurium bacteriophage P22 VLP self-assembles from 420 copies of the coat protein, with the aid of approximately 300 scaffolding proteins. It forms *T*=7 icosahedral hollow nanoparticles with an outer diameter of 56 nm [18]. P22 VLPs have been widely utilized as nanoplatforms for delivering cargo molecules in a target-specific manner [15, 19] by encapsulating functional proteins within their interior cavity [12], because of their large, robust, and versatile structure, which can be created by easy heterologous expression. Recently, a sortase tag, LPETG, was genetically introduced into the C-terminus of the P22 capsid and an N-terminally polyglycine-tagged GFP or head domain of the influenza hemagglutinin protein (HAhead) were post-translationally attached using sortase-

mediated ligation [20]. We used the ST/SC post-translational ligation system to produce P22 VLPs displaying relatively large targeting ligands on their surfaces, without altering the protein cage nanoparticle architecture. SpyTag (ST) and SpyCatcher (SC) are split proteins derived from the *Streptococcus pyogenes* fibronectin-binding protein FbaB. The SpyCatcher protein recognizes 13 amino acids (AHIVMVDAYKPTK) of SpyTag, and they form a covalent isopeptide bond [21]. This reaction is rapid and selective and occurs under a range of pH, buffer, and temperature conditions upon mixing, without the need for additional chemical compounds or enzymes. Previously, we constructed a series of multifunctional protein conjugates by combining either various affibody molecules [22-24] and fluorescent proteins or enzymes and clustering ligands post-translationally in a mix-and-match manner. We also demonstrated that those conjugates exhibited a range of different functions [22, 24-25]. The ST/SC protein ligation system has been applied for displaying various antigenic proteins and targeting ligands on virus-like particles and their effective immune response inductions and cell-specific gene delivery were successfully demonstrated[26-34].

In the research reported here, we developed target-tunable P22 VLP-based polyvalent delivery nanoplatforms, ligated two different targeting affibody molecules on demand, chemically conjugated pH-sensitive prodrugs, and evaluated them as drug delivery platforms to bind target receptors and selectively kill target cells *in vitro*.

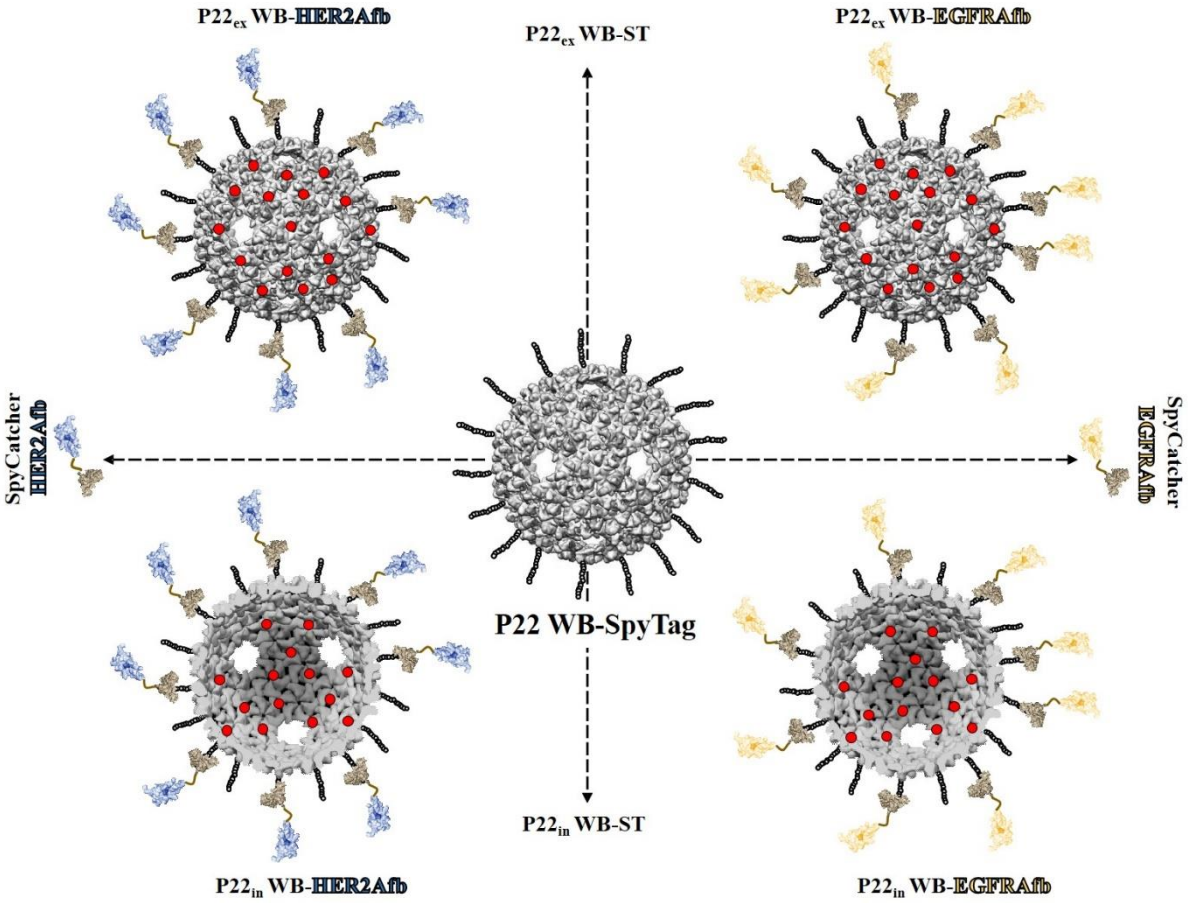

Scheme 3.1 Schematic representation of various configurations of target-tunable and cargo-loadable P22 VLP-based delivery nanoplatforms. Red dots on the interior (bottom) and exterior (top) surface of particles represent either prodrugs or fluorescent dyes. HER2Afb and EGFRAfb are represented as blue and yellow surface models, respectively. VLP, virus-like particles

3.2 Materials and Methods

Genetic modifications and purifications of P22 WB-ST and SC-Afb

SpyTag peptide (AHIVMVDAYKPTK) with extra amino acids (SGGGSGGG) were genetically added to C-terminus of P22 capsid protein by well-established polymerase chain reaction (PCR). Either lysine residue at position 118 or serine residues at position 113 of P22 capsid protein was genetically substituted with cysteine ($P22_{in}$ VLP-ST or $P22_{ex}$ VLP-ST). P22 VLP-ST ($P22_{in}$ VLP-ST and $P22_{ex}$ VLP-ST) genes were subcloned in pET30a vector, transformed to *E.coli* strain BL21(DE3), and overexpressed at 37 ℃ for 16 hrs in a shaking incubator. P22 VLP-ST were sedimented with 35% sucrose cushion and recovered by slow resuspension with buffer. Resuspended P22 VLP-ST were further heated at 75 ℃ for 15 min to obtain P22 WB-ST. P22 WB-ST were further purified by 10-35% sucrose gradient [18]. On the other hands, SpyCatcher protein was genetically fused to N-termini of epidermal growth factor receptor (EGFR) affibody molecules or human epidermal growth factor receptor2 (HER2) affibody molecules with extra amino acids (SGGGSGGG) by PCR. SC-Afb (SC-EGFRAfb and SC-HER2Afb) in pETDuet vector were transformed to *E.coli* strain BL21(DE3) and overexpressed at 30 ℃ for 16 hrs in shaking incubator. SC-Afb were purified by immobilized metal affinity chromatography (IMAC) [24]. Purified proteins were dialyzed against with phosphate-buffered saline (PBS, pH7.4).

Characterization of purified P22 WB-ST and P22 WB-ST/SC-Afb

Concentrations of P22 WB-ST and SC-Afb in PBS (pH 7.4) were determined by the BCA assay. P22 WB-ST were mixed with various amounts of SC-Afb and incubated for various times at room temperature to obtain the optimal reaction condition. Reactions were stopped at indicated times by adding SDS loading buffer and boiling at 110℃. Reaction products were analyzed with SDS-PAGE and optimal condition of input ratio of SC-Afb to P22 WB-ST subunit was determined as 0.4 and reaction was finished within 30 min. Hydrodynamic diameters of P22 WB-ST and P22 WB-ST/SC-Afb were measured with dynamic light scattering (DLS; Zetasizer, Malvern). Each sample was prepared at 1 mg/ml concentration and set in disposable rectangular polystyrene cuvette. The scattered light was detected by a 90° angle with the projected light at 25℃. P22 WB-ST and P22 WB-ST/SC-Afb were also negatively stained with 2% uranyl acetate and images were obtained with transmission electron microscope (TEM). P22-ST were stable in PBS at 4℃ for a month and SC-Afb were stable at −20℃ for 6 months.

Cell culture and fluorescent microscope imaging

MDA-MB-468 and MCF-10A cells were purchased from American Type Culture Collection (ATCC) and SK-BR3 and MCF-7 cells were purchased from Korean cell line bank (KCLB). MDA-MB-468 cells were cultured in Leibovitz's L-15 medium with 10% fetal bovine serum (FBS), 1% antibiotic-antimycotic, 25 mM HEPES and sodium bicarbonate. SK-BR-3 cells were cultured in DMEM medium with 10% FBS and 1% antibiotic-antimycotic. MCF-7 cells were cultured in RPMI-1640 with 10% FBS and 1% antibiotic-antimycotic. MCF-10A cells were cultured in DMEM/F12 with 5% horse serum, 1% penicillin/streptomycin, EGF, hydrocortisone, insulin, and 25 mM bicarbonate. All cells were grown in 5% CO_2 and 95% air at 37°C. 1×10^5 cells were grown on microscope cover glass in a 12-well plate for overnight to perform fluorescent microscopic imaging. The cells were fixed by 4% paraformaldehyde in PBS. Subsequently, blocking buffer (5% BSA, 5% FBS, and 0.5% Triton X-100 in PBS) were treated for 1 hr at room temperature with gentle shake to prevent the nonspecific binding of samples to the background. Ten micrometers of the samples were added to fixed cells and incubated for 1 hr at room temperature. Before sealing, the cells were washed by wash buffer (0.1% Triton X-100 in PBS) three times and the nuclei were stained by DAPI. Images of samples were acquired by Olympus Fluoview FV1000 fluorescent microscope (Olympus, UOBC).

Cytotoxic assay

The in vitro cytotoxicity of Aldoxorubicin (AlDox) conjugated samples was measured by the thiazolyl blue tetrazolium bromide (MTT; Sigma-Aldrich) assay. 1×10^4 cells were cultured in 96-well plates for overnight. Serially diluted samples from 20 μM to 1.2 μM were treated to cells under 5% CO_2 at 37°C for 1 hr. The cells were washed with fresh media two times and grown for additional 3 days. The cells were treated with 200 μl of media containing 0.5 mg/ml of MTT for 3 hrs, media were removed, and the cells were resuspended with dimethyl sulfoxide (DMSO) to dissolve formazan crystals formed in viable cells. Dissolved formazan was monitored by measuring absorbance at 595 nm with multi-scanner (Spectramax, Molecular devices).

3.3 Results and discussion

SpyTag was genetically fused to the C-terminus of the P22 viral capsid, which is known to be exposed to the exterior [35] to form P22 VLP-ST. One amino acid located on either the interior or exterior surface of P22 VLP was mutated with cysteine (S133C or K118C, respectively) to conjugate cargo molecules through thiol-maleimide conjugation [18, 36]. We used two affibody molecules which selectively bind to EGFR and HER2 (EGFRAfb and HER2Afb, respectively) [37-38] as targeting ligands, because breast cancer cells usually overexpress EGFR, HER2, or both on their surfaces and they are well-known tumor biomarkers for diagnosis and therapeutics [39]. SpyCatcher was genetically fused to the N-termini of EGFRAfb and HER2Afb with an extra linker to produce SC-EGFRAfb and SC-HER2Afb, respectively [22, 24]. P22 VLP-ST were overexpressed in *E. coli*, purified by sucrose gradient centrifugation, and heated at 75°C for 15 min to remove scaffold proteins and form a wiffle ball structure, denoted P22 WB-ST [40]. P22 WB-ST have genome- and scaffolding protein-free hollow architectures, with sufficient space for accommodating small chemotherapeutic agents and/or diagnostic probes within their cavity [36]. The twelve 10-nm pores of P22 WB-ST could be used as portals for the entry and exit of even larger molecular species [41] and the C-terminal end of capsid protein is surely exposed to the surface in the form of P22 WB [20, 35]. Formation of the wiffle ball structure was confirmed by removing scaffold proteins using SDS-PAGE and assessing the mobility shift on native agarose gels (Figure 3.1A and B). The hydrodynamic diameter, as determined by dynamic light scattering (DLS), was slightly increased (Figure 3.1C) when there was an intact cage architecture, as confirmed by transmission electron microscopy (TEM) (Figure 3.1D). Independently, SC-Afb (SC-EGFRAfb and SC-HER2Afb) were overexpressed in *E. coli* and purified with Ni-NTA-based immobilized metal affinity chromatography (Ni-NTA-agarose columns). Using purified SC-Afb and P22 WB-ST, we first investigated the number of affibody molecules which could be loaded on a P22 WB-ST without altering the protein cage nanoparticle architecture. We fixed the amount of P22 WB-ST and varied the input amounts of SC-Afb (Figure 3.2A and B). The degree of isopeptide formation between the P22 WB-ST subunits and SC-Afb increased as the input ratio of SC-Afb to P22 WB-ST subunits increased, up to 0.4, and reaction mixtures started to aggregate at ratios higher than 0.5. Although there is no atomic resolution structure of P22 VLP, we hypothesize that the C-termini of P22 WB-ST subunits may have clustered together as the amounts of attached SC-Afb increased and excess amounts of attached SC-Afb resulted in aggregation of P22 VLP conjugates similar to those observed in sortase-mediated conjugations [20]. Densitometric analyses indicated that approximately 150 copies of affibody molecules were attached to 1 P22 WB-ST with a 0.4 SC-Afb input ratio on average, a result which matches well with the number calculated: 144 copies of affibody molecules (0.4 x 360 subunit/P22 WB-ST) (Figure 3.3A). We therefore prepared P22 WB-ST/SC-Afb using this ratio, to maximize the number of targeting ligands per particle, while minimizing particle aggregation.

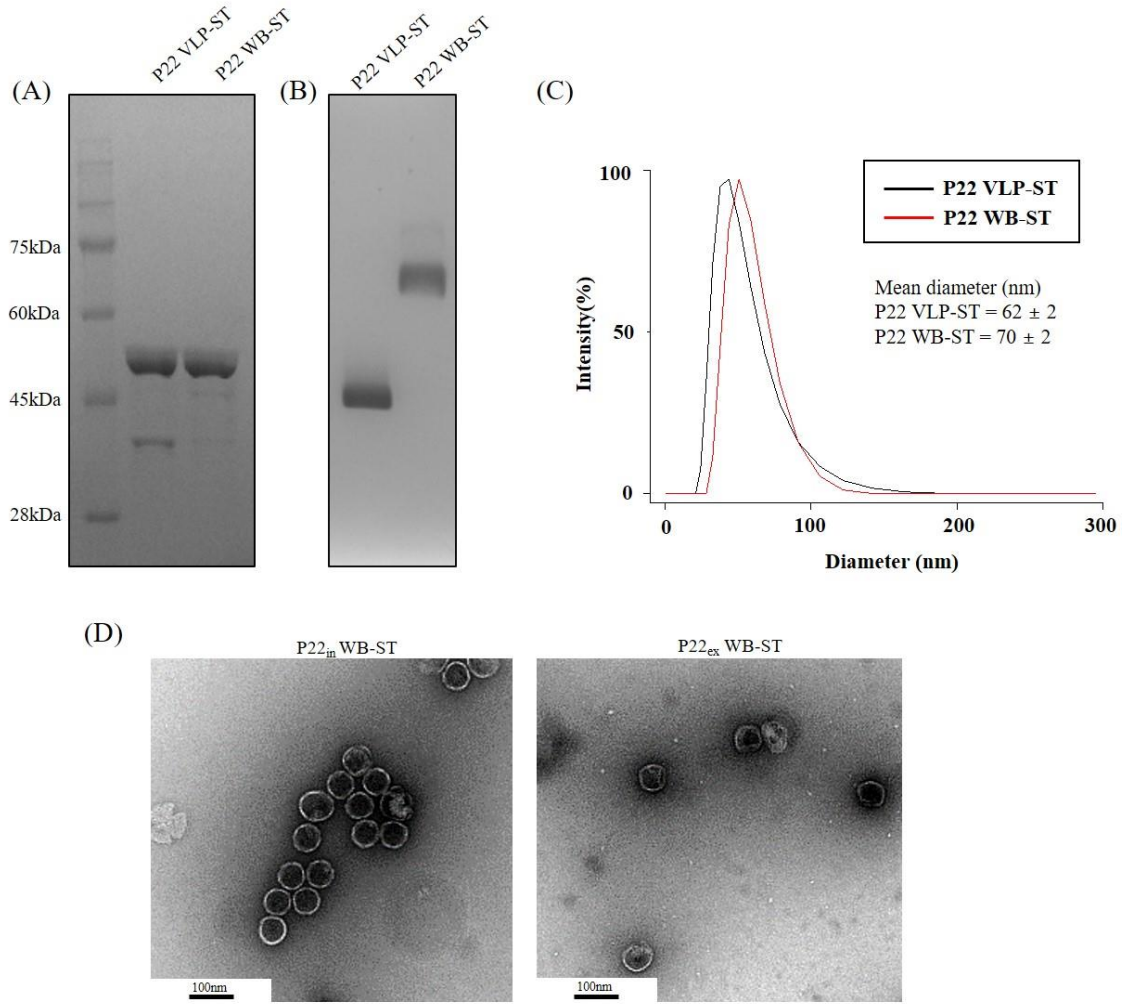

Figure 3.1 Characterization of wiffle ball form of P22 VLP-ST (P22 WB-ST). (a) SDS-PAGE analyses of P22 VLP-ST and P22 WB-ST. (b) Native agarose gel electrophoresis analyses of P22 VLP-ST and P22 WB-ST. (c) Dynamic light scattering (DLS) analyses of P22 VLP-ST and P22 WB-ST. (d) Transmission electron microscopy (TEM) images of P22in WB-ST and P22ex WB-ST.

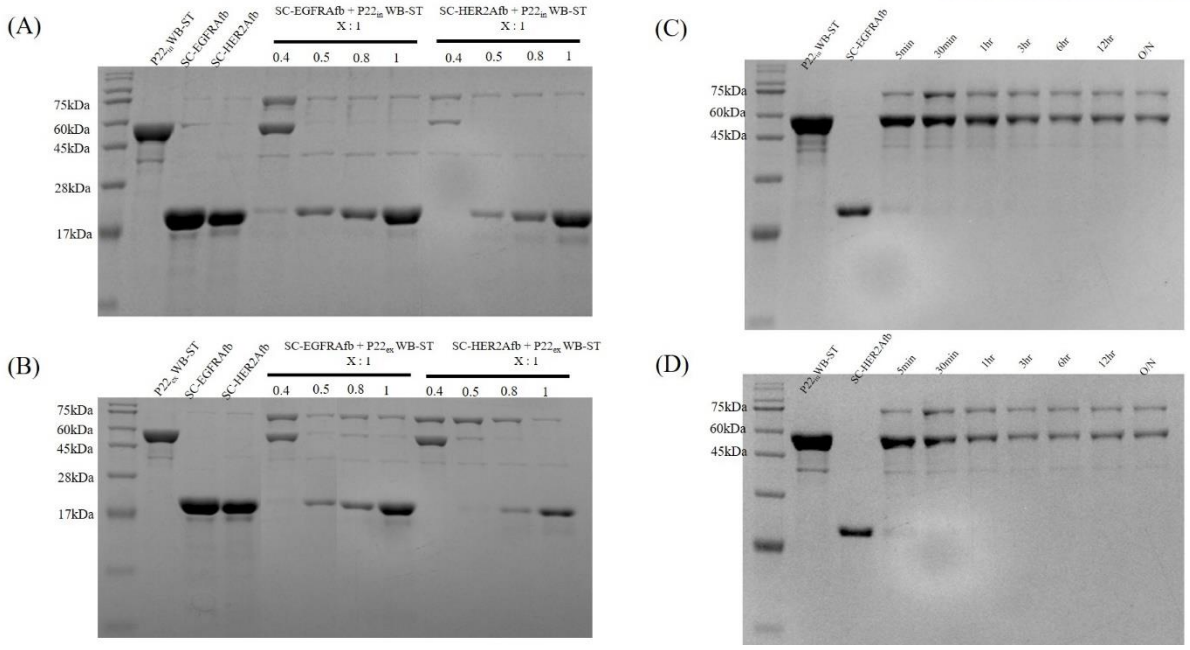

Figure 3.2 SDS-PAGE analyses of reaction results of P22 VLP-ST and SC-Afb at various input ratio and reaction times. Reaction resultants of (a) P22in WB-ST with SC-Afb and (b) P22ex WB-ST with SCAfb at various input ratio (1:0.4, 1:0.5, 1:0.8 and 1:1 molar ratios). Reaction results of (c) P22in WB-ST with SC-EGFRAfb and (d) P22in WB-ST with SC-HER2Afb at various reaction times as indicated.

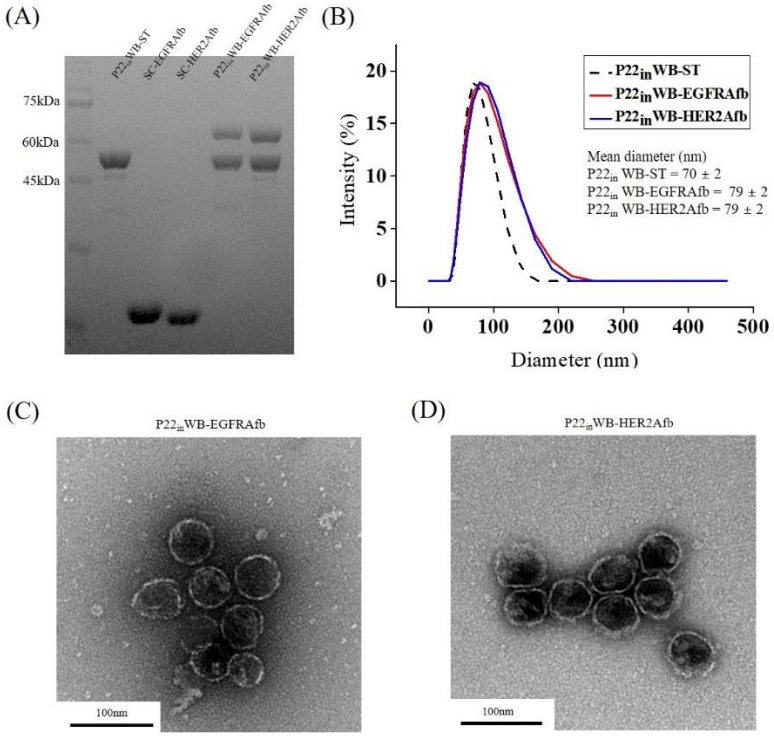

Figure 3.3 Characterization of $P22_{in}$ WB-Afb. (A) SDS-PAGE analyses of reaction results of $P22_{in}$ WB-ST and SC-EGFRAfb or SC-HER2Afb at an optimal input ratio. (B) Dynamic light scattering (DLS) analyses of the reaction results of $P22_{in}$ WB-ST and SC-EGFRAfb or SC-HER2Afb and $P22_{in}$ WB-ST only. Transmission electron microscopy images of $P22_{in}$ WB-ST/SC-EGFRAfb (C) and $P22_{in}$ WB-ST/SC-HER2Afb (D) stained with 2% uranyl acetate

Isopeptide bond formation between P22 WB-ST and SC-Afb was almost complete within 30 min (Figure 3.2C and D), and there was no noticeable amount of aggregation after an overnight reaction. The average diameter of P22 WB-ST/SC-Afb determined by DLS was 79 ± 2 nm, slightly larger than that of P22 WB-ST (70 ± 2 nm), indicating that SC-Afb are covalently attached to the exterior surfaces of P22 WB-ST (Figure 3.3B). TEM images of SC-Afb-treated P22 WB-ST showed intact cage architectures, although we could not clearly observe extra density on their surfaces (Figure 3.3C and D). To test whether each P22 WB-ST/SC-Afb could selectively recognize its target cells and bind tightly to them, we labeled P22 WB-ST/SC-Afb (P22 WB-ST/SC-EGFRAfb or P22 WB-ST/SC-HER2Afb) with fluorescein-5-maleimide (F5M) via a thiol-maleimide coupling reaction. P22 WB-ST/SC-Afb has one cysteine per subunit either on the interior ($P22_{in}$ WB-ST) or the exterior surface ($P22_{ex}$ WB-ST) of P22 WB-ST. We first tested $P22_{in}$ WB-ST, because interior fluorescein labeling would not interrupt the binding capacity of the affibody molecules displayed on the exterior surfaces of the P22 WB-ST/SC-Afb. We determined the degree of fluorescein conjugation to $P22_{in}$ WB-ST/SC-Afb by measuring absorbance at 488 and 280 nm, representing the amounts of fluorescein and $P22_{in}$ WB-ST subunit concentrations, respectively. Almost every subunit of $P22_{in}$ WB-ST was labeled with one fluorescein ($fP22_{in}$ WB-ST, Figure 3.4). Subsequently, SC-EGFRAfb and SC-HER2Afb were covalently ligated to $fP22_{in}$ WB-ST by simply mixing them at the previously determined optimized reaction ratio ($fP22_{in}$ WB-ST subunit/SC-Afb = 1:0.4).

MDA-MB-468 cells, known to overexpress EGFR on their membranes, and SK-BR-3 cells, known to overexpress HER2 on their membranes, were prepared and treated with $fP22_{in}$ WB-ST/SC-EGFRAfb and $fP22_{in}$ WB-ST/SC-HER2Afb, respectively. The fluorescent microscopy images showed that $fP22_{in}$ WB-ST/SC-EGFRAfb and $P22_{in}$ WB-ST/SC-HER2Afb bound efficiently to their corresponding MDA-MB-468 and SK-BR-3 cells, whereas cells treated with $fP22_{in}$ WB-ST did not exhibit any fluorescent signal (Figure 3.5A and B). MCF-7 and MCF-10A cells, which do not overexpress EGFR and HER2 respectively, were also treated with $fP22_{in}$ WB-ST/SC-EGFRAfb and $fP22_{in}$ WB-ST/SC-HER2Afb, respectively, as negative controls and did not show any fluorescent signals (Figure 3.6A and B). These data indicated that $P22_{in}$ WB-ST/SC-Afb efficiently and selectively bound to their target receptor molecules allowing the detection of specific target cells, with minimal non-specific binding. We also used $P22_{ex}$ WB-ST instead of $P22_{in}$ WB-ST and obtained almost identical results (Figure 3.7 and Figure 3.8) demonstrating that the exterior chemical conjugations of fluorescein do not interfere with targeting ligand ligations or target cell bindings.

To assess the potential of P22 WB-ST/SC-Afb as modular drug carriers, we chemically conjugated 6-maleimidocaproyl hydrazine, a prodrug of doxorubicin (AlDox) to $P22_{in}$ WB-ST instead of to F5M, as a representative anticancer drug. AlDox is a doxorubicin prodrug that contains a maleimide moiety attached via an acid-sensitive hydrazine linker [42]. When AlDox is trapped in acidic conditions, such as those in the endosome, lysosomes, and tumor environments, doxorubicin (Dox) is released through

(a)

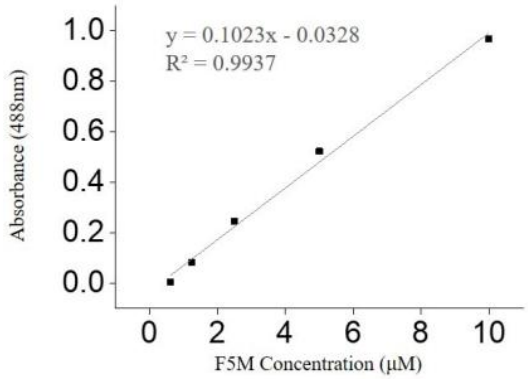

(b)

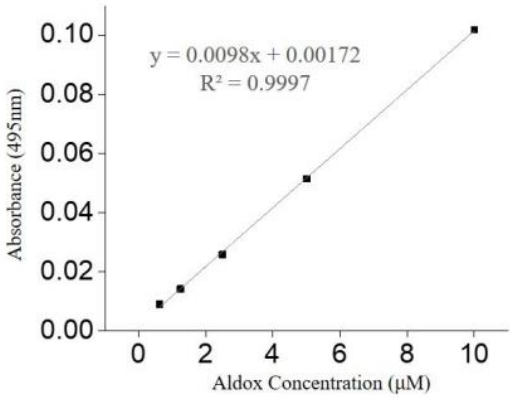

(c)

	Absorbance (RU)	Dye Concentration (μM)	P22 VLP Concentration (μM)	Ratio
F5M	0.204	2.314	2.5	0.926
AlDox	0.0301	2.895	2.5	1.158

Figure 3.4 Concentration dependent absorbance profiles of fluorescein-5-maleimide (a) and Aldoxorubicin (b). (c) Binding ratio of F5M and AlDox to P22 VLP-ST based on absorbance profiles.

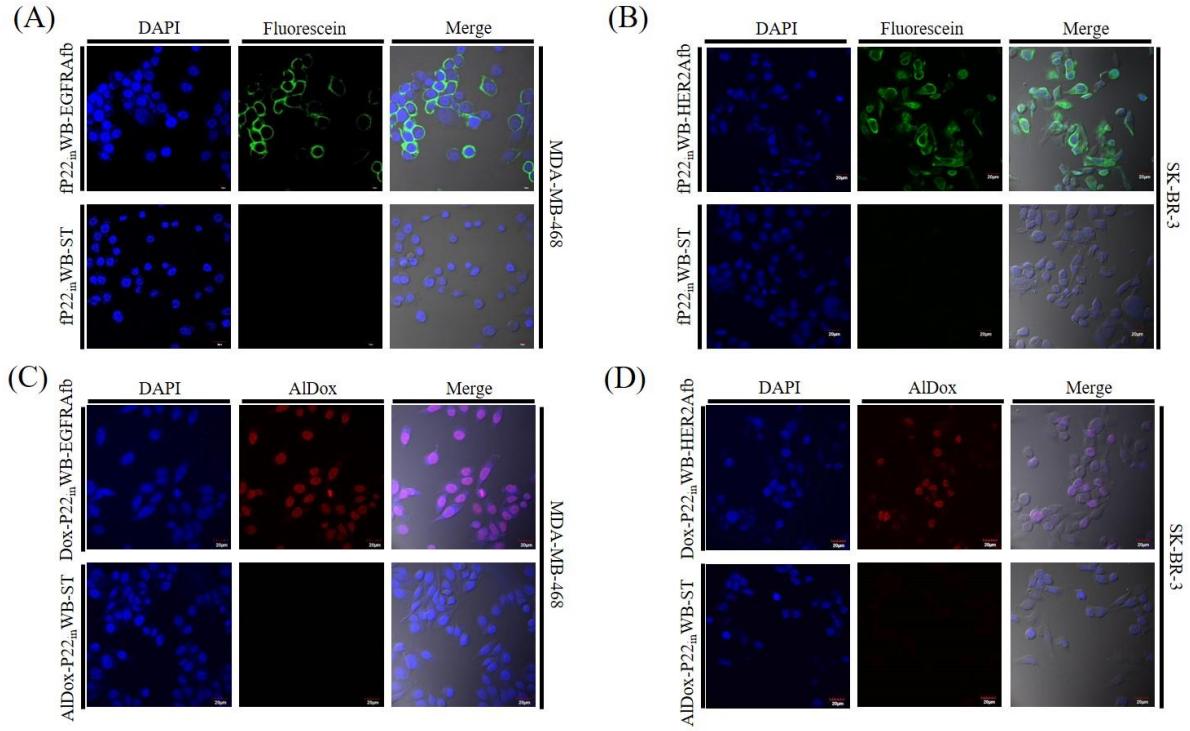

Figure 3.5 Fluorescent microscopic images of MDA-MB-468 cells (a) and SK-BR-3 cells (b) treated with $fP22_{in}$ WB-ST/SC-EGFRAfb and $fP22_{in}$ WB-ST/SC-HER2Afb, respectively. $fP22_{in}$ WB-ST was also independently treated (lower panels). Fluorescent microscopic images of MDA-MB-468 cells (c) and SK-BR-3 cells (d) treated with AlDox-$P22_{in}$ WB-ST/SC-EGFRAfb and AlDox-$P22_{in}$ WB-ST/SC-HER2Afb, respectively. AlDox-$P22_{in}$ WB-ST was also independently treated (lower panels). Treated samples and cells are indicated on the left and right of the image panels, respectively. Nuclei are stained by DAPI (left panels, blue), fluorescein and AlDox are visualized in green and red, respectively (upper panels). Scale bar = 20 μm

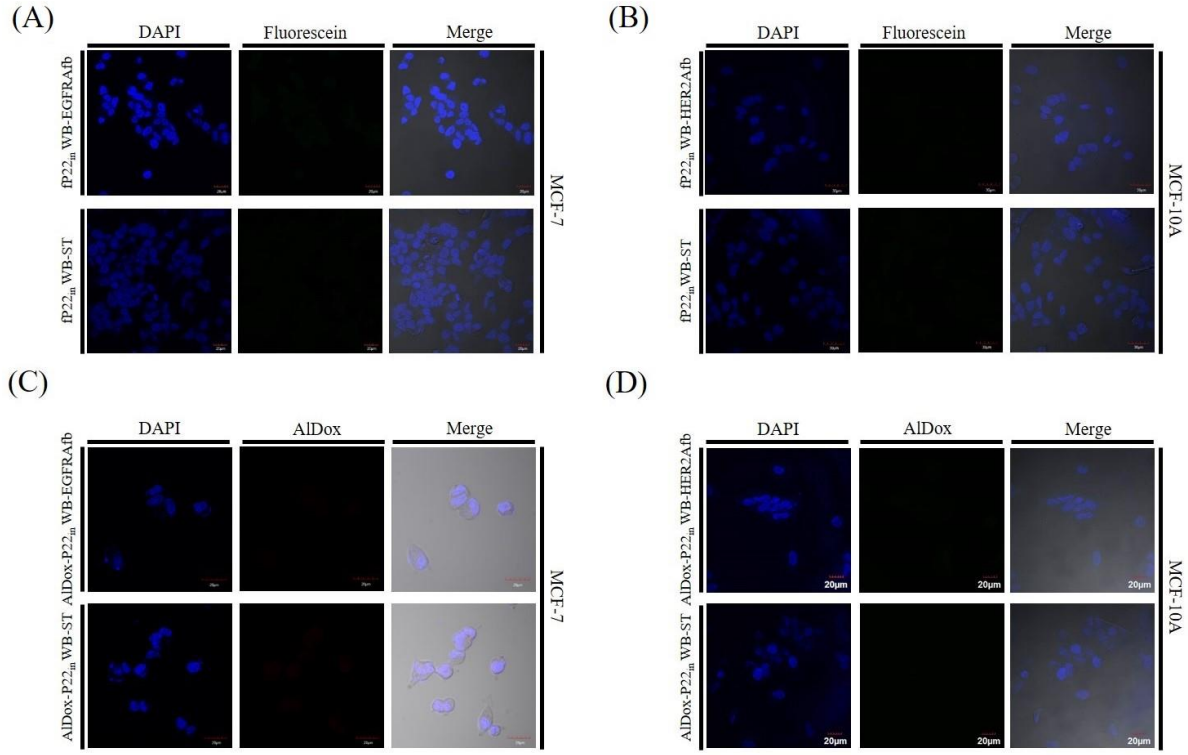

Figure 3.6 Fluorescent microscopic images of MCF-7 cells (a) and MCF-10A cells (b) treated with fP22in WB-ST/SC-EGFRAfb and fP22in WB-ST/SC-HER2Afb, respectively. fP22in WB-ST was also independently treated (lower panels). Fluorescent microscopic images of MCF-7 cells (c) and MCF10A cells (d) treated with AlDox-P22in WB-ST/SC-EGFRAfb and AlDox-P22In WB-ST/SC-HER2Afb, respectively. AlDox-P22in WB-ST was also independently treated (lower panels). Treated samples and cells are indicated on the left and right of the image panels, respectively. Nuclei are stained by DAPI (left panels, blue), fluorescein and AlDox are visualized in green and red, respectively (upper panels). Scale bar = 20 μm

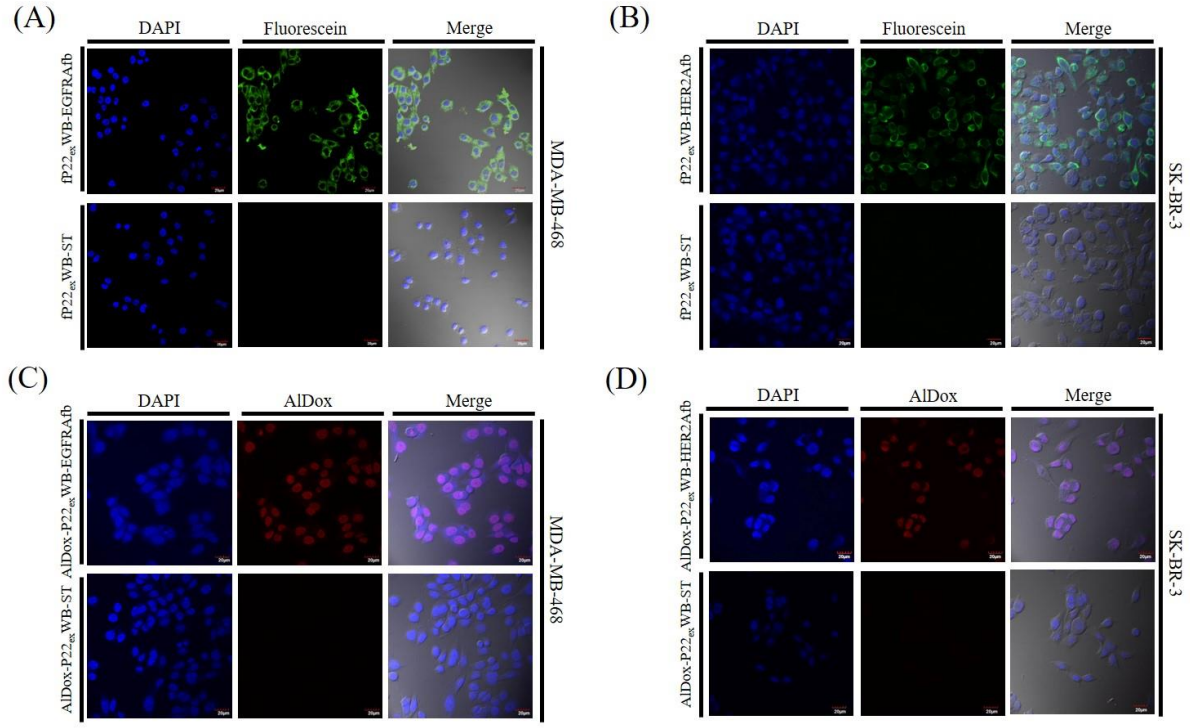

Figure 3.7 Fluorescent microscopic images of MDA-MB-468 cells (a) and SK-BR-3 cells (b) treated with fP22ex WB-ST/SC-EGFRAfb and fP22ex WB-ST/SC-HER2Afb, respectively. fP22ex WB-ST was also independently treated (lower panels). Fluorescent microscopic images of MDA-MB-468 cells (c) and SK-BR-3 cells (d) treated with AlDox-P22ex WB-ST/SC-EGFRAfb and AlDox-P22ex WB-ST/SCHER2Afb, respectively. AlDox-P22ex WB-ST was also independently treated (lower panels). Treated samples and cells are indicated on the left and right of the image panels, respectively. Nuclei are stained by DAPI (left panels, blue), fluorescein and AlDox are visualized in green and red, respectively (upper panels). Scale bar = 20 μm

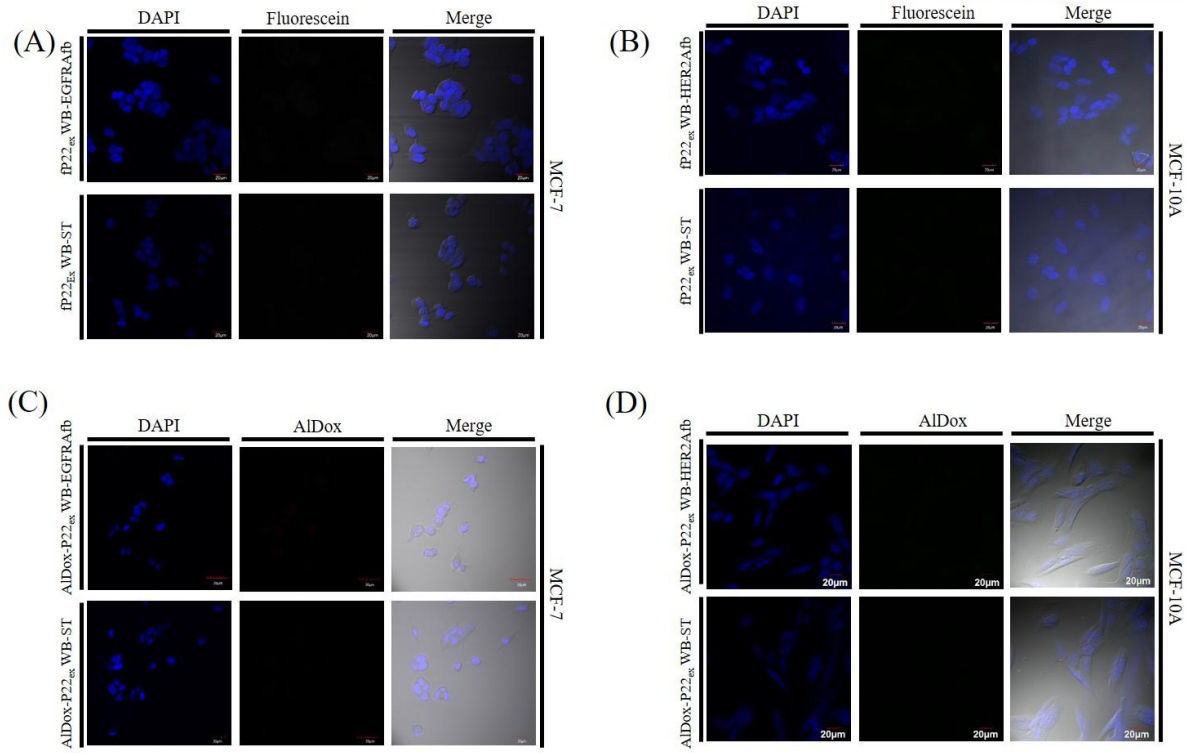

Figure 3.8 Fluorescent microscopic images of MCF-7 cells (a) and MCF-10A cells (b) treated with fP22ex WB-ST/SC-EGFRAfb and fP22ex WB-ST/SC-HER2Afb, respectively. fP22ex WB-ST was also independently treated (lower panels). Fluorescent microscopic images of MCF-7 cells (c) and MCF10A cells (d) treated with AlDox-P22ex WB-ST/SC-EGFRAfb and AlDox-P22ex WB-ST/SC-HER2Afb, respectively. AlDox-P22ex WB-ST was also independently treated (lower panels). Treated samples and cells are indicated on the left and right of the image panels, respectively. Nuclei are stained by DAPI (left panels, blue), fluorescein and AlDox are visualized in green and red, respectively (upper panels). Scale bar = 20 μm

low pH-induced cleavage of the hydrazine linkage and the released Dox can enter the nucleus, disrupting the genomic DNA, DNA repair systems, or both [43-44]. As with F5M, we conjugated $P22_{in}$ WB-ST with AlDox and subsequently ligated them with SC-Afb (AlDox-$P22_{in}$ WB-ST/SC-EGFRAfb or AlDox-$P22_{in}$ WB-ST/SC-HER2Afb). Almost every subunit of $P22_{in}$ WB-ST was conjugated with AlDox (Figure 3.4), and their architecture was not altered. MDA-MB-468 and SK-BR-3 cells were treated with AlDox-$P22_{in}$ WB-ST/SC-EGFRAfb and AlDox-$P22_{in}$ WB-ST/SC-HER2Afb, respectively. Red fluorescent signals from the released Dox appeared in the nuclei of the cells treated with AlDox-$P22_{in}$ WB-ST/SC-EGFRAfb or AlDox-$P22_{in}$ WB-ST/SC-HER2Afb but not with AlDox-$P22_{in}$ WB-ST (Figure 3.5C and D). These results indicated that AlDox-$P22_{in}$ WB-ST/SC-EGFRAfb and AlDox-$P22_{in}$ WB-ST/SC-HER2Afb selectively bound to EGFR and HER2 on the surface of MDA-MB-468 and SK-BR-3 cells, respectively, resulting in receptor-mediated endocytosis and subsequent cleavage of the hydrazine linkage in endosomes. Dox released from endosomes enters the nuclei and kills the cells. MCF-7 and MCF-10A cells were also treated with AlDox-$P22_{in}$ WB-ST/SC-EGFRAfb and AlDox-$P22_{in}$ WB-ST/SC-HER2Afb, and no Dox signal was detected (Figure 3.6C and D). These data suggested that AlDox-$P22_{in}$ WB-ST/SC-Afb do not bind to any cells non-specifically, consistent with the observations made using fluorescent microscopy, thus avoiding non-specific delivery of drugs to non-target cells. We performed the same experiments with AlDox-$P22_{ex}$ WB-ST/SC-EGFRAfb and AlDox-$P22_{ex}$ WB-ST/SC-HER2Afb and obtained almost identical results (Figure 3.7 and Figure 3.8). These data indicated that targeting, imaging, and therapeutic molecules could be simultaneously incorporated into P22 WB-ST and the system can deliver cargo molecules to target sites selectively and precisely.

To evaluate the cytotoxicity of Dox delivered by P22 WB-ST/SC-Afb, 3-(4,5-dimethylthiazol-2-yl)-2,5-diphenyl-tetrazolium bromide (MTT) cell viability assays were performed. MDA-MB-468 and SK-BR-3 cells were treated with AlDox-$P22_{in}$ WB-ST/SC-EGFRAfb and AlDox-$P22_{in}$ WB-ST/SC-HER2Afb, respectively, for 3 h. Free Dox was used as a positive control and $P22_{in}$ WB-ST/SC-Afb without AlDox as a negative control. Following incubation, the cells were washed with growth media and cultured for an additional 48 h before cell viability was measured with MTT assays. The cytotoxic effects of both AlDox-$P22_{in}$ WB-ST/SC-Afb and free Dox on MDA-MB-468 or SK-BR-3 cells increased in a dose-dependent manner (Figure 3.9A and B). AlDox-$P22_{in}$ WB-ST/SC-EGFRAfb had slightly higher cytotoxicity to MDA-MB-468 cells than Dox-treated cells. These results indicated that active targeting of P22 WB-ST/SC-EGFRAfb delivered Dox more effectively than the diffusion of free Dox. However, in the case of SK-BR-3 cells, Aldox-P22 WB-ST/SC-HER2Afb exhibited similar cytotoxicity to that of free Dox. One of the main advantages of targeted delivery should be a reduction in side effects, achieved by minimizing off-target effects. To test for off-target effects of AlDox-$P22_{in}$ WB-ST/SC-Afb, MCF-7 and MCF-10A cells were treated with AlDox-$P22_{in}$ WB-ST/SC-EGFRAfb and AlDox-$P22_{in}$ WB-ST/SC-HER2Afb, respectively, and free Dox (Figure 3.9C and D).

Approximately 50%–60% of MCF-7 and MCF-10A cells were killed with 20 μM of free Dox, a similar proportion to those treated with MDA-MB 468 and SK-BR3, whereas only basal levels of MCF-7 and MCF-10A cells were killed by AlDox-P22$_{in}$ WB-ST/SC-EGFRAfb and AlDox-P22$_{in}$ WB-ST/SC-HER2Afb. These results indicated that P22$_{in}$ WB-ST/SC-Afb could be used as a drug delivery vehicle in target cells, minimizing the off-target effects of commonly used prodrugs. We also evaluated the cytotoxicity of AlDox-P22$_{ex}$ WB-ST/SC-Afb and obtained almost identical results (Figure 3.10). These results indicated that attachment of cargo molecules to the exterior surface of P22 WB-ST/SC-Afb does not affect their targeting capability and that both the interior and exterior surfaces of P22 WB-ST/SC-Afb could be utilized for multiple cargo loading sites.

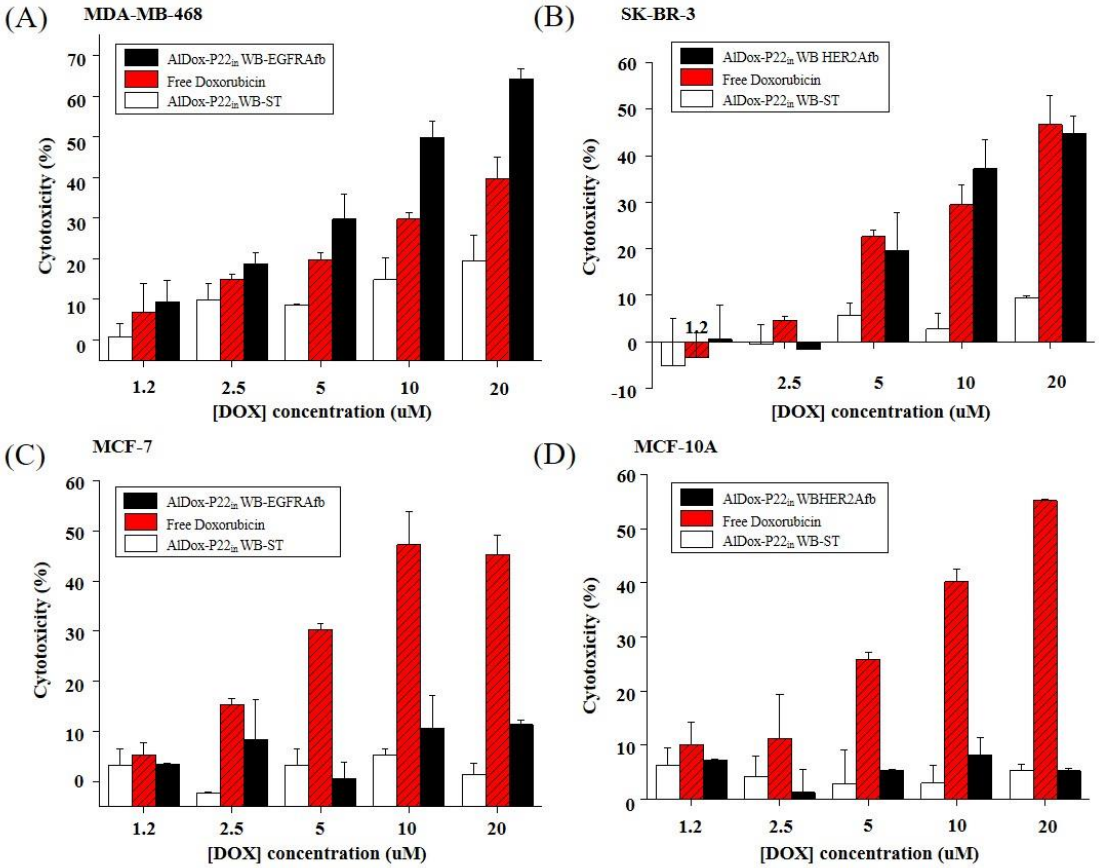

Figure 3.9 MTT cell viability assay. (a) Dose-dependent cytotoxic effects of AlDox-$P22_{in}$ WB-ST/SC-EGFRAfb (black), free Dox (gray), and AlDox-$P22_{in}$ WB-ST (white) on MDA-MB-468 cells. (b) Dose-dependent cytotoxic effects of AlDox-$P22_{in}$ WB-ST/SC-HER2Afb (black), free Dox (gray), and AlDox-$P22_{in}$ WB-ST (white) on SK-BR-3 cells. (c) Dose-dependent cytotoxic effects of AlDox-$P22_{in}$ WB-ST/SC-EGFRAfb (black), free Dox (gray), and AlDox-$P22_{in}$ WB-ST (white) on MCF-7 cells. (d) Dose-dependent cytotoxic effects of AlDox-$P22_{in}$ WB-ST/SC-HER2Afb (black), free Dox (gray), and AlDox-$P22_{in}$ WB-ST (white) on MCF-10A cells. Five independent experiments were performed, and error bars are indicated

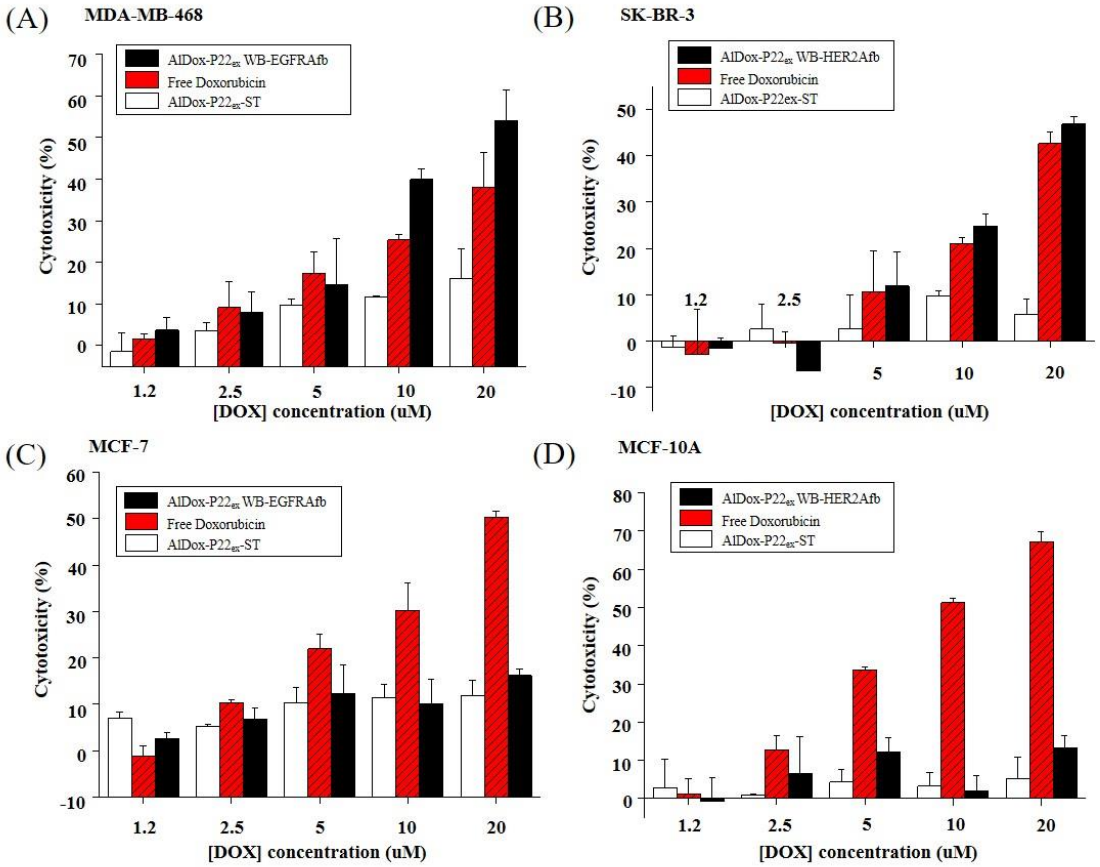

Figure 3.10 MTT cell viability assay. (a) Dose-dependent cytotoxic effects of AlDox-P22ex WB-ST/SCEGFRAfb (black), free Dox (grey), and AlDox-P22ex WB-ST (white) on MDA-MB 468 cells. (b) Dosedependent cytotoxic effect of AlDox-P22ex WB-ST/SC-HER2Afb (black), free Dox (grey), and AlDoxP22ex WB-ST (white) on SK-BR 3 cells. (c) Dose-dependent cytotoxic effects of AlDox-P22ex WBST/SC-EGFRAfb (black), free Dox (grey), and AlDox-P22ex WB-ST (white) on MCF-7 cells. (d) Dosedependent cytotoxic effects of AlDox-P22ex WB-ST/SC-HER2Afb (black), free Dox (grey), and AlDox-P22ex WB-ST (white) on MCF-10A cells. Five independent experiments were performed, and error bars are indicated

3.4 Conclusions

In this study, we developed P22 VLP-based target-tunable delivery nanoplatforms that can deliver fluorescent dyes or anticancer drugs, such as Dox to target cells with precision. ST-inserted P22 WB and SC-fused EGFR and HER2 affibody molecules were independently prepared and were covalently ligated according to their target cells. A fluorescent dye, fluorescein, and the prodrug AlDox were chemically conjugated to P22 WB-ST/SC-Afb on either interior or exterior surfaces and successfully delivered to the cytosol and nuclei of their target cells, resulting in effective cell imaging and selective target cell killing. The AlDox-P22 WB-ST/SC-Afb showed high specificity toward their target cells, minimizing nonspecific delivery of toxic drugs to nontargeted cells. P22 VLP had a robust genome-free hollow structure with high symmetry, providing sufficient space for loading therapeutic cargoes and diagnostic probes on the interior or exterior surfaces, and the SpyTag/SpyCatcher ligation system allowed us to covalently display two different large targeting ligands on P22 VLP. The approach we describe here can be applied to multifunctional delivery by the conjugation of two or more functional proteins, as well as affibody molecules. We anticipate that this platform could display proteins even larger than affibody molecules by controlling the molar ratio with respect to P22 VLP. In addition to the exterior surface with target-specific ligands, the interior cavity of P22 VLP can be used for encapsulating functional proteins, such as enzymes and therapeutic proteins. The dual modification approach may provide new opportunities for developing biomolecule-based target-specific functional protein delivery systems.

3.5 References

1. Ma, Y.; Nolte, R. J.; Cornelissen, J. J., Virus-based nanocarriers for drug delivery. *Adv Drug Deliv Rev* **2012,** *64* (9), 811-25.

2. Lee, E. J.; Lee, N. K.; Kim, I.-S., Bioengineered protein-based nanocage for drug delivery. *Advanced drug delivery reviews* **2016,** *106*, 157-171.

3. Czapar, A. E.; Steinmetz, N. F., Plant viruses and bacteriophages for drug delivery in medicine and biotechnology. *Curr Opin Chem Biol* **2017,** *38*, 108-116.

4. Rohovie, M. J.; Nagasawa, M.; Swartz, J. R., Virus-like particles: Next-generation nanoparticles for targeted therapeutic delivery. *Bioeng Transl Med* **2017,** *2* (1), 43-57.

5. Choi, B.; Kim, H.; Choi, H.; Kang, S., Protein Cage Nanoparticles as Delivery Nanoplatforms. *Adv Exp Med Biol* **2018,** *1064*, 27-43.

6. Tetter, S.; Hilvert, D., Enzyme Encapsulation by a Ferritin Cage. *Angew Chem Int Ed Engl* **2017,** *56* (47), 14933-14936.

7. Kim, H.; Kang, Y. J.; Min, J.; Choi, H.; Kang, S., Development of an antibody-binding modular nanoplatform for antibody-guided targeted cell imaging and delivery. *Rsc Advances* **2016,** *6* (23), 19208-19213.

8. Jordan, P. C.; Patterson, D. P.; Saboda, K. N.; Edwards, E. J.; Miettinen, H. M.; Basu, G.; Thielges, M. C.; Douglas, T., Self-assembling biomolecular catalysts for hydrogen production. *Nature chemistry* **2016,** *8* (2), 179.

9. Choi, B.; Moon, H.; Hong, S. J.; Shin, C.; Do, Y.; Ryu, S.; Kang, S., Effective Delivery of Antigen-Encapsulin Nanoparticle Fusions to Dendritic Cells Leads to Antigen-Specific Cytotoxic T Cell Activation and Tumor Rejection. *ACS Nano* **2016,** *10* (8), 7339-50.

10. Song, Y.; Kang, Y. J.; Jung, H.; Kim, H.; Kang, S.; Cho, H., Lumazine Synthase Protein Nanoparticle-Gd (III)-DOTA Conjugate as a T 1 contrast agent for high-field MRI. *Scientific reports* **2015,** *5*, 15656.

11. Lucon, J.; Qazi, S.; Uchida, M.; Bedwell, G. J.; LaFrance, B.; Prevelige, P. E.; Douglas, T., Use of the interior cavity of the P22 capsid for site-specific initiation of atom-transfer radical polymerization with high-density cargo loading. *Nature Chemistry* **2012,** *4* (10), 781-788.

12. Aumiller, W. M.; Uchida, M.; Douglas, T., Protein cage assembly across multiple length scales. *Chem Soc Rev* **2018,** *47* (10), 3433-3469.

13. Azuma, Y.; Edwardson, T. G. W.; Hilvert, D., Tailoring lumazine synthase assemblies for bionanotechnology. *Chem Soc Rev* **2018,** *47* (10), 3543-3557.

14. Min, J.; Kim, S.; Lee, J.; Kang, S., Lumazine synthase protein cage nanoparticles as modular delivery platforms for targeted drug delivery. *RSC Advances* **2014,** *4* (89), 48596-48600.

15. Min, J.; Moon, H.; Yang, H. J.; Shin, H. H.; Hong, S. Y.; Kang, S., Development of P22 viral capsid nanocomposites as anti-cancer drug, bortezomib (BTZ), delivery nanoplatforms. *Macromol Biosci* **2014,** *14* (4), 557-64.

16. Smith, M. L.; Lindbo, J. A.; Dillard-Telm, S.; Brosio, P. M.; Lasnik, A. B.; McCormick, A. A.; Nguyen, L. V.; Palmer, K. E., Modified Tobacco mosaic virus particles as scaffolds for display of protein antigens for vaccine applications. *Virology* **2006,** *348* (2), 475-488.

17. Zhou, H. X., Loops, linkages, rings, catenanes, cages, and crowders: entropy-based strategies for stabilizing proteins. *Acc Chem Res* **2004,** *37* (2), 123-30.

18. Kang, S.; Uchida, M.; O'Neil, A.; Li, R.; Prevelige, P. E.; Douglas, T., Implementation of p22 viral capsids as nanoplatforms. *Biomacromolecules* **2010,** *11* (10), 2804-2809.

19. Wang, J. G.; Fang, T.; Li, M.; Zhang, W. J.; Zhang, Z. P.; Zhang, X. E.; Li, F., Intracellular delivery of peptide drugs using viral nanoparticles of bacteriophage P22: covalent loading and cleavable release. *J Mater Chem B* **2018,** *6* (22), 3716-3726.

20. Patterson, D.; Schwarz, B.; Avera, J.; Western, B.; Hicks, M.; Krugler, P.; Terra, M.; Uchida, M.; McCoy, K.; Douglas, T., Sortase-Mediated Ligation as a Modular Approach for the Covalent Attachment of Proteins to the Exterior of the Bacteriophage P22 Virus-like Particle. *Bioconjug Chem* **2017,** *28* (8), 2114-2124.

21. Zakeri, B.; Fierer, J. O.; Celik, E.; Chittock, E. C.; Schwarz-Linek, U.; Moy, V. T.; Howarth, M., Peptide tag forming a rapid covalent bond to a protein, through engineering a bacterial adhesin. *Proceedings of the National Academy of Sciences* **2012,** *109* (12), E690-E697.

22. Bae, Y.; Kim, G. J.; Kim, H.; Park, S. G.; Jung, H. S.; Kang, S., Engineering Tunable Dual Functional Protein Cage Nanoparticles Using Bacterial Superglue. *Biomacromolecules* **2018**.

23. Oh, J. Y.; Kim, H. S.; Palanikumar, L.; Go, E. M.; Jana, B.; Park, S. A.; Kim, H. Y.; Kim, K.; Seo, J. K.; Kwak, S. K.; Kim, C.; Kang, S.; Ryu, J. H., Cloaking nanoparticles with protein corona shield for targeted drug delivery. *Nat Commun* **2018,** *9* (1), 4548.

24. Moon, H.; Bae, Y.; Kim, H.; Kang, S., Plug-and-playable fluorescent cell imaging modular toolkits using the bacterial superglue, SpyTag/SpyCatcher. *Chemical Communications* **2016,** *52* (97), 14051-14054.

25. Choi, H.; Choi, B.; Kim, G. J.; Kim, H. u.; Kim, H.; Jung, H. S.; Kang, S., Fabrication of Nanoreaction Clusters with Dual-Functionalized Protein Cage Nanobuilding Blocks. *Small* **2018,** *14* (35), 1801488.

26. Brune, K. D.; Leneghan, D. B.; Brian, I. J.; Ishizuka, A. S.; Bachmann, M. F.; Draper, S. J.; Biswas, S.; Howarth, M., Plug-and-Display: decoration of Virus-Like Particles via isopeptide bonds for modular immunization. *Sci Rep* **2016,** *6*, 19234.

27. Bruun, T. U. J.; Andersson, A. C.; Draper, S. J.; Howarth, M., Engineering a Rugged Nanoscaffold To Enhance Plug-and-Display Vaccination. *ACS Nano* **2018,** *12* (9), 8855-8866.

28. Ke, X.; Zhang, Y.; Zheng, F.; Liu, Y.; Zheng, Z.; Xu, Y.; Wang, H., SpyCatcher-SpyTag mediated in situ labelling of progeny baculovirus with quantum dots for tracking viral infection in living cells. *Chem Commun (Camb)* **2018,** *54* (10), 1189-1192.

29. Kasaraneni, N.; Chamoun-Emanuelli, A. M.; Wright, G.; Chen, Z. L., Retargeting Lentiviruses via SpyCatcher-SpyTag Chemistry for Gene Delivery into Specific Cell Types. *Mbio* **2017,** *8* (6).

30. Leneghan, D. B.; Miura, K.; Taylor, I. J.; Li, Y.; Jin, J.; Brune, K. D.; Bachmann, M. F.; Howarth, M.; Long, C. A.; Biswas, S., Nanoassembly routes stimulate conflicting antibody quantity and quality for transmission-blocking malaria vaccines. *Sci Rep* **2017,** *7* (1), 3811.

31. Brune, K. D.; Buldun, C. M.; Li, Y. Y.; Taylor, I. J.; Brod, F.; Biswas, S.; Howarth, M., Dual Plug-and-Display Synthetic Assembly Using Orthogonal Reactive Proteins for Twin Antigen Immunization. *Bioconjugate Chem* **2017,** *28* (5), 1544-1551.

32. Thrane, S.; Janitzek, C. M.; Matondo, S.; Resende, M.; Gustavsson, T.; de Jongh, W. A.; Clemmensen, S.; Roeffen, W.; van de Vegte-Bolmer, M.; van Gemert, G. J.; Sauerwein, R.; Schiller, J. T.; Nielsen, M. A.; Theander, T. G.; Salanti, A.; Sander, A. F., Bacterial superglue enables easy development of efficient virus-like particle based vaccines. *Journal of Nanobiotechnology* **2016,** *14*.

33. Janitzek, C. M.; Matondo, S.; Thrane, S.; Nielsen, M. A.; Kavishe, R.; Mwakalinga, S. B.; Theander, T. G.; Salanti, A.; Sander, A. F., Bacterial superglue generates a full-length circumsporozoite protein virus-like particle vaccine capable of inducing high and durable antibody responses. *Malaria J* **2016,** *15*.

34. Singh, S. K.; Thrane, S.; Janitzek, C. M.; Nielsen, M. A.; Theander, T. G.; Theisen, M.; Salanti, A.; Sander, A. F., Improving the malaria transmission-blocking activity of a Plasmodium falciparum 48/45 based vaccine antigen by SpyTag/SpyCatcher mediated virus-like display. *Vaccine* **2017,** *35* (30), 3726-3732.

35. Servid, A.; Jordan, P.; O'Neil, A.; Prevelige, P.; Douglas, T., Location of the Bacteriophage P22 Coat Protein C-Terminus Provides Opportunities for the Design of Capsid-Based Materials. *Biomacromolecules* **2013,** *14* (9), 2989-2995.

36. Min, J.; Jung, H.; Shin, H.-H.; Cho, G.; Cho, H.; Kang, S., Implementation of P22 viral capsids as intravascular magnetic resonance T 1 contrast conjugates via site-selective attachment of Gd (III)-chelating agents. *Biomacromolecules* **2013,** *14* (7), 2332-2339.

37. Orlova, A.; Magnusson, M.; Eriksson, T. L. J.; Nilsson, M.; Larsson, B.; Hoiden-Guthenherg, I.; Widstrom, C.; Carlsson, J.; Tolmachev, V.; Stahl, S.; Nilsson, F. Y., Tumor Imaging using a picomolar affinity HER2 binding affibody molecule. *Cancer Res* **2006,** *66* (8), 4339-4348.

38. Friedman, M.; Orlova, A.; Johansson, E.; Eriksson, T. L. J.; Hoiden-Guthenberg, I.; Tolmachev, V.; Nilsson, F. Y.; Stahl, S., Directed evolution to low nanomolar affinity of a tumor-targeting epidermal growth factor receptor-binding affibody molecule. *J Mol Biol* **2008,** *376* (5),

1388-1402.

39. Verbeek, B. S.; Adriaansen-Slot, S. S.; Vroom, T. M.; Beckers, T.; Rijksen, G., Overexpression of EGFR and c-erbB2 causes enhanced cell migration in human breast cancer cells and NIH3T3 fibroblasts. *FEBS Lett* **1998,** *425* (1), 145-50.

40. Teschke, C. M.; McGough, A.; Thuman-Commike, P. A., Penton release from P22 heat-expanded capsids suggests importance of stabilizing penton-hexon interactions during capsid maturation. *Biophysical journal* **2003,** *84* (4), 2585-2592.

41. Patterson, D. P.; Prevelige, P. E.; Douglas, T., Nanoreactors by Programmed Enzyme Encapsulation Inside the Capsid of the Bacteriophage P22. *Acs Nano* **2012,** *6* (6), 5000-5009.

42. Willner, D.; Trail, P. A.; Hofstead, S. J.; King, H. D.; Lasch, S. J.; Braslawsky, G. R.; Greenfield, R. S.; Kaneko, T.; Firestone, R. A., (6-Maleimidocaproyl)hydrazone of doxorubicin--a new derivative for the preparation of immunoconjugates of doxorubicin. *Bioconjug Chem* **1993,** *4* (6), 521-7.

43. Thorn, C. F.; Oshiro, C.; Marsh, S.; Hernandez-Boussard, T.; McLeod, H.; Klein, T. E.; Altman, R. B., Doxorubicin pathways: pharmacodynamics and adverse effects. *Pharmacogenet Genomics* **2011,** *21* (7), 440-6.

44. Muller, I.; Jenner, A.; Bruchelt, G.; Niethammer, D.; Halliwell, B., Effect of concentration on the cytotoxic mechanism of doxorubicin--apoptosis and oxidative DNA damage. *Biochem Biophys Res Commun* **1997,** *230* (2), 254-7.

Chapter 4. Cloaking nanoparticles with protein corona shield for targeted drug delivery

4.1 Introduction

The application of nanoparticles is promising for the development of imaging and therapeutic agents through improved biodistribution and controlled drug release[1-3]. The rationale behind using nanoparticles is that those with diameters of <200 nm extravasate from the leaky tumor blood vessels are retained in the tumor due to the "enhanced permeability and retention" (EPR) effect[4]. Although few nanoparticle formulations (e.g., Abraxane and Doxil) are available in the market, the ubiquitous targeting approach suffers from several limitations including rapid clearance by the mononuclear phagocyte system (MPS) and low uptake into target tumors[5-6]. To improve the targeting ability, along with the EPR effect, an active targeting approach has been attempted by coating the particle surface with antibodies, proteins, or peptides that bind to receptors that are typically overexpressed on cancer cells[7]. However, recent reports have revealed only a modest increase in tumor targeting when this approach is applied; moreover, the addition of targeting ligands increased the clearance of nanoparticles by MPS, indicating that no definitive conclusion has been reached regarding the therapeutic efficacy of this technique[8-9]. In principle, when exposed to physiological environments, the nanoparticle surface is covered by various biomolecules to lower the surface energy by a combination of entropy-driven water molecule displacement, particle surface charge compensation, and screening of hydrophobic parts[10-12]. Biomolecule adsorption results in the formation of a layer, called a protein corona, and significantly changes the original molecular identity of the nanoparticle[13]. The formation of a protein corona on the nanoparticle surface can be regulated by modifying the nanoparticle surface with zwitterions, polyethylene glycol (PEG), carbohydrate moieties, and dysopsonic proteins, which can enhance the colloidal stability and prolong the circulation time in blood by enabling escape from MPS clearance[14-17]. However, these strategies are still limited at conferring targeting specificity since an additional targeting ligand increases the propensity for protein corona formation to mask the targeting ability and inhibit the biological effects of nanoparticles[18-24]. This can explain why many nanoparticles with active targeting systems have failed in clinical trials[25]. Therefore, to design nanoparticle-based therapeutic agents, there is a considerable need to regulate protein corona formation on nanoparticles[26-28] and to obtain a deeper understanding of the molecular mechanism involved in regulating nanoparticle–biological interactions. Here, we present a targeting system in which nanoparticles are supramolecularly pre-coated with a protein

corona shield (PCS) that reduce serum protein absorption while retaining targeting specificity (Scheme 4.1).

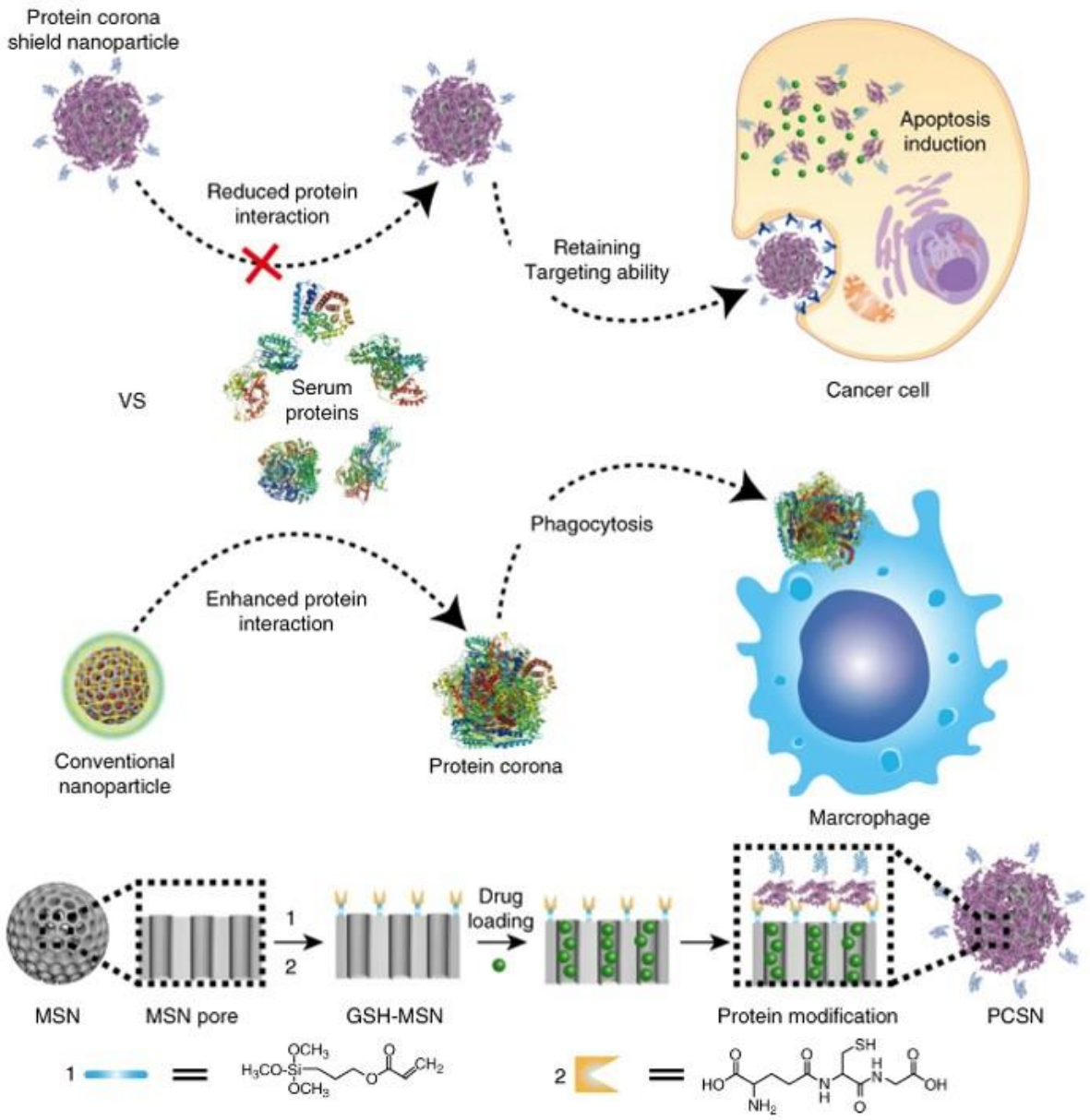

Scheme 4.1 Protein corona shield nanoparticle (PCSN). We introduce the protein corona shield (PCS) concept for an efficient target drug delivery system. Generally, nanoparticle drug carriers with a target ligand lose their targeting ability on being coated by blood proteins in a biological environment. However, the PCS system can inhibit blood protein adsorption to maintain the targeting ability and avoid unwanted clearance by the mononuclear phagocyte system.

4.2 Materials and Methods

Materials

Cetyltrimethylammonium bromide (CTAB), Pluronic® F-127 ($EO_{106}PO_{70}EO_{106}$), tetraethyl orthosilicate (TEOS; 98%, reagent grade), fluorescein isothiocyanate, toluene (99.9% anhydrous), pyridine, dimethylformamide (HPLC grade), disuccinimidyl suberate, and dimethyl sulfoxide were purchased from Sigma-Aldrich (Yongin S. Korea). 3-(Trimethoxysilyl) propyl acrylate, (3-aminopropyl) trimethoxysilane, succinic acid anhydride, and L-glutathione reduced (>98%) were purchased from Tokyo Chemical Industries (TCI) (Tokyo, Japan). 1,1′-Dioctadecyl-3,3,3′,3′-tetramethylindocarbocyanine perchlorate (DiI), DiD were purchased from Thermo Fisher. CPT was obtained from Ontario Chemicals Inc. (Ontario, Canada). Doxorubicin (Dox) was obtained from Acorn PharmaTech (Redwood City, CA, USA). Anhydrous ethanol, sodium hydroxide (NaOH; 99%), and ammonium hydroxide (29 wt%) were purchased from Samchun Chemical. All chemicals were used as received without further purification. Deionized (DI) water was produced by the Millipore Milli-Q System (18.2 MΩ cm). Isopropyl β-D-1-thiogalactopyranoside was purchased from Bio Basic. Lysozyme was purchased from Sigma-Aldrich. PBS (10×) without calcium or magnesium was purchased from Lonza. One milliliter HisTrap FF column was purchased from GE HealthCare. DuoflowTM chromatography system was purchased from Bio-rad. BCA assay was purchased from Thermo Fisher. MassPREP microdesalting column and Xevo G2 TOF MS were purchased from Waters. All the other chemicals were purchased from Bioshop. SK-BR-3 cells were purchased from the Korean cell line bank (KCLB catalog No. 30030). MDA-MB-468 cells were purchased from the Amerian Type Culuture Collection (ATCC Catalog No. HTB-132). All cell culture reagents and medium were from Life Technologies (S. Korea) and FBS was purchased from Gold Standard (USA). The graphics found in the figures were created by a co-author.

Cell culture

Human breast cancer cells derived from the metastatic sites MDA-MB468 and SK-BR3 were obtained. Normal macrophage cell lines RAW264.7 and HeK293T were obtained as a gift from Prof. Hyun Woo Rhee at UNIST. SK-BR3 and RAW264.7 cells were cultured in DMEM medium (Invitrogen, S. Korea), and MDA-MB468 in Leibovitz-L-15 media (Invitrogen, S. Korea) was supplemented with 10% FBS, 100 µg/mL streptomycin, and 100 U/mL penicillin at 37 °C in a humidified incubator containing 5% CO_2 and 95% air. The medium was replenished every other day, and the cells were subcultured after reaching >85% confluence.

Cell viability analysis

The in vitro cell viabilities of various formulations against SK-BR3 and MDA-MB468 cells were determined by performing the Alamar blue dye assay (Invitrogen, Korea). Briefly, SK-BR3 and MDA-MB468 cells were cultured in 96-well (Thermo Scientific Inc. Korea) micro-titer plates at a density of 5×10^3 cells/well and then allowed to settle for 24 h under incubation at 37 °C, 95% air, and 5% CO_2. Then, the grown cells were treated with different concentrations of pristine MSN, GSH-MSN, and EGFR- and Her2-Afb-modified MSN (10 µg/mL to 1 mg/mL) in both cell lines and analyzed after 24-h incubation at an excitation wavelength of 565 nm and an emission wavelength of 590 nm using a fluorescence plate reader (Tecan Infinite Series, Germany). Similarly, CPT-loaded EGFR and Her2 PCSN along with free-CPT were analyzed using similar methods (0.01, 0.1, 0.25, 0.5, 1, 2.5, and 5 µg/mL of CPT).

Cellular uptake analysis

The cellular uptake of CPT-loaded nanoparticles was investigated with confocal microscopic and flow cytometric analyses. HeK293T, MDA-MB468, and SK-BR3 cells were seeded into two-well chambers with a cover glass (Lab Tek II; Thermo Scientific) at a seeding density of 2×10^5 cells/well. After a 24-h incubation, the cells were treated with CPT-loaded PCSN at a final concentration of CPT of 10 µg/mL at different time points and analyzed with confocal microscopy. Similarly, the cells were stained with lysotracker green (Lysotracker Green FM DND-26; Invitrogen) to check the colocalization with the CPT-loaded MSN. To evaluate the drug release from MSN, the FITC-conjugated MSNs were loaded with CPT and the releases at varying time points (2, 1, and 16 h) were checked. To evaluate cellular uptake, DiI-loaded MSNs were used for flow cytometric analysis. HeK293T, SK-BR3, and MDA-MB468 cells were seeded into six-well plates at a density of 1×10^6 cells per well and incubated in a complete medium for 24 h at 37 °C, 95% air, and 5% CO_2. The concentration of DiI nanoparticles was equivalent to a DiI dosage of 0.20 µg/mL. After the stipulated period of 4 and 6 h of incubation, the different treatment cells were trypsinized, harvested, rinsed with PBS, resuspended, and subjected to flow cytometry assay using BD-FACS Caliber. All experiments detected ≥10,000 cells, and the data were analyzed using the FlowJo software.

Endocytic pathway analysis

To check the endocytosis-mediated uptake, SK-BR3 cells were seeded into four-well chambers with cover glass and pretreated with different inhibitors, including sucrose (clathrin-mediated uptake, 400 nM), methyl-beta cyclodextrin (caveolae-mediated uptake), and amilorin (macropinocytosis), in a serum-free DMEM for 1 h and replaced with fresh media. Afterward, DiI-loaded PCSNs were added to the medium for another 1 h of incubation. Then, the cells were analyzed with a confocal microscope (Olympus FV1000) connected to a CO_2 incubator.

Animals and tumor models

Female nude mice (18 ± 2 g, 6 weeks of age) were fed under the condition of 22 ± 2 °C and 55 ± 5% humidity, with free access to food and water. All animal experiments were approved by the Institutional Animal Care and Use Committee at Ulsan National Institute of Science and Technology and conducted in compliance with the guidelines (UNIST-IACUC-17-29). To set up the tumor xenograft model, mice were subcutaneously inoculated in the right lower leg with 1×10^6 human breast cancer SK-BR3 cells. Tumor volume (V) was determined by the following equation: $V = L \times W^2/2$, where L and W are the length and width of the tumor, respectively. SK-BR3 tumor-bearing mice were used in the experiments when the tumor volumes reached approximately 100 mm^3.

In vivo and ex vivo fluorescence imaging

To evaluate the biodistribution of GSH-MSN, PEG-MSN, and PCSN loaded with a lipophillic dye, DiD (at 10 wt% loading capacity) was intravenously injected (0.1 mg/mL) into SK-BR3 tumor-bearing nude mice (7 mice/group). Then, the mice were anesthetized and imaged using an in vivo imaging system (Bruker Xtreme) with an excitation wavelength of 630 nm and emission wavelength of 700 nm. In vivo images were taken at 0.5, 1, 2, 4, 8, 10, 12, 24, 32, and 48 h. Then, the mice were killed to separate the organs and tumors for ex vivo imaging to determine the biodistribution pattern of DiD-loaded nanocarriers.

In vivo tumor inhibition analysis

Female nude mice (average weight 18.5 ± 2 g) were obtained from Orientbio, Korea, for the in vivo studies. All protocols for the in vivo experiments were approved by the UNIST-IACUC animal ethics approval committee. SK-BR3 tumor-bearing mice were used to carry out experiments when the tumor volumes reached approximately 300 mm^3. The tumor-bearing nude mice were randomly divided into five groups (6 mice per group). PBS, free-CPT, PCSN, CPT-loaded PEG-MSN, and CPT-loaded PCSN were intravenously injected into mice every 3 days seven times. CPT dosage was 1.5 mg/kg body weight. The first day of treatment was defined as day 0. The body weight and tumor size were recorded every 3 days, and the survival of mice was monitored throughout the experiment. The concentrations used for the groups treated with PCSN were the same as that of CPT-PCSN. After treatment for 21 days, related mice were killed, and the tumor tissues were removed from the bodies to investigate the morphology and use for further studies.

Histochemical analysis

At day 22, one mouse in each group was sacrificed to separate the tumors, and the mice were then fixed in 4% formaldehyde solution in PBS. For histochemical staining, the fixed tumors were dehydrated by gradient ethanol washing and embedded in paraffin blocks, sectioned, and stained with H&E staining.

Statistical analysis

All data were reported as means ± standard deviations (SDs). Microsoft Excel software was used to calculate *P*-values for unpaired *t*-tests. Statistical significance was determined by using Student's *t*-test and one-way analysis of variance, and *P*-values of <0.05 were considered to be indicative of statistical significance.

4.3 Results and discussion

To develop PCS on nanoparticles, we use a recombinant fusion protein, GST-HER2-Afb, in which HER2-binding affibody (Afb) is genetically combined with a glutathione-*S*-transferase (GST)[29], a well-known fusion tag protein, with an extra linker (GGGLVPRGSGGGCGGGGTGGGSGGG). The preparation of GST-HER2-Afb (molecular weight: 36.3 kDa, >99.0% purity) is confirmed by electrospray ionization time-of-flight mass spectrometry (Figure 4.1A) and sodium dodecyl sulfate–polyacrylamide gel electrophoresis (SDS-PAGE) (Figure 4.2A). The surface charge of the GST-HER2-Afb at physiological pH is approximately −5.25 mV, which is similar to that of GST (−6.29 mV) (Figure 4.1B). The intact binding ability of GST-HER2-Afb is confirmed by monitoring its interactions with the targeting receptor HER2/ErbB2 in real time using a quartz crystal microbalance (Figure 4.2B) and the cellular uptake of the fluorescein-labeled GST-HER2-Afb to the HER2-receptor-overexpressing cell line (SK-BR3) (Figure 4.1D). These results indicate that the recombinant fusion protein with the linker, GST-HER2-Afb, exhibit the ability to bind to the complementary receptor. Furthermore, the toxicity test confirms its biocompatibility, indicating that GST-HER2 itself is not toxic up to 10 μM (Figure 4.2C). Next, PCS nanoparticles (PCSNs) were constructed by supramolecularly attaching GST-HER2-Afb to mesoporous silica nanoparticle (MSN), for which cargo molecules can be loaded in the interior[30]. First, 3-(trimethoxysilyl) propyl acrylate was modified on MSN (mean diameter: 140 ± 10 nm in a dynamic light scattering (DLS), surface area: 1190 m^2/g, pore volume: 1.10 cm^3/g, mean pore size: 2.68 nm; Figure 4.3; Table 4.1) and glutathione (GSH) was further attached using thiol-ene click chemistry, which was confirmed by FT-IR analysis (Figure 4.3D). The hydrodynamic radius of the GSH-modified MSN (GSH-MSN) was ~140 ± 20 nm, as confirmed by DLS experiment, and the diameter of GSH-MSN observed from transmission electron microscopic (TEM) images was ~90 ± 10 nm (Figure 4.1E). GSH modification decreased the surface area (540 m^2/g), pore volume (0.5 cm^3/g), and mean pore size (2.04 nm) (Figure 4.3B and C; Table 4.1). Nevertheless, the GSH-MSN showed a decent cargo loading capacity of 52%, 65%, 11%, and 5% for doxorubicin (DOX), camptothecin (CPT), $DiIC_{18}$ (DiI), and DiD, respectively (Figure 4.4; Table 4.2). The GSH-MSN was then coated with GST-HER2-Afb to give the PCSN through the supramolecular interaction at the GSH-binding site. The attachment of GST-HER2 on GSH-MSN was confirmed by measuring the surface charge, which changed from −40 mV (GSH-MSN) to −5.3 mV (PCSN) (Figure 4.1B). The DLS experiment indicated an increase in the hydrodynamic radius of PCSN (~270 ± 20 nm) compared with that of GSH-MSN (~140 ± 20 nm) (Figure 4.5), and the TEM image analysis further confirmed the protein-coating layer (Figure 4.1E). The maximum number of GST-HER2-Afb attached on GSH-MSN was 270 μg/mg, which was confirmed by BCA assay (Figure 4.5B). No significant aggregation of PCSNs was observed in the DLS analysis up to 2 weeks at 4 °C (Figure 4.1C). Next, we investigated interactions occurring at the interfaces between serum proteins

and PCSNs. Control particles, GSH-MSN, and PEG-modified MSN (PEG-MSN)[31] were used to study the effects of GST-HER2-Afb pre-coating on particles. We first incubated PCSN, PEG-MSN, and GSH-MSN with 55% fetal bovine serum (FBS) for 1, 2, and 4 h and isolated the serum proteins that adsorbed to them by centrifugation to completely remove unbound proteins. The molecular composition of the adsorbed serum proteins was measured by denaturing SDS-PAGE and the protein density was plotted (Figure 4.6A and B). The protein profiles observed for PEG-MSN and GSH-MSN were fairly similar, but the intensities of the bands for PCSN were significantly reduced (~15-fold lower intensity than for GSH-MSN for the case of 1 h of incubation), indicating that the GST-HER2-Afb pre-coating on PCSN could reduce the interactions with serum proteins. To further confirm the particle–protein interactions, the physical characterizations were also investigated by using DLS, zeta, and PDI (Figure 4.7). The treatment of 55% serum on GSH-MSN and PEG-MSN increased its hydrodynamic radius and changed its surface charge while PCSN showed no significant changes, confirming the decreased PCSN–serum protein interactions. We then investigated the composition of serum proteins adsorbed on each particle using shotgun proteomics [liquid chromatography tandem mass spectrometry (LC-MS/MS)]. A total of 183 proteins were identified and the 78 most abundant proteins (at levels >0.01% w/w) were selected and divided into three groups based on the correlation in their relative abundances on each particle (Group 1: GSH-MSN > PEG-MSN > PCSN, Group 2: GSH-MSN ≈ PEG-MSN > PCSN, Group 3: GSH ≈ PEG-MSN ≈ PCSN, as shown in Figure 4.6C), which exhibited the lowest tendency to be adsorbed on PCSN. The proteins were further classified according to the weight, isoelectric point, and serum protein classification (expressed as a percentage of each protein in Figure 4.6D, middle). The proteins adsorbed on PCSN were composed of lower-molecular-weight proteins (20–60 kDa) (Figure 4.6D, left) and included an abundance of proteins with pI of approximately 7–8 compared with the proteins adsorbed on GSH-MSN and PEG-MSN (Figure 4.6D, right). Moreover, the amount of immune response involving proteins, complement, and coagulation proteins adsorbed on PCSN was significantly lower than those on GSH-MSN and PEG-MSN, suggesting that PCSN can increase their circulation time in the blood by decreasing the uptake from the immune system[20]. It is also noted that the relative quantity of apolipoproteins among serum proteins absorbed on PCSN increased with respect to GSH-MSN and to PEG-MSN (Figure 4.6D, middle). Considering that apolipoproteins on nanoparticle play an important role in association with cellular uptake to target cells[32-34], targeting capability of PCSN partly could be linked with some serum proteins recruited at the surface of PCSN. To understand the interactions between PCS and external biological components, we investigated the molecular mechanisms of the interactions associated with the conformational change of GST-HER2-Afb. When non-covalently adsorbed on nanoparticles with precisely designed supramolecular interaction, specific domains of proteins can interact with the surface of nanoparticles in thermodynamically favorable manners, leading to the colloidal stabilization and dysopsonization of particles in a physiological environment[35-36]. On the

other hand, covalent attachment of their counterparts on particles significantly changes their conformations and particle surface properties (e.g., hydrophobicity and charge density), inducing potential detrimental interactions with external biomolecules, rather than stabilizing them[13, 19, 37]. Therefore, assuming that the orientation and conformational change of proteins adsorbed on particles are subject to interaction with serum proteins, the effects of chemical modification of GST-HER2-Afb on biological consequences were investigated. First, PCSNs having randomly orientated GST-HER2-Afb [PCSN(R)s] were prepared by chemically conjugating GST-HER2-Afb to succinimidyl-modified MSN via amide formation with amine groups on the protein surface (Figure 4.6E, right). When assessed by SDS-PAGE (Figure 4.6E, left), the protein absorption for PCSN(R) was enhanced five-fold compared with that for PCSN, indicating that the randomly orientated conjugation of GST-HER2-Afb may change surface properties and increase protein–nanoparticle interactions. Next, the succinic anhydride-modified PCSN [PCSN(−)] were prepared to generate additional carboxylate groups on GST-HER2-Afb, which has a negatively charged function but still binds on GSH-MSN in the same orientation as GST-HER2-Afb (Figure 4.6E, middle). The SDS-PAGE analysis confirmed that the protein absorption observed for PCSN(−) was similar to that of PCSN, implying that once thermodynamically favorably orientated on nanoparticles, the supramolecularly adsorbed proteins can stabilize the colloid and significantly reduce the interactions with external serum proteins. We further employed coarse-grained molecular dynamics method to observe the interactions between coated silica nanoparticles (i.e. PEG-MSN, PCSN(R), PCSN (−), and PCSN) and serum protein (i.e. albumin) in the vicinity of their interface at the molecular level (simulation method details in the Figure 4.8-10), which suggests that the orientation of GST-HER2-Afb attached to the surface of silica nanoparticles as well as the electrostatic interactions can be an important factor.

We studied the cellular uptake of PCSN by macrophages, one of the most important components of the immune defense system, which act by clearing foreign molecules from the blood. Being able to evade internalization by phagocytic cells would provide a drug carrier that can accomplish long-term blood circulation and enhanced arrival at the target tumor[22, 38]. PCSNs or PEG-MSNs loaded with a fluorescent dye, DiI, were pretreated with 55% FBS for 1 h at 37 °C and then incubated with a murine macrophage-like cell line, RAW264.7, for 6 h in culture medium supplemented with 10% serum (Figure 4.11A). Confocal microscopy imaging revealed that the internalization of the DiI-loaded PEG-MSN was significant, but was rarely observed for the DiI-loaded PCSN (Figure 4.11B), which was further confirmed by flow cytometry (Figure 4.11C). Cell viability analysis also confirmed reduced cellular uptake of PCSN when the camptothecin-loaded PCSN was applied (Figure 4.11D). These results indicate that PCS on PCSN significantly reduced internalization into macrophages. A recent study reported that the biomolecular corona formation with a specific composition provides a stealth effect on the macrophage recognition[39]. Similarly, our results suggest that the scarce corona formation on PCSN caused by the supramolecularly pre-coated proteins could confer stealth

properties to evade immune cells and subsequent elimination by the MPS. Next, to investigate the cell-specific targeting ability of PCSN, the HER2-receptor-overexpressing cancer cell line SK-BR3 and the HER2-receptor-negative cell line HEK293T were treated with Dil- or camptothecin-loaded PCSN after pre-incubation in 55% FBS for 4 h (Figure 4.11E). The significant uptake of Dil-loaded PCSN by SK-BR3 cells rather than HEK293T cells, mediated by receptor-mediated endocytosis (especially macropinocytosis), was confirmed by confocal fluorescence microscopy (Figure 4.11F and Figure 4.12A) and FACS (Figure 4.12B). The targeted internalization was further confirmed by measuring cellular viability for the camptothecin-loaded PCSN, which exhibited dose-dependent toxicity on SK-BR3, while exhibiting lower toxicity on HEK293T (Figure 4.11G). A control, HER2-binding affibody (Afb) modified MSNs (Afb-MSN) was also evaluated and it confirmed that GST plays an important role in reducing interactions among the serum proteins as well as supramolecularly conjugating on particle (Figure 4.13). To examine the versatile targeting platform for PCS, EGFR-binding Afb combined with glutathione-*S*-transferase (GST-EGFR-Afb) was also applied on GSH-MSN and its targeting ability to MDA-MB468 cells (EGFR-positive cancer cells) was confirmed (Figure 4.14). Taken together, these results show that PCSN exhibited cell-specific targeting ability as well as stealth properties.

To translate the outcomes of PCSN in an in vivo tumor model, nanoparticles loaded with the far-red fluorescent dye DiD were systemically injected via the tail vein into nude mice ($n = 6$ mice per group) bearing SK-BR3 cell xenografts, after which the tumor accumulation of PCSN was monitored. Considering the lowest accumulation efficacy of GSH-MSN observed from initial experiments (Figure 4.15A), our studies focused on the comparison between PCSN and PEG-MSN. The in vivo live imaging results showed the presence of 1.8-fold enhanced fluorescent signals in tumor sites from the PCSN-treated group compared with the PEG-MSN-treated group at 0.5 h after injection (Figure 4.15B), which was maintained until 24 h, while the fluorescent signals for PEG-MSN gradually decreased with time at 8 h (Figure 4.15C). The biodistribution of nanoparticles was then assessed by measuring the fluorescence of DiD in harvested organs and tumors upon necropsy 48 h after injection. The fluorescent signals of tumors from the PCSN group were enhanced 2.5-fold in comparison with those of the PEG-MSN group (Figure 4.16A). Moreover, the fluorescent intensity in the tumor for the PCSN group was seven-fold higher than that in reticuloendothelial organs (e.g., liver and spleen), whereas no significant difference in fluorescent intensities between tumors and the reticuloendothelial organs was observed for the PEG-MSN groups (Figure 4.16B), indicating that PCS enabled the nanoparticles to evade the immune system and undergo enhanced accumulation in the target tumor. In vivo antitumor efficacy was further evaluated by intravenously administering camptothecin-loaded PCSN (PCSN(CPT)), PEG-MSN (PEG-MSN(CPT)), PCSN, camptothecin (Free-CPT), and

phosphate-buffered saline (PBS) to the SK-BR3 tumor-bearing mice. Compared with the PEG-MSN(CPT)-treated group, the PCSN(CPT)-treated group exhibited higher therapeutic efficacy, resulting in ~90.0% inhibition of tumor growth in terms of volume and 2.5-fold enhancement of inhibitory effects (Figure 4.16C). Subsequently, by examining tumor weight reduction and histopathology after necropsy on day 22, the PCSN(CPT)-treated group was shown to have enhanced therapeutic efficacy for tumor growth inhibition (Figure 4.15D). Additionally, hematoxylin and eosin (H&E)-stained lung, liver, spleen, and kidney samples showed no apparent abnormalities or lesions at day 21 after camptothecin-loaded PCSN treatment (Figure 4.17). These results indicate that PCSN increases the tumor targeting ability, enhancing the efficacy of cancer chemotherapy. Collectively, we found that the supramolecular binding of GST-HER2-Afb on particles enabled the maintenance of conformational stability and further minimized interactions with serum proteins. In vitro and in vivo experiments confirmed that PCSN improved the targeting ability and therapeutic efficacy. These findings indicate that exploiting protein coronas can provide a tool for a targeting platform.

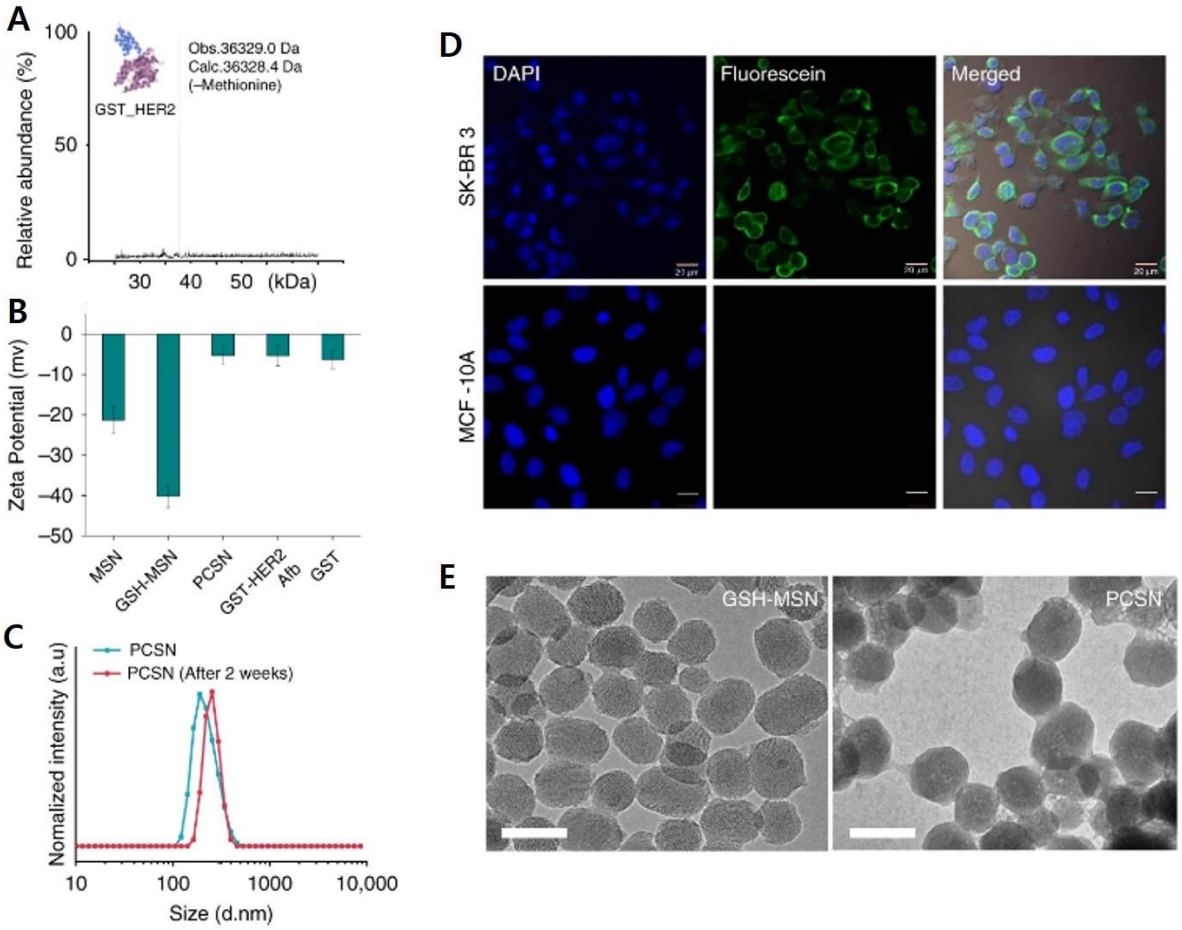

Figure 4.1 Protein corona shield nanoparticles(PCSN) (A**)** Mass spectrometry analysis of the GST-HER2-Afb showed a mass of 36.3 kDa. (B) Zeta-potential analysis of mesoporous silica nanoparticle (MSN) (−23 mV), GSH-MSN (−39 mV), GST-HER2-Afb (−5.25 mV), and PCSN (−5.3 mV). (C) Size distribution plots of PCSN. (D) Images of cellular uptake of fluorescein 5 maleimide-modified GST-HER2-Afb by the target cell (SK-BR3) and the negative control (MCF-10A). (E) Transmission electron microscopic images of GSH-MSN and PCSN (scale bar represents 100 nm). All bar graphs were reported as means ± standard deviations (SDs) for three experimental replicates ($n = 3$)

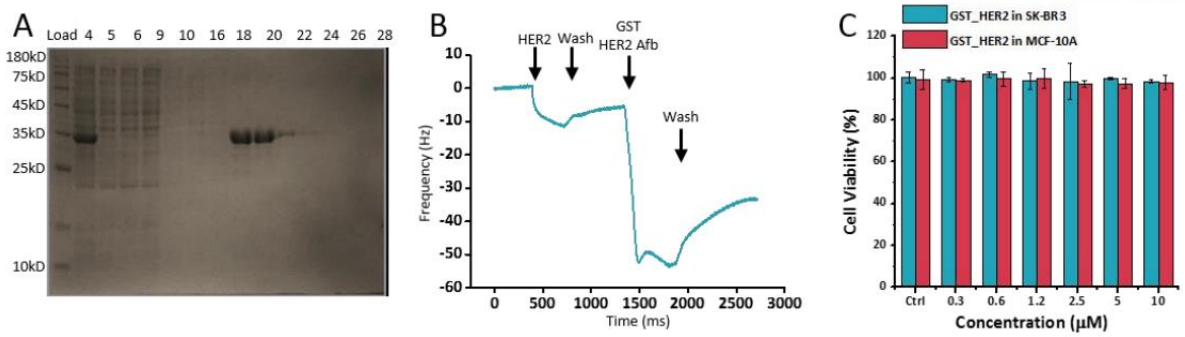

Figure 4.2 Preparation of GST-HER2-Afb. (A) Purified GST-HER2-Afb identification by SDS-PAGE. (B) Quartz crystal microbalance (QCM) analysis of HER2- Afb and GST-HER2-Afb. (C) Cell cytotoxicity test of GST-HER2-Afb in SK-BR3 and MCF-10A cells. All bar graphs were reported as means ± standard deviations (SDs) for three experimental replicates (n =3).

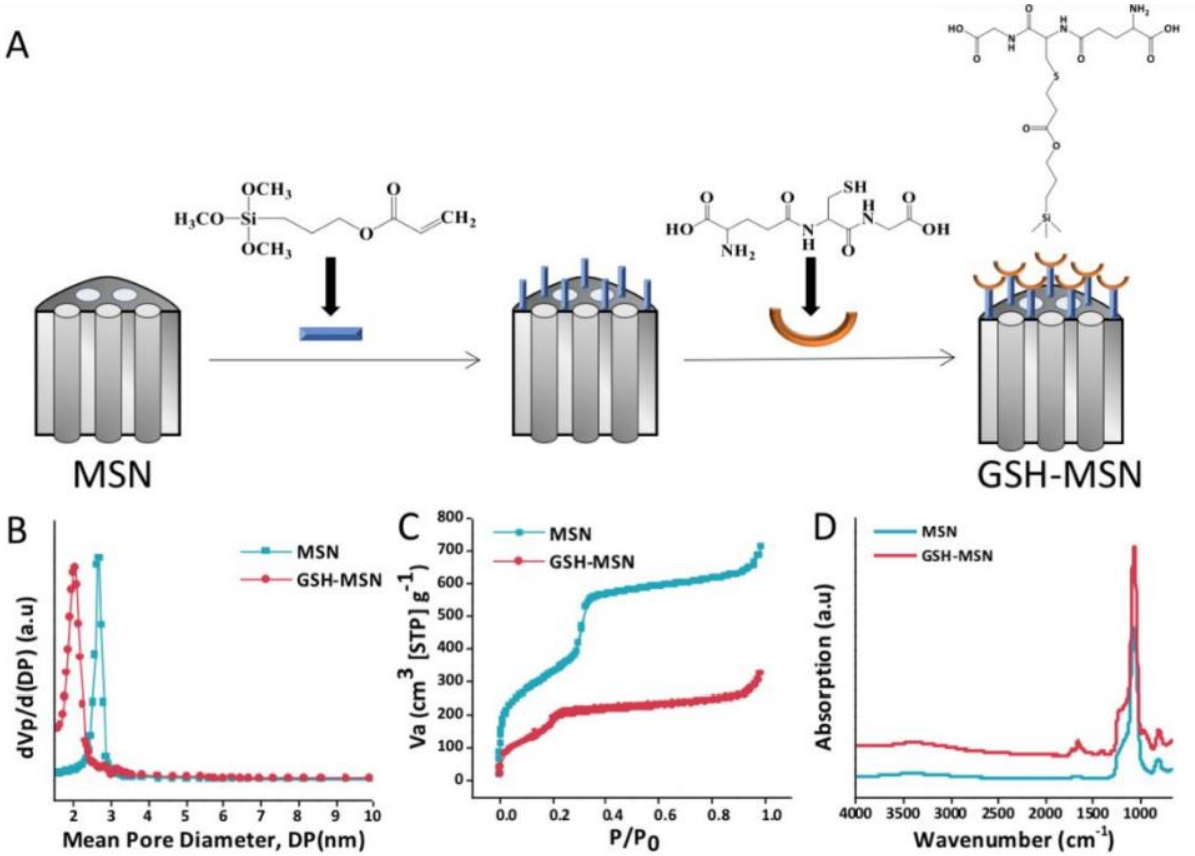

Figure 4.3 Preparation of GSH-MSN. (A) Scheme of GSH-modified mesoporous silica nanoparticles (GSH-MSNs). (B, C) Pore size and surface area change from MSNs to GSH-MSNs. (D) FTIR analysis for MSNs and GSH-MSNs.

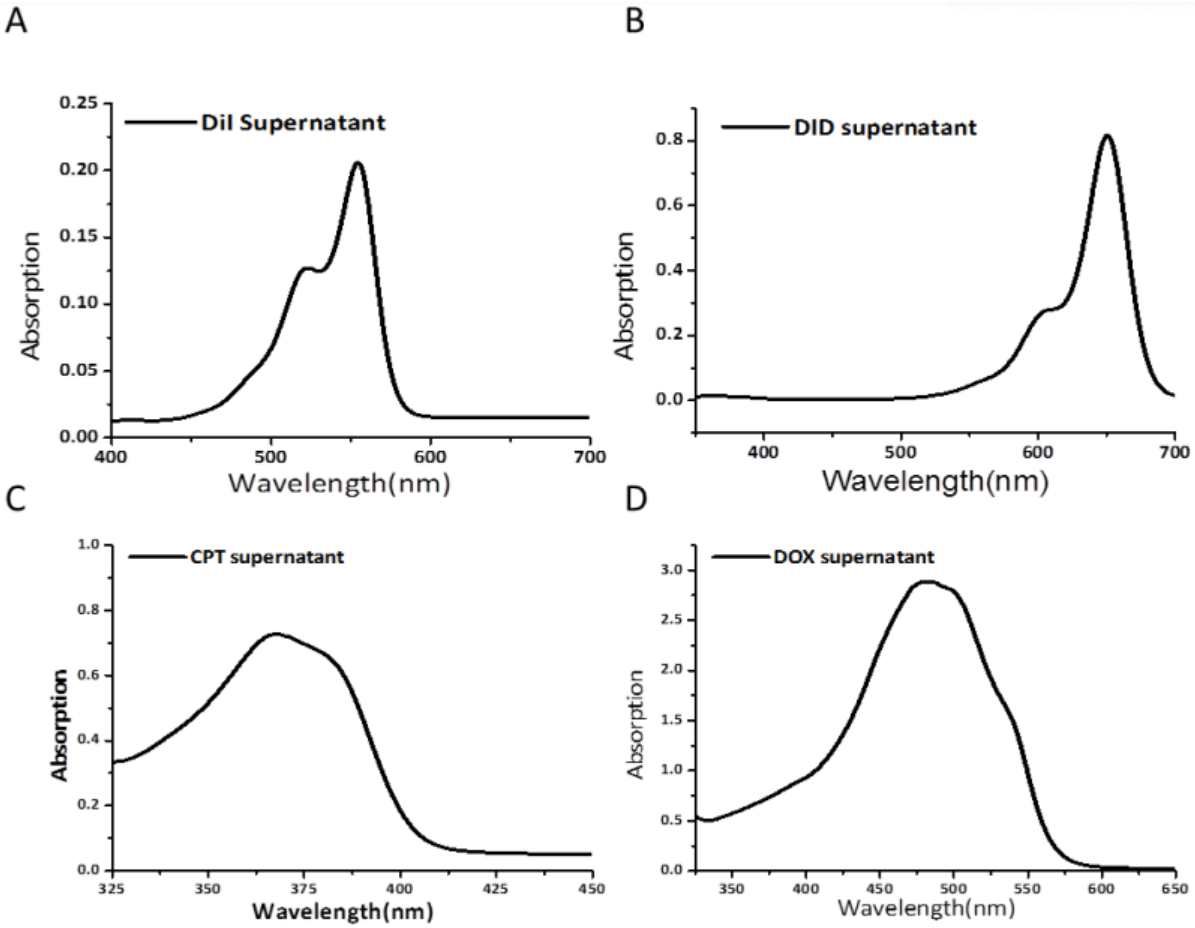

Figure 4.4 Cargo loading analysis of GSH-MSNs. UV-VIS absorption of the supernatant of (A) DiI, (B) DiD, (C) CPT, and (D) DOX solutions.

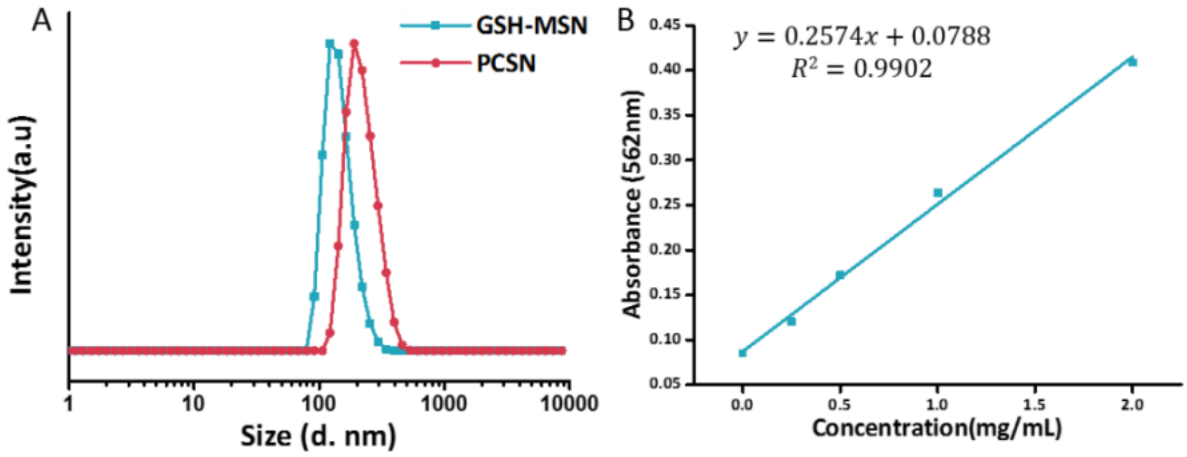

Figure 4.5 Protein absorption and size difference analysis for PCSNs.(A) Hydrodynamics diameter change between GSH-MSNs and PCSNs. (B) Concentration curve for BSA on GSH-MSNs determined using the BCA assay. The absorbance of the sample is 0.148, and the concentration is 0.27 mg/mL.

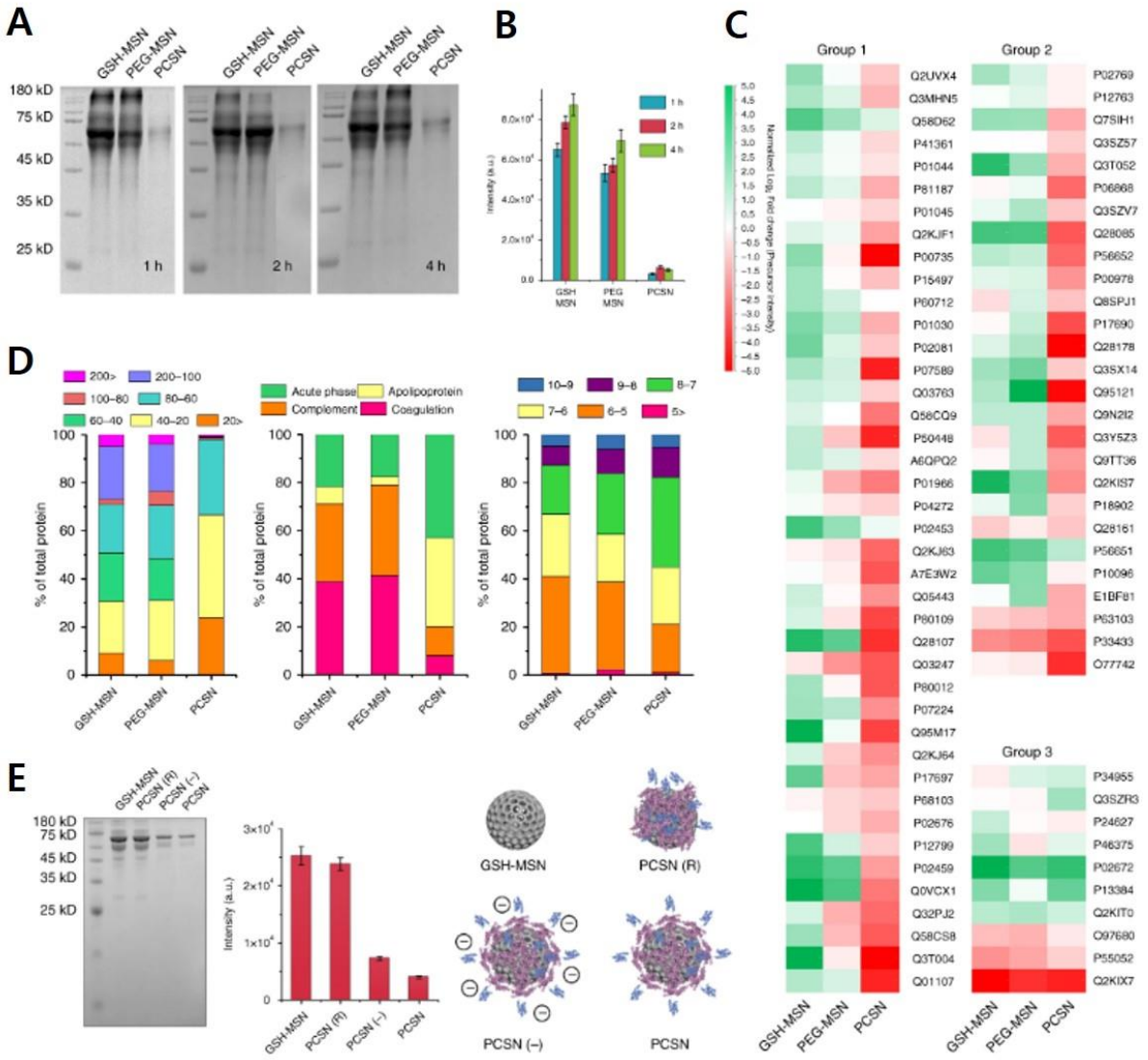

Figure 4.6 Proteomic study of surface protein corona. (A) GSH-MSN, PEG-MSN, and PCSN were treated with 55% serum for 1, 2, and 4 h, and the amount of serum protein attached to the surface was determined by SDS-PAGE. (B) Band intensity difference. (C) Classification of protein corona components characterized by quantitative LC-MS/MS. A total of 183 proteins were identified and the 78 most abundant proteins were used to make the heat map. (D) Proteins attached to each particle were classified by weight (kDa), category, and pI. (E) GSH-MSN, PCSN(R), PCSN(−), and PCSN were treated with 55% serum for 1 h and the amount of serum protein attached to the surface was determined by SDS-PAGE. All bar graphs were reported as means ± standard deviations (SDs) for three experimental replicates ($n = 3$)

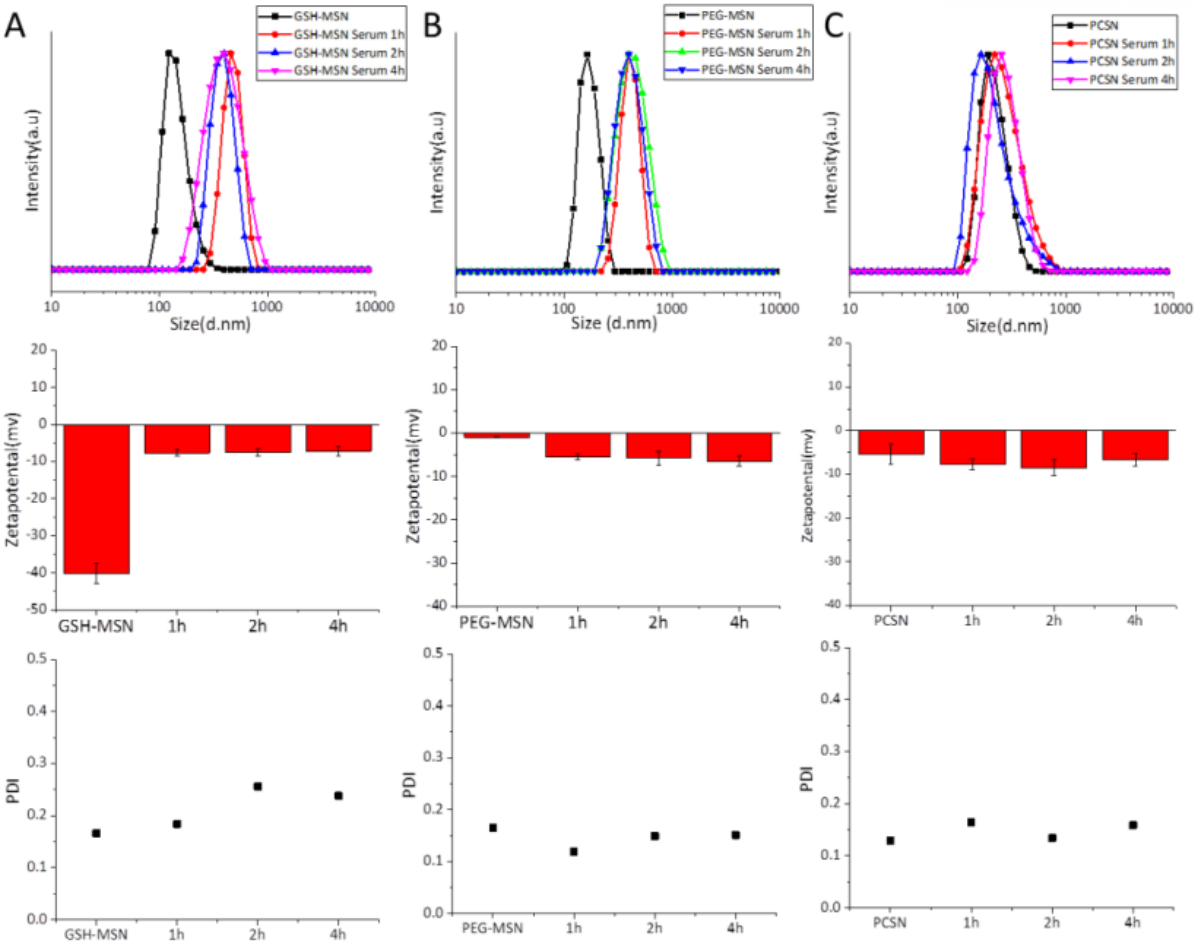

Figure 4.7 The physical-characterizations of nanoparticle-serum protein interaction. Size, surface charge and PDI analysis of (A) GSH-MSN (B) PEG-MSN (C) PCSN with treatment of the 55% serum for 1h, 2h and 4h.

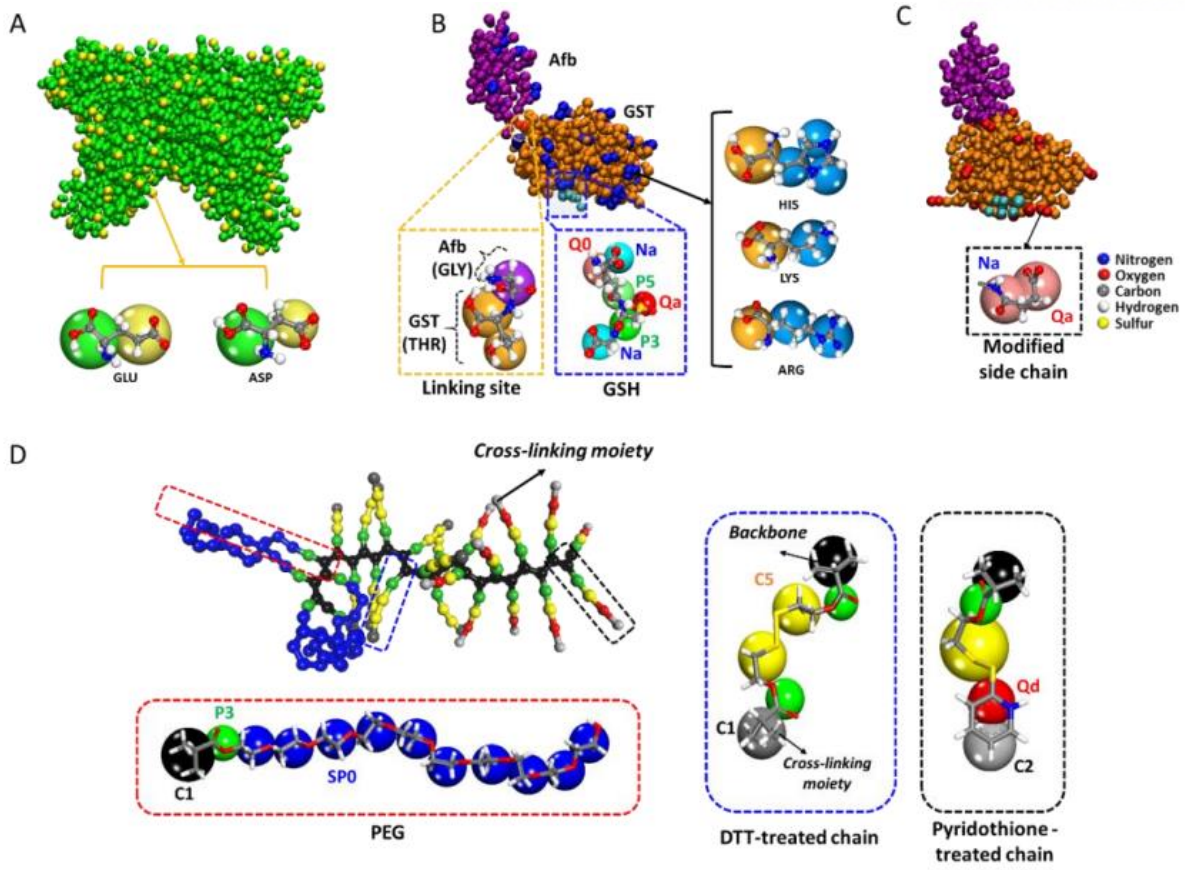

Figure 4.8 Coarse-grained molecular models. (A) Coarse-grained model of albumin. Negatively charged side chains in GLU and ASP are shown with yellow beads and coarse-grained schemes are presented. Coarse-grained models of (B) GST-HER2 Afb and (C) charge-modified GST-HER2 Afb. Yellow, blue and black dotted boxes showed magnified coarse-grained mapping of linking site between GST and Afb, GSH and modified side chain in GST, respectively. Positively charged side chains in HIS, LYS and ARG are shown in blue. (D) Coarse-grained model of PEG-PDS polymer. Red, blue and black dotted boxes represent PEG chain, DTT-treated chain and pyridothione-treated chain, respectively. Martini bead types for GSH, modified side chain and PEG-PDS polymer were shown with magnification.

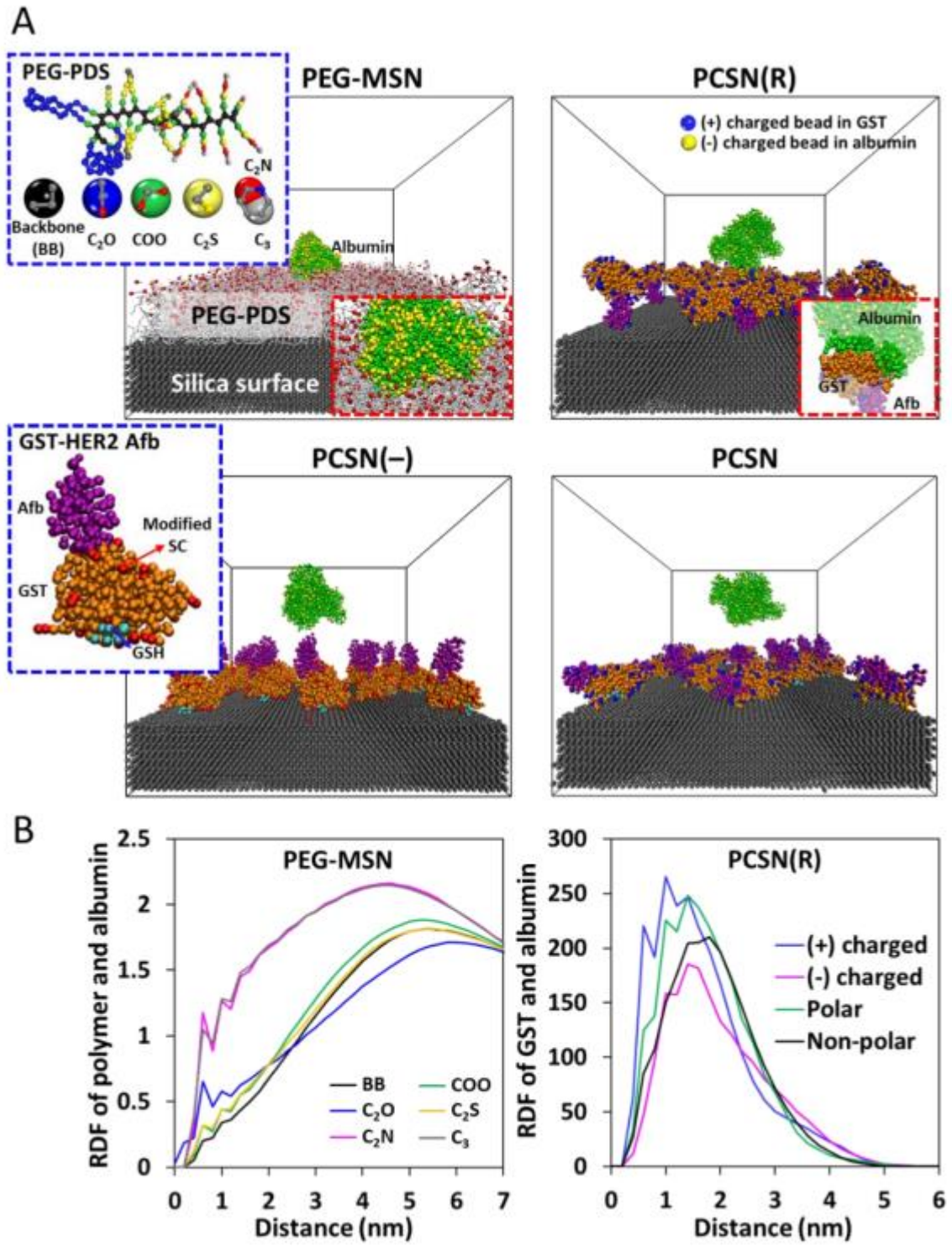

Figure 4.9 Simulations of surface protein corona phenomenon. (A) Final configurations of CGMD simulation of PEG-MSN and PCSN series interacted with albumin in water environment. Water is omitted for clear view. Blue and red dotted boxes show the structures of bead models and binding states, respectively. Color scheme is presented in detail (Supplementary Fig. 7) (B) Radial distribution functions of constituents of PEG-PDS with albumin in PEG-MSN and residues of GST with albumin in PCSN(R), respectively.

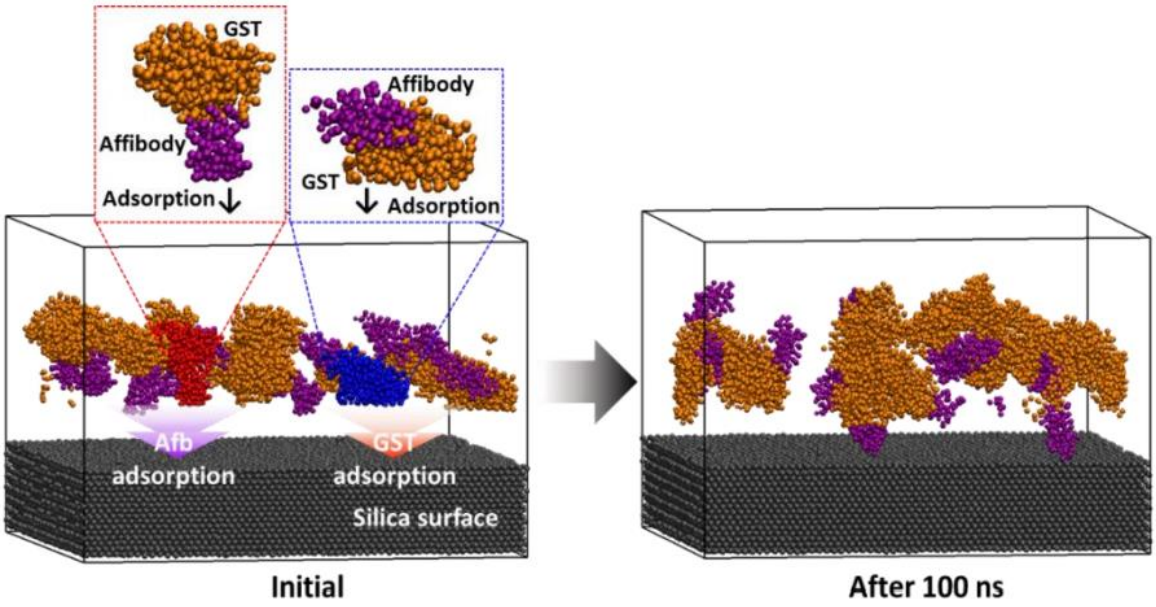

Figure 4.10 Adsorption of GST-HER2 Afb proteins on silica surface. Initial and final configurations of adsorption simulation with GST-HER2 Afb proteins on silica surface. The red-and blue-highlighted proteins represent models with adsorption directions set to Afb and GST, respectively.

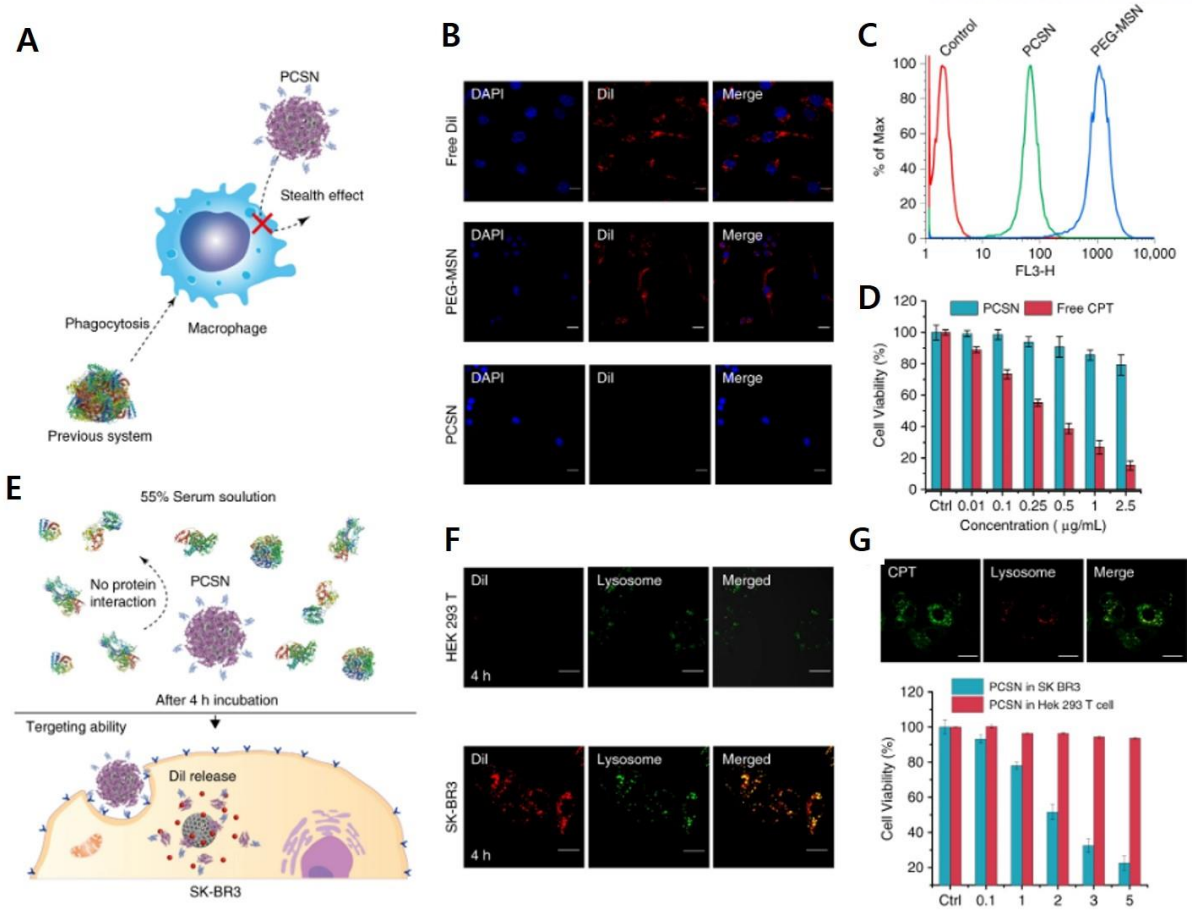

Figure 4.11 In vitro experiment and stealth effect of PCSN. (A) Schematic showing the avoidance of phagocytosis by a macrophage. (B) Confocal microscopy images of DiI-loaded PCSN and PEG-MSN, and free DiI incubated for 6 h in RAW264.7 cells (scale bar is 20 μm). (C) FACS analysis of PCSN and PEG-MSN incubated in RAW264.7 cells for 6 h. (D) Cell cytotoxicity assay of PCSN and free camptothecin (CPT) on RAW264.7 cells (48 h of incubation). (E) Schematic of the targeting ability of PCSN treated with 55% serum. Cellular uptake confocal microscopy images of (F) DiI-loaded PCSN to HEK293T cells (negative control) and to SK-BR3 (target cells). (G) Cellular uptake confocal microscopic images of camptothecin-loaded PCSN to SK-BR3 and cell cytotoxicity assay (scale bar is 10 μm). All bar graphs were reported as means ± standard deviations (SDs) for three experimental replicates ($n = 3$)

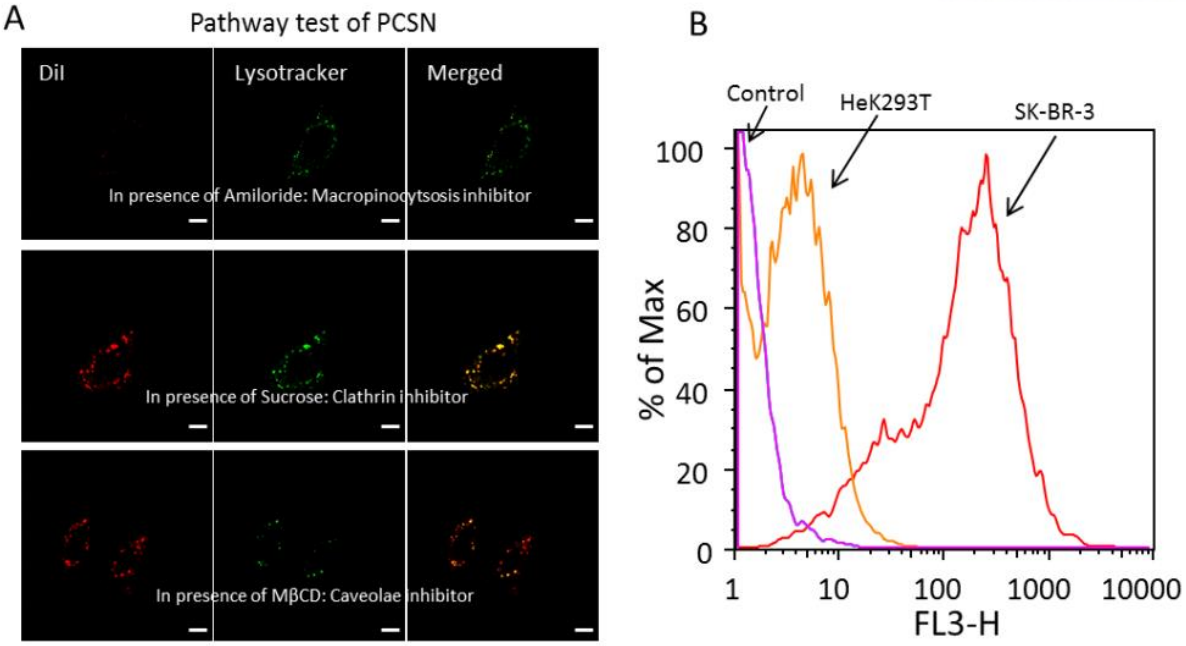

Figure 4.12 Pathway test of PCSN (A) Cellular uptake image of PCSN to SK-BR3 in the presence of amiloride, sucrose , MβCD . (B) fluorescence-activated cell sorting analysis of dye (DiI)-loaded PCSN (scale bar is 5 μm).

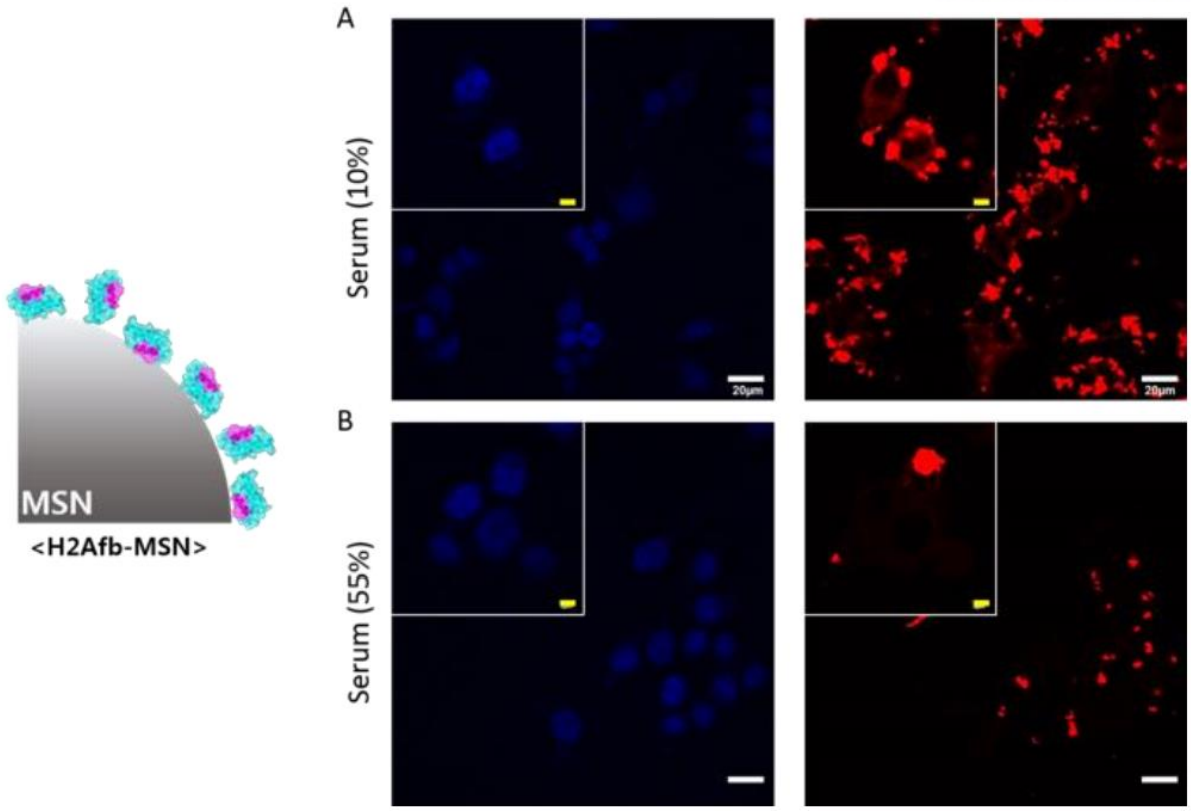

Figure 4.13 In-vitro experiment for randomly modified MSN. Cellular uptake experiment for dye-containing (DiIC18) HER2-binding affibody (Afb) modified MSNs (Afb-MSN) on SK-BR3 cell. The Afb-MSN was pre-treated in (A) 10% serum and (B) 55% serum for 1 hour (Scale bar is 20 μm and scale bar of inset image is 5 μm).

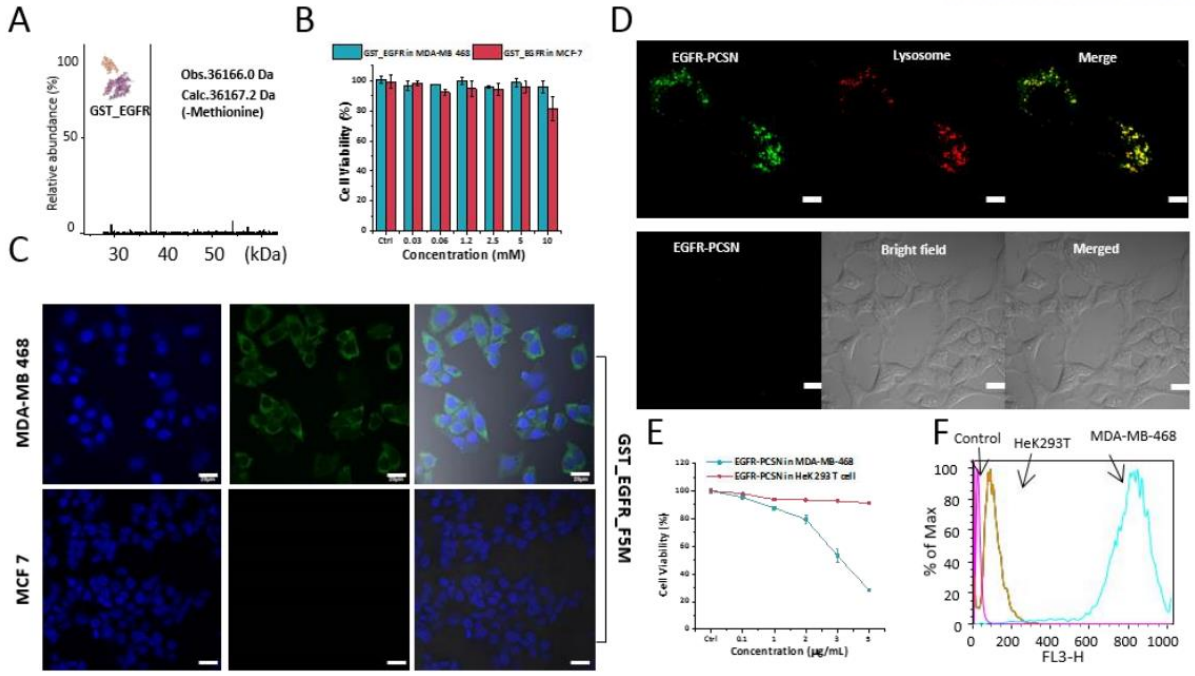

Figure 4.14 Preparations of GST-EGFR-Afb and EGFR-PCSNs. (A) Mass spectrometry analysis of the GST-EGFR-Afb was 36.1 kDa; (B) cell cytotoxicity test of GST-EGFR-Afb in MDA-MB468 and MCF-10A cells; (C) cellular uptake images of fluorescein 5 maleimide-modified GST-EGFR-Afb (GST-EGFR-Afb F5M) into the target cell (MDA-MB468) and the negative control (MCF-10A) (Scale bar is 20 μm); (D) CPTloaded EGFR-PCSNs into MDA-MB468 (scale bar is 5 μm) and HeK293T cells (scale bar is 10 μm); (E) cell cytotoxicity assay; (F) fluorescence-activated cell sorting analysis of dye (DiI)-loaded EGFR-PCSNs. Figure B and E graphs were reported as means ± standard deviations (SDs) for three experimental replicates (n =3).

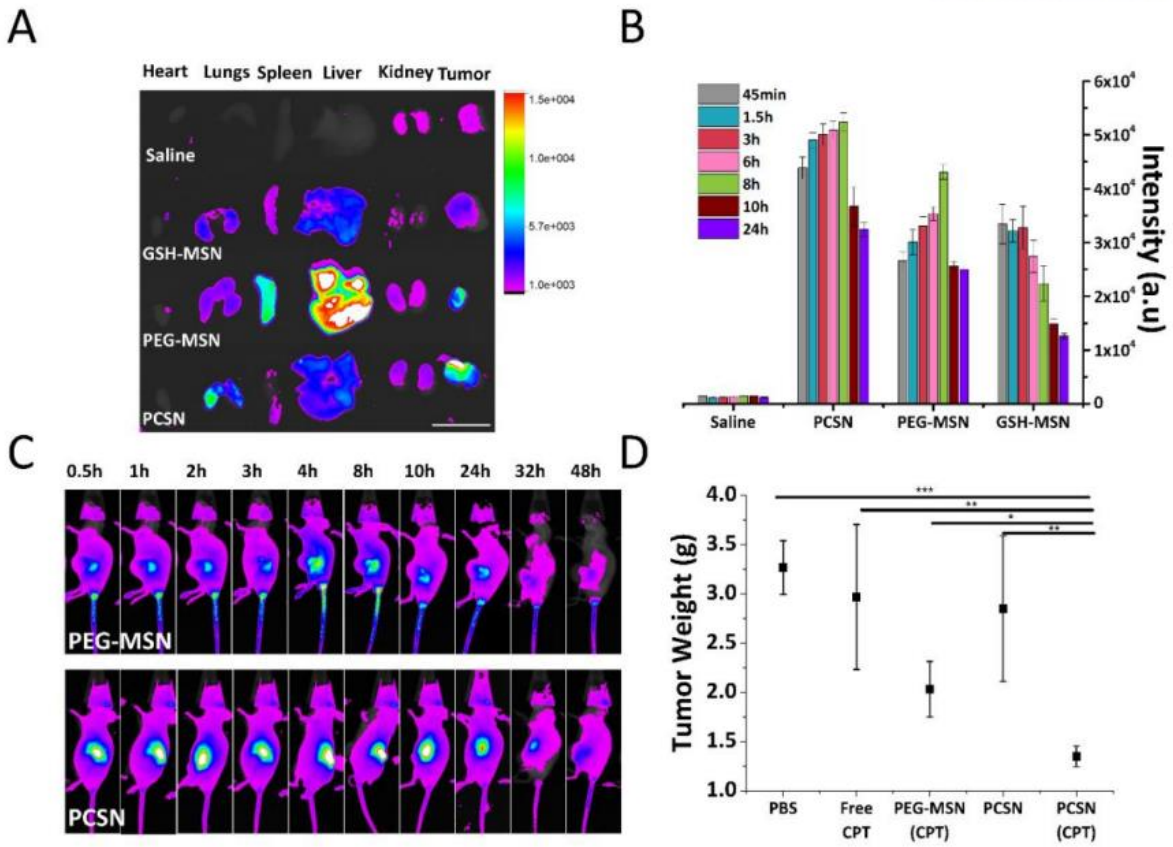

Figure 4.15 Pre-in vivo and -ex vivo experiments with PCSNs. (A) Ex vivo fluorescence imaging data of each organ; (B) changes in DiD intensity of tumors in each group per each time (each animal received a particle dose of 1 mg/mice (~50 mg/kg), which delivers ~3 mg/kg of DiD per mouse, n = 3/group by IV injection), (Scale bar is 2 cm); (C) representative whole-body fluorescence images of subcutaneous SK-BR3 tumor-bearing mice intravenously injected with nanoparticles (1.5 mg/kg of DiD per mouse, n = 6/group by IV injection); (D) tumor weight of each group (n = 6/group, mean ± SD, statistical significance was calculated by one-way analysis of variance. *P < 0.05, **P < 0.01, *** P < 0.001). All bar graphs were reported as means ± standard deviations (SDs) (n = 6/group).

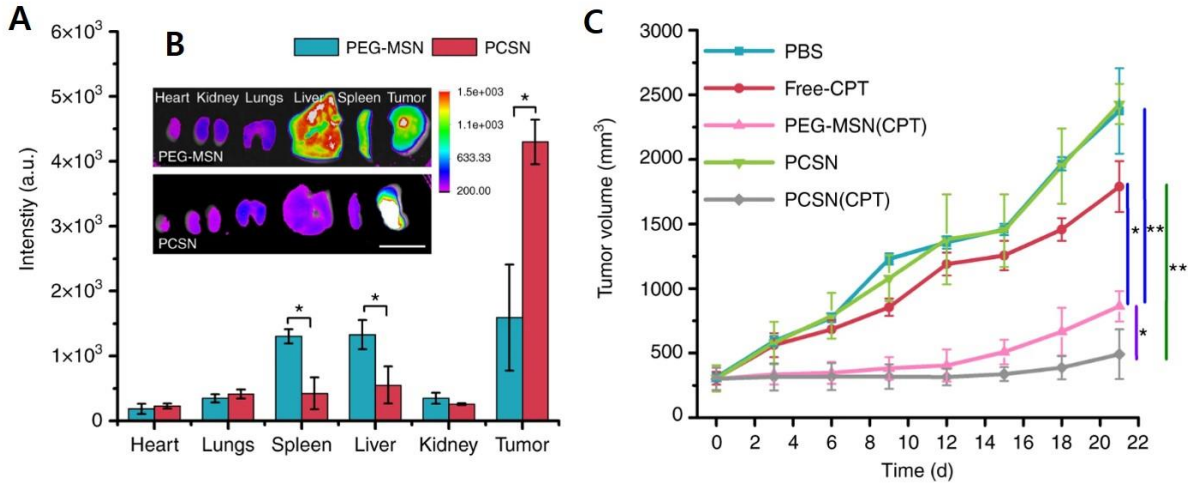

Figure 4.16 Ex vivo and in vivo efficiency of PCSN. (A, B) Fluorescence images of organs and tumors 48 h after intravenous injection and biodistribution of injected formulations in animals with SK-BR3 tumor xenograft from fluorescence intensity analysis. In vivo antitumor effects in different treatment groups loaded with camptothecin (CPT) (1.5 mg/kg of mice) (scale bar is 2 cm). (C) Growth curve of tumor volume after intravenous injection with various groups of carriers until day 21 ($n = 6$ mice per group, mean ± 1 day [$n = 6$ mice per group, mean ± SD, statistical significance was calculated by one-way analysis of variance, *$P < 0.05$, **$P < 0.01$]

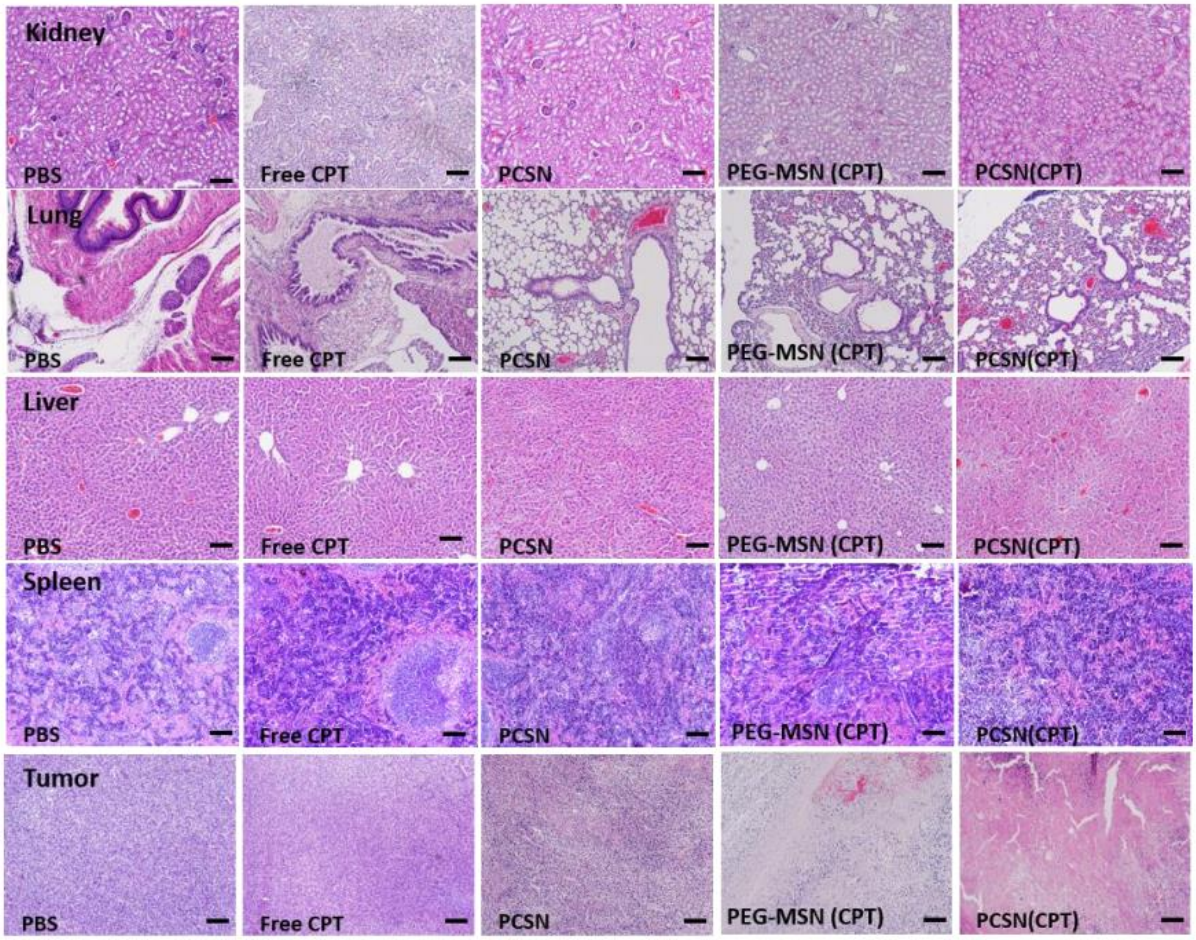

Figure 4.17 Histological evaluations of tumor tissues. Hematoxylin and eosin (H&E) staining of the lung, liver, spleen, kidney, and tumor. (Scale bar is 50 μm)

4.4 Conclusions

Targeted drug delivery using nanoparticles can minimize the side effects of conventional pharmaceutical agents and enhance their efficacy. However, translating nanoparticle-based agents into clinical applications still remains a challenge due to the difficulty in regulating interactions on the interfaces between nanoparticles and biological systems. Here, we present a targeting strategy for nanoparticles incorporated with a supramolecularly pre-coated recombinant fusion protein in which HER2-binding affibody combines with glutathione-*S*-transferase. Once thermodynamically stabilized in preferred orientations on the nanoparticles, the adsorbed fusion proteins as a corona minimize interactions with serum proteins to prevent the clearance of nanoparticles by macrophages, while ensuring systematic targeting functions in vitro and in vivo. This study provides insight into the use of the supramolecularly built protein corona shield as a targeting agent through regulating the interfaces between nanoparticles and biological systems.

4.5 References

1. Walkey, C. D.; Chan, W. C. W., Understanding and controlling the interaction of nanomaterials with proteins in a physiological environment. *Chem Soc Rev* **2012,** *41* (7), 2780-2799.

2. Peer, D.; Karp, J. M.; Hong, S.; FaroKHzad, O. C.; Margalit, R.; Langer, R., Nanocarriers as an emerging platform for cancer therapy. *Nat Nanotechnol* **2007,** *2* (12), 751-760.

3. Bertrand, N.; Wu, J.; Xu, X. Y.; Kamaly, N.; Farokhzad, O. C., Cancer nanotechnology: The impact of passive and active targeting in the era of modern cancer biology. *Adv Drug Deliver Rev* **2014,** *66*, 2-25.

4. Maeda, H.; Nakamura, H.; Fang, J., The EPR effect for macromolecular drug delivery to solid tumors: Improvement of tumor uptake, lowering of systemic toxicity, and distinct tumor imaging in vivo. *Adv Drug Deliver Rev* **2013,** *65* (1), 71-79.

5. Mahmoudi, M.; Bertrand, N.; Zope, H.; Farokhzad, O. C., Emerging understanding of the protein corona at the nano-bio interfaces. *Nano Today* **2016,** *11* (6), 817-832.

6. Hatakeyama, H.; Akita, H.; Harashima, H., A multifunctional envelope type nano device (MEND) for gene delivery to tumours based on the EPR effect: A strategy for overcoming the PEG dilemma. *Adv Drug Deliver Rev* **2011,** *63* (3), 152-160.

7. Xu, X. Y.; Ho, W.; Zhang, X. Q.; Bertrand, N.; Farokhzad, O., Cancer nanomedicine: from targeted delivery to combination therapy. *Trends Mol Med* **2015,** *21* (4), 223-232.

8. Wilhelm, S.; Tavares, A. J.; Dai, Q.; Ohta, S.; Audet, J.; Dvorak, H. F.; Chan, W. C. W., Analysis of nanoparticle delivery to tumours. *Nat Rev Mater* **2016,** *1* (5).

9. Monopoli, M. P.; Aberg, C.; Salvati, A.; Dawson, K. A., Biomolecular coronas provide the biological identity of nanosized materials. *Nat Nanotechnol* **2012,** *7* (12), 779-786.

10. Lynch, I.; Dawson, K. A., Protein-nanoparticle interactions. *Nano Today* **2008,** *3* (1-2), 40-47.

11. Mahmoudi, M.; Lynch, I.; Ejtehadi, M. R.; Monopoli, M. P.; Bombelli, F. B.; Laurent, S., Protein-Nanoparticle Interactions: Opportunities and Challenges. *Chem Rev* **2011,** *111* (9), 5610-5637.

12. Nel, A. E.; Madler, L.; Velegol, D.; Xia, T.; Hoek, E. M.; Somasundaran, P.; Klaessig, F.; Castranova, V.; Thompson, M., Understanding biophysicochemical interactions at the nano-bio interface. *Nat Mater* **2009,** *8* (7), 543-57.

13. Salvati, A.; Pitek, A. S.; Monopoli, M. P.; Prapainop, K.; Bombelli, F. B.; Hristov, D. R.; Kelly, P. M.; Aberg, C.; Mahon, E.; Dawson, K. A., Transferrin-functionalized nanoparticles lose their targeting capabilities when a biomolecule corona adsorbs on the surface. *Nat Nanotechnol* **2013,** *8* (2), 137-143.

14. Mizuhara, T.; Saha, K.; Moyano, D. F.; Kim, C. S.; Yan, B.; Kim, Y. K.; Rotello, V. M.,

Acylsulfonamide-Functionalized Zwitterionic Gold Nanoparticles for Enhanced Cellular Uptake at Tumor pH. *Angew Chem Int Edit* **2015,** *54* (22), 6567-6570.

15. Kang, B.; Okwieka, P.; Schottler, S.; Winzen, S.; Langhanki, J.; Mohr, K.; Opatz, T.; Mailander, V.; Landfester, K.; Wurm, F. R., Carbohydrate-Based Nanocarriers Exhibiting Specific Cell Targeting with Minimum Influence from the Protein Corona. *Angew Chem Int Edit* **2015,** *54* (25), 7436-7440.

16. Dai, Q.; Walkey, C.; Chan, W. C. W., Polyethylene Glycol Backfilling Mitigates the Negative Impact of the Protein Corona on Nanoparticle Cell Targeting. *Angew Chem Int Edit* **2014,** *53* (20), 5093-5096.

17. Wan, S.; Kelly, P. M.; Mahon, E.; Stockmann, H.; Rudd, P. M.; Caruso, F.; Dawson, K. A.; Yan, Y.; Monopoli, M. P., The "Sweet" Side of the Protein Corona: Effects of Glycosylation on Nanoparticle-Cell Interactions. *Acs Nano* **2015,** *9* (2), 2157-2166.

18. Tenzer, S.; Docter, D.; Kuharev, J.; Musyanovych, A.; Fetz, V.; Hecht, R.; Schlenk, F.; Fischer, D.; Kiouptsi, K.; Reinhardt, C.; Landfester, K.; Schild, H.; Maskos, M.; Knauer, S. K.; Stauber, R. H., Rapid formation of plasma protein corona critically affects nanoparticle pathophysiology. *Nat Nanotechnol* **2013,** *8* (10), 772-U1000.

19. Mirshafiee, V.; Kim, R.; Park, S.; Mahmoudi, M.; Kraft, M. L., Impact of protein pre-coating on the protein corona composition and nanoparticle cellular uptake. *Biomaterials* **2016,** *75*, 295-304.

20. Corbo, C.; Molinaro, R.; Taraballi, F.; Furman, N. E. T.; Hartman, K. A.; Sherman, M. B.; De Rosa, E.; Kirui, D. K.; Salvatore, F.; Tasciotti, E., Unveiling the in Vivo Protein Corona of Circulating Leukocyte-like Carriers. *Acs Nano* **2017,** *11* (3), 3262-3273.

21. Schottler, S.; Becker, G.; Winzen, S.; Steinbach, T.; Mohr, K.; Landfester, K.; Mailander, V.; Wurm, F. R., Protein adsorption is required for stealth effect of poly(ethylene glycol)- and poly(phosphoester)-coated nanocarriers. *Nat Nanotechnol* **2016,** *11* (4), 372-377.

22. Takeuchi, T.; Kitayama, Y.; Sasao, R.; Yamada, T.; Toh, K.; Matsumoto, Y.; Kataoka, K., Molecularly Imprinted Nanogels Acquire Stealth In Situ by Cloaking Themselves with Native Dysopsonic Proteins. *Angew Chem Int Edit* **2017,** *56* (25), 7088-7092.

23. Ke, P. C.; Lin, S.; Parak, W. J.; Davis, T. P.; Caruso, F., A Decade of the Protein Corona. *Acs Nano* **2017,** *11* (12), 11773-11776.

24. Kah, J. C. Y.; Chen, J.; Zubieta, A.; Hamad-Schifferli, K., Exploiting the Protein Corona around Gold Nanorods for Loading and Triggered Release. *Acs Nano* **2012,** *6* (8), 6730-6740.

25. Hadjidemetriou, M.; Al-Ahmady, Z.; Mazza, M.; Collins, R. F.; Dawson, K.; Kostarelos, K., In Vivo Biomolecule Corona around Blood-Circulating, Clinically Used and Antibody-Targeted Lipid Bilayer Nanoscale Vesicles. *Acs Nano* **2015,** *9* (8), 8142-8156.

26. Lazarovits, J.; Chen, Y. Y.; Sykes, E. A.; Chan, W. C. W., Nanoparticle-blood interactions: the implications on solid tumour targeting. *Chem Commun* **2015,** *51* (14), 2756-2767.

27. Hamad-Schifferli, K., Exploiting the novel properties of protein coronas: emerging applications in nanomedicine. *Nanomedicine-Uk* **2015,** *10* (10), 1663-1674.

28. Saha, K.; Rahimi, M.; Yazdani, M.; Kim, S. T.; Moyano, D. F.; Hou, S.; Das, R.; Mout, R.; Rezaee, F.; Mahmoudi, M.; Rotello, V. M., Regulation of Macrophage Recognition through the Interplay of Nanoparticle Surface Functionality and Protein Corona. *Acs Nano* **2016,** *10* (4), 4421-4430.

29. Martos-Maldonado, M. C.; Casas-Solvas, J. M.; Tellez-Sanz, R.; Mesa-Valle, C.; Quesada-Soriano, I.; Garcia-Maroto, F.; Vargas-Berenguel, A.; Garcia-Fuentes, L., Binding properties of ferrocene-glutathione conjugates as inhibitors and sensors for glutathione S-transferases. *Biochimie* **2012,** *94* (2), 541-550.

30. Palanikumar, L.; Choi, E. S.; Cheon, J. Y.; Joo, S. H.; Ryu, J. H., Noncovalent Polymer-Gatekeeper in Mesoporous Silica Nanoparticles as a Targeted Drug Delivery Platform. *Adv Funct Mater* **2015,** *25* (6), 957-965.

31. Palanikumar, L.; Kim, H. Y.; Oh, J. Y.; Thomas, A. P.; Choi, E. S.; Jeena, M. T.; Joo, S. H.; Ryu, J. H., Noncovalent Surface Locking of Mesoporous Silica Nanoparticles for Exceptionally High Hydrophobic Drug Loading and Enhanced Colloidal Stability. *Biomacromolecules* **2015,** *16* (9), 2701-2714.

32. Pozzi, D.; Colapicchioni, V.; Caracciolo, G.; Piovesana, S.; Capriotti, A. L.; Palchetti, S.; De Grossi, S.; Riccioli, A.; Amenitsch, H.; Lagana, A., Effect of polyethyleneglycol (PEG) chain length on the bio-nano-interactions between PEGylated lipid nanoparticles and biological fluids: from nanostructure to uptake in cancer cells. *Nanoscale* **2014,** *6* (5), 2782-2792.

33. Caracciolo, G., Clinically approved liposomal nanomedicines: lessons learned from the biomolecular corona. *Nanoscale* **2018,** *10* (9), 4167-4172.

34. Digiacomo, L.; Cardarelli, F.; Pozzi, D.; Palchetti, S.; Digman, M. A.; Gratton, E.; Capriotti, A. L.; Mahmoudi, M.; Caracciolo, G., An apolipoprotein-enriched biomolecular corona switches the cellular uptake mechanism and trafficking pathway of lipid nanoparticles. *Nanoscale* **2017,** *9* (44), 17254-17262.

35. Treuel, L.; Brandholt, S.; Maffre, P.; Wiegele, S.; Shang, L.; Nienhaus, G. U., Impact of Protein Modification on the Protein Corona on Nanoparticles and Nanoparticle-Cell Interactions. *Acs Nano* **2014,** *8* (1), 503-513.

36. Mortimer, G. M.; Butcher, N. J.; Musumeci, A. W.; Deng, Z. J.; Martin, D. J.; Minchin, R. F., Cryptic Epitopes of Albumin Determine Mononuclear Phagocyte System Clearance of Nanomaterials. *Acs Nano* **2014,** *8* (4), 3357-3366.

37. Herda, L. M.; Hristov, D. R.; Lo Giudice, M. C.; Polo, E.; Dawson, K. A., Mapping of Molecular Structure of the Nanoscale Surface in Bionanoparticles. *Journal of the American Chemical Society* **2017,** *139* (1), 111-114.

38. Cao, H. Q.; Zou, L. L.; He, B.; Zeng, L. J.; Huang, Y. Z.; Yu, H. J.; Zhang, P. C.; Yin, Q.; Zhang, Z. W.; Li, Y. P., Albumin Biomimetic Nanocorona Improves Tumor Targeting and Penetration for Synergistic Therapy of Metastatic Breast Cancer. *Adv Funct Mater* **2017,** *27* (11).

39. Caracciolo, G.; Palchetti, S.; Colapicchioni, V.; Digiacomo, L.; Pozzi, D.; Capriotti, A. L.; La Barbera, G.; Lagana, A., Stealth Effect of Biomolecular Corona on Nanoparticle Uptake by Immune Cells. *Langmuir* **2015,** *31* (39), 10764-10773.

Conclusions

In this dissertation, I developed protein nanoparticle-based cargo-delivery system. Conventional drugs have many limitations on their use due to their physicochemical properties including low solubility, stability, short half-life, and high diffusion rate to normal tissues. Here, I proved that protein nanoparticle could be utilized in cargo delivery for enhanced efficacy of drugs and low side-effects of cargoes. In addition, targeting ligands including antibodies and affibody molecules were decorated on nanoparticles for active targeting as well as passive targeting via EPR effect.

In chapter 2, I developed a universal multivalent antibody-binding nanoplatform by insertion of ABDs to AaLS protein cage nanoparticle. ABD–AaLS effectively captures various types of antibodies derived from diverse species on demand, and that their complexes selectively recognize and bind to their target cells *in vitro*, guided by antibodies displayed on the surface of ABD–AaLS.

In chapter 3, I developed target-tunable P22 VLP-based polyvalent delivery nanoplatforms, ligated two different targeting affibody molecules on demand. Here, I utilized bacterial superglue SpyTag/SpyCathcer forming covalent isopeptide bond. P22 VLP having two different affibody molecules could load pH-sensitive prodrugs and selectively kill target cells in vitro.

In chapter 4, I developed cloaking nanoparticles for drug delivery. I bound GST fused affibody molecules on GSH expressing mesoporous silica nanoparticles via non-covalent binding of GST/GSH. Bound fusion protein stabilized in preferred orientations on the nanoparticles, which minimize interactions with serum proteins to prevent the clearance of nanoparticles by macrophages, while ensuring systematic targeting functions in vitro and in vivo

Acknowledgement

2010 년 철없던 대학생이던 제가 10 년이라는 시간이 지난 지금 박사 졸업을 앞두고 있습니다. 박사 학위를 취득한다는 기쁨과 더불어 새로운 시작에 대한 두려움이 함께하는 기분입니다. 저 혼자서는 결코 해내지 못했을 일입니다. 도움을 주신 모든 분들께 진심 어린 감사의 인사와 고마움을 전하고자 합니다.

제일 먼저 저의 지도교수님이신 강세병 교수님께 감사의 말씀을 전하고 싶습니다. 교수님의 조언과 가르침으로 인해 제가 무사히 대학원생활을 마칠 수 있었습니다. 연구에 대한 조언 뿐 아니라 저의 부족한 부분과 개선 방향, 연구자가 가져야할 자세 등을 포함한 많은 가르침을 주셨습니다. 부족한 제가 교수님의 지도로 인해서 이렇게 성장할 수 있었습니다. 교수님께 지도를 받을 수 있어서 영광이었고, 교수님을 롤모델로 삼아 저 또한 훌륭한 연구자이자 멘토가 될 수 있도록 항상 노력하겠습니다.

그리고 졸업위원으로 많은 조언을 해주신 유자형 교수님, 이창욱 교수님, 조형준 교수님, 채영찬 교수님께 다시 한번 감사드립니다. 교수님들께서 바쁘신 와중에도 졸업 발표를 포함한 여러 번의 미팅에 참석하셔서 해주신 조언과 격려들은 앞으로도 마음 속 깊이 간직하겠습니다.

제가 연구실에 처음 들어와 적응을 못하고 있을 때 많은 도움을 준 신현희 선생님, 강영지 누나, 문효진 누나, 최봉서 형, 민준선 선배, 이지수 선배에게도 고마움을 전하고 싶습니다. 다들 원하는 목표를 모두 이루어 가까운 미래에 웃으며 이야기하고 싶습니다. 그리고 부족한 저를 따라와 준 실험실 동료들에게도 고맙다는 말을 전하고 싶습니다. 언제나 자기 실험에 애착을 가지고 열의를 보이는 최혁준 후배, 궂은 일을 도맡아서 실험실의 랩장 노릇을 야무지게 하고 있는 배윤지 후배, 사차원이지만 실험은 똑똑하게 하는 박성국 후배, 아직 1 년차이지만 누구보다 열심히 일을 하고 고민하는 엄수민 후배, 박사 선배로서 진로에 대해 많은 조언을 해준 이창규 박사님, 아직 익숙하진 않지만 연구에 적응하기 위해 언제나 열심히 노력 중인 이희진 후배. 모두 대학원 생활 무사히 마칠 거라 믿어 의심치 않습니다.

그리고 6 년동안의 학위 과정동안 묵묵히 저의 선택을 지지해주시고 지원해주신 부모님께 이 자리를 빌어 감사의 인사를 드리고 싶습니다. 무뚝뚝한 아들이라 표현을 잘 하지 못했지만, 부모님이 곁에 계시다는 것만으로도 저에게 있어 큰 버팀목이 되었습니다.

여기에는 다 언급하지 못했지만, 저와 인연이 있는 모든 연구원분들과 친구들께 못다한 인사를 전하고 싶습니다. 이 곳에서 지냈던 6 년동안의 시간이 제가 앞으로 연구자의 길을 가는데 있어서 무엇과도 바꿀 수 없는 소중한 시간이 될 것입니다. 다시한번 모든 분들께 감사드립니다.